SURFACE REACTION MECHANISMS FOR PLASMA PROCESSING OF SEMICONDUCTORS

BY

ARVIND SANKARAN

B.Tech., Indian Institute of Technology, Madras, 1999
M.S., University of Illinois at Urbana-Champaign, 2001

DISSERTATION

Submitted in partial fulfillment of the requirements
for the degree of Doctor of Philosophy in Chemical and Biomolecular Engineering
in the Graduate College of the
University of Illinois at Urbana-Champaign, 2003

Urbana, Illinois

RED BORDER FORM

SURFACE REACTION MECHANISMS FOR PLASMA PROCESSING OF SEMICONDUCTORS

Arvind Sankaran, Ph.D.
Department of Chemical and Biomolecular Engineering
University of Illinois at Urbana-Champaign, 2003
Mark J. Kushner, Advisor

Plasma-surface interactions are critical during plasma processing for microelectronic fabrication. Surface reaction mechanisms are indispensable to understanding the evolution of features during the various plasma processing steps. As microelectronic device features have become smaller, device speeds and performance depend heavily on the resistance-capacitance (RC) delay times in the interconnect wiring. This has brought focus onto low dielectric constant (low-k) materials as the inter layer dielectric (ILD) and copper as the interconnect wire material. Porous silica (PS) is a promising candidate for ILDs. Integration of such new materials into microelectronic fabrication has increased the importance of understanding and characterizing the complex surface phenomena during its processing. The plasma processing steps of interest in this work are fluorocarbon etch of solid SiO_2 (SS) and PS, clean of the residual fluorocarbon polymer from the trenches and fill with Cu.

Profile evolution and maintenance of critical dimensions during plasma etching of PS are problematic due to the exposure of open pores. To investigate issues related to etching, reaction mechanisms for fluorocarbon plasma etching of SiO_2 in C_2F_6, CHF_3 and C_4F_8 gas chemistries have been developed and incorporated into the Monte Carlo Feature Profile Model (MCFPM) which was modified to address these two-phase systems. The reaction mechanism was validated by comparison to experiments by others for etching of PS and SS. We found that the etch rates (ER) for PS are generally higher than that of SS due to the inherently lower mass fraction. Mass

corrected etch rates of PS can be larger or smaller than those for SS depending on the degree of pore filling by polymer and degree of ion activated chemical sputtering. Pore filling is particularly important for PS having open networks with large pores and high porosities. We found little dependence of the taper of high aspect ratio profiles on the average pore radius and porosity. However, the profile changes from tapered to bowed as the interconnectivity of the porous network increases. Scaling laws for profile shapes are otherwise similar for both SS and PS.

Cleaning of residual polymer from trenches following etching and the deposition of a continuous barrier layer are critical processes for integration PS as ILDs. To investigate these issues, a reaction mechanism for plasma stripping of residual fluorocarbon polymer using oxygen-based chemistries has been developed and incorporated into the MCFPM. The reaction mechanism was validated by comparison to experiments for blanket plasma etching of polytetrafluoroethylene using Ar/O_2 chemistries. The etching of organic polymers in oxygen plasmas is ion-assisted, having an oxygen limited regime and an ion energy limited regime. Plasma stripping of residual fluorocarbon polymers from SS was less efficient at higher aspect ratios. Stripping was less efficient from PS trenches having large average pore radius and high interconnectivity, as compared to SS. Cu ionized metal physical vapor deposition (IMPVD) was also investigated as a surrogate for barrier coating in SS and PS trenches. Thin film deposition was less conformal for PS with closed pore networks. Thicker Cu barrier films were required for interconnected PS to avoid pin-hole formation.

ACKNOWLEDGMENTS

I would like to express my sincere gratitude to my advisor, Prof. Mark J. Kushner, whose help and guidance has been the scaffold of this work. I am profoundly thankful to him for being patient with me and helping me solve all the difficulties in my work and otherwise. All my knowledge and understanding in plasma physics, I attribute to him.

My sincere thanks go to the professors of my final dissertation committee, Vinay K. Gupta, David N. Ruzic, and Michael S. Strano for their thoughtful comments. I would like to acknowledge the support of the Semiconductor Research Corporation (SRC), National Science Foundation (NSF) and SEMATECH.

I am also thankful to my fellow members in the Computational Optical and Discharge Physics Group: Ron Kinder, Da Zhang, Junqing Lu, Rajesh Dorai, Brian Lay, Alex Vasenkov, Kelly Collier, Pramod Subramonium, Kapil Rajaraman, Vivek Vyas, Ananth Bhoj, Rick Moss, David Stafford, Ramesh Arakoni and Ankur Agarwal.

My aunt Bhavani and my parents, Savithri and Sankaran, have showed endless love and encouragement throughout my career, without which I would not be the person I am. My sister Aparna has shared all my problems and has always helped me with timely advice and constructive criticism, and my grandmother's faith in me has always motivated me. My aunt Meena and her family have always supported me in all my endeavors. I thank them all for all their help and support, which have helped in shaping my dreams and efforts into this work. This note would be incomplete if I didn't thank all those who made my stay in Champaign-Urbana pleasant and memorable. Finally I thank my other friends and relatives for their support.

TABLE OF CONTENTS

1. INTRODUCTION

1.1 Plasma Processing for Semiconductor Applications

Moore's law has characterized the microelectronics industry since 1980, when Gordon Moore observed that the number of transistors in microprocessors doubles every 18 months. Moore's law is illustrated by the growth of the number of transistors in logic chips over the years in Fig. 1.1. The industry has obeyed Moore's law for over 12 generations.[1] This has lead to smaller devices and features and improved capabilities over the years. The process of fabricating these devices involves hundreds of steps while critical dimensions have shrunk to 10's of Å (a few atomic monolayers). As microelectronic device sizes continue to shrink, there is a propensity for increased delay in signal propagation in interconnect wiring due to higher resistances in the lines (smaller diameter wires) and larger capacitance between the lines (smaller spacing).[2] Low dielectric constant (low-k) materials as the interlayer dielectrics (ILD) and Cu as the interconnects are being investigated to reduce this delay. Examples of nine-level copper interconnect with low-k ILD as current state of the art are shown in Fig. 1.2.

The shift to smaller devices and newer materials has placed emphasis on precise and superior processing of semiconductors. The strict design rules necessary in modern processes have led to the replacement of wet chemical etching with dry plasma etching, and to improvements of the plasma etching process. Plasma processing of semiconductors (plasma etching, plasma enhanced chemical vapor deposition (PECVD) is widely used to meet such needs.[3]

Plasma etching has the advantage of obtaining anisotropic features as illustrated in Fig. 1.3. Anisotropic etching by a plasma is attributed to its abundance of energetic etch reactants

(radicals and ions) and to the vertically oriented ion bombardment of the wafer surface. As a result, the minimum controllable sizes are much smaller than what wet etching can achieve. Primarily for this reason, plasma etching has dominated the commercial market and has become an important topic of research. In the case of wet etching the neutrals reacts in all directions of contact. As a result wet processes produce isotropic profiles (undercutting) as shown in Fig. 1.3. When overetching occurs, the minimum feature size is limited.

A plasma is a partially ionized gas in an electrically quasi-neutral state. When an electrical field is applied to a gas, free electrons are accelerated by the field. Because the mass of an electron is much smaller than that of a neutral species, electrons lose almost no energy during electron-neutral momentum transfer collisions. As a result, the free electrons are accelerated to very high energies, typically several electron volts (eVs). When electron energies exceed the threshold energies of inelastic collisions (ionization or excitation), electron impact of neutral species produce electron-ion pairs and neutral radicals. By choosing appropriate feed gas chemistries and with an astute choice of reactor and processing conditions, desired electron-ion pairs and neutral radicals can be extracted towards a plethora of plasma processing applications.

Conventionally plasmas are electrically driven by either capacitive coupling (capacitively coupled plasmas-CCPs) or inductive coupling (inductively coupled plasmas-ICPs). A schematic of a CCP reactor is shown in Fig. 1.4. In CCP reactors a radio frequency (rf) voltage source (a few to 10's of MHz) drives current through a low-pressure gas between two electrodes and deposits power of 50–2000 W. The gas breaks down to form a plasma, which is usually weakly ionized with a fractional ionization of about 10^{-5}. The operating pressures are about 10–1000 mTorr. The plasma density varies from 10^{9}–10^{11} cm^{-3} and electron temperature between 1–5 eV. In high-density plasmas such as ICP reactors, shown in Fig 1.5, the power is coupled to the

plasma through an antenna, which acts as a transformer. The plasma acts as a single-turn conductor that is coupled to a multi turn non-resonant rf coil around the dielectric discharge chamber. ICPs operate with a fractional ionization of about 10^{-3}, with operating pressures of 0.5–50 mTorr. Plasma density varies from 10^{10}–10^{12} cm^{-3} and electron temperature between 2–7 eV. To control ion energy to the substrate in ICPs, the electrode on which the wafer is placed can be independently driven by a capacitively coupled rf source. The ions created in the bulk plasma by inductive coupling are accelerated in the sheath near the wafer by applying an rf bias on the electrode and is shown in Fig. 1.6. This is the cause of the anisotropic distribution of ions incident upon the wafer.

1.2 Plasma Modeling

As plasma processing systems have increased in complexity and cost, it has become prohibitive to develop new reactors by only physical experimentation. The development of plasma equipment models (PEMs) for investigating chemical, physical and engineering scaling issues for plasma processing has significantly advanced in recent years. Use of these models allows costly physical development and manufacturing to be reduced as seen in almost every technological industry.

Initially, plasma modeling was limited to global and one-dimensional (1-D) models based on limited physics such as drift-diffusion. Two-dimensional (2-D) models are now being used by the industry to design plasma processes and equipment. PEMs in 2-D have been developed with the goals of both investigating basic physical processes and for use in the design of plasma equipment.[4] One of the first 2-D models for rf discharges was developed by Tsai and Wu in 1990.[5] Pitchford *et al.* also produced a 2-D numerical model demonstrating the effects of dc self

bias which compared well to experiments for parallel plate plasma systems.[6] Dalvie *et al.* also produced a drift-diffusion-based 2-D model and described the effects of enhanced ionization for large radii in parallel plate systems.[7] Lymberopoulos and Economu developed the first finite element model of a parallel plate system and demonstrated comparison to the Gaseous Electronics Conference (GEC) reference cell.[8] Goedheer *et al.* developed a 2-D drift-diffusion model of a parallel plate argon discharge which utilized semi-implicit solutions of Poisson's equation to accelerate solution speed.[9,10] Ventzek *et al.* produced the first 2-D model of inductively coupled discharge and included capacitive coupling effects and later included the effects of momentum for ions and neutrals.[11,12] Kortshagen *et al.* developed a model utilizing a nonlocal kinetic model for the electrons and demonstrating the deviation from equilibrium fluid models.[13] Economu *et al.* developed the first direct simulation Monte Carlo (DSMC) model of heavy body transport in an HDP system utilizing fluid model results to describe the plasma distributions.[14] Recently, Panagopoulos *et al*. developed a three-dimensional (3-D) finite element fluid model for studying azimuthal asymmetries and their effect on etch uniformity in ICPs.[15]

The equipment scale models are typically linked to feature scale models (10's of Å - micron) to predict the evolution of the properties of microelectronic features. Computational models to describe topography evolution of a surface have been used in other fields as well. One method of topography modeling, described as the "string" or "geometric" method, involves solving partial differential equations. For example, SPEEDIE, a string model developed by Ulacia and McVittie has been used to examine etching and deposition related to metallization processes in VLSI fabrication.[16] Another string model, EVOLVE, developed by Cale *et al.* has also the capability to simulate deposition in VLSI fabrication.[17] Monte Carlo based methods are

more straightforward in modeling feature profile evolution. May *et al.* developed a sputter etch model for argon impinging on silicon showing the effects of ion angular distribution on trench undercutting.[18] Hwang and Giapis modeled the effects of nonuniform charging within etch feature profiles and the development of horizontal "notch" formation using a parallel Monte Carlo algorithm.[19-22] Many Monte Carlo based feature profile models for chlorine etching of polysilicon have been investigated.[23-26]

1.3 Research on Plasma Processing of Low-k Dielectrics

The increase in the area density of devices and the reduction of device sizes in microelectronics have resulted in an increase in the RC delay time in interconnect wiring.[2] Low-k materials are being investigated as ILDs in interconnect wiring to reduce this delay. Low-k dielectrics can be broadly classified as organic, inorganic, and hybrid and the classification is shown in Fig. 1.7.[27] Organic materials such as polytetrafluoroethylene (PTFE) and parylene are etched in oxygen based plasmas (O_2/Ar and O_2/N_2).[28-30] Inorganic dielectrics typically involve SiO_2 based materials which are etched in fluorocarbon plasmas.[31,32] Porous SiO_2 (PS) is one such inorganic low-k material. Successful integration of PS films as an ILD depends on its electrical, thermo-mechanical, chemical and structural properties. Of interest in this work are their structural properties, which are porosity, average pore radius and pore interconnectivity.[33]

Measurements of PS characteristics using small angle x-ray spectroscopy (SAXS) combined with x-ray reflectivity (XRR) and ellipsometric porosimetry (EP) indicate that the typical porosities used for ILD are 20-80%.[34,35] The dielectric constant is generally reduced in proportion to the mass density, which is inversely proportional to the porosity. PS with an interconnected pore structure typically experiences an increase in dielectric constant during processing due to a partial collapse of the pore structure.[34] The connectivity of pores in

industrially relevant materials can be large. For example, Wu *et al*. utilized small angle neutron spectroscopy (SANS) to determine that 22% of the pores of a 900 nm thick PS thin film (AlliedSignal Nanoglass^{TM} K2.2-A10B) have connective paths to the free surface.[34] Gidley *et al*. measured 100% pore interconnectivity in a methylsilsesquioxane (MSQ) film (k = 2.5) using positron annihilation lifetime spectroscopy (PALS).[36] Pore measurements using SANS and PALS among other techniques predict typical radii to be around 2-20 nm.[34,37]

The successful integration and reliability of low-k dielectrics as ILD depends in part on its compatibility with current processing techniques.[38] The main process steps of interest are photolithography exposure and development, plasma etching to define vias and trenches, cleaning of the feature and the deposition of a barrier coating and seed layer for subsequent electrochemical deposition. Standaert *et al*. have investigated fluorocarbon etching of fluorinated SiO_2, hydrogen silsesquioxane (HSQ) and MSQ low-k films using an ICP.[39] Comparisons were made to the etching of solid SiO_2 (SS) in CHF_3 and C_4F_8 chemistries. The etch rate of PS was in general higher than that of SS due to the lower mass densities of PS. However in highly polymerizing environments they found that the ER of PS was suppressed compared to SS. They also investigated profile evolution of HSQ and MSQ etched in a CHF_3 plasma and found similar scaling laws as for SS. [27,39]

Fluorocarbon etching of both PS and SS proceeds through the formation of an overlying fluorocarbon polymer on the SiO_2.[40] C_xF_y radicals are the precursors to the polymer layer which regulates the delivery of activation energy and the transport of neutral and ion fluxes to the underlying materials.[41] Upon delivery of activation energy to the polymer-SiO_2 interface, the oxygen in SiO_2 reacts with the fluorocarbon species in the polymer to release etch products such as COF_x, thereby consuming the polymer.[42] This leads to a thinner polymer layer during SiO_2

etching compared to Si etching.[43] The thickness of polymer layer is the main source of selectivity between different materials such as SiO_2, Si_3N_4 and Si as ER generally scales inversely with the polymer thickness.[44] Polymer is also consumed by energetic ion sputtering.[45,46]

Post etch processing of ILDs typically involves stripping of the etch residues and photoresist followed by a barrier coating for Cu deposition. Post etch cleaning of the trenches and the vias reduces the contact resistance between the plasma-exposed surfaces and the subsequent deposited metal layers.[47] In the case of organic low-k materials which are etched using oxygen containing plasmas, there is a residual oxidized layer on the surface, which is typically cleaned by Ar sputtering.[27] In the case of inorganic low-k materials such as porous silica (PS) the residual fluorocarbon polymer remaining after etching and the photo-resist are typically removed using O_2 based chemistries (among others).[48-50]

In the case of plasma etching of silicon based dielectrics, if the residual fluorocarbon polymer is not totally removed prior to the subsequent metal deposition for a barrier coating or seed layer, the sputtered metal atoms could mix with the polymer to form a high resistance material and thus increase the contact resistance.[51] The formation of this high resistance material also raises reliability concerns.[51] In the case of Si substrates the residual polymer results in defects at the metal-Si interface leading to a high leakage current.[47] As a result, the removal of these residues is critical for device integration.

Several wet and dry methods for removing such residues have been previously investigated.[52-55] Both wet and dry plasma cleaning chemistries have typically involved oxidizing chemistries to remove the residual fluorocarbons.[48,51,54] Wet cleaning methods include RCA cleans, HF dips, H_2SO_4/H_2O_2 and amine based solvents.[47] However with decreases in

feature sizes, wet strip processes have been found to be less effective. In addition, wet strip processes often have higher process costs and disposal of the solvents poses significant environmental hazards.[56]

As an alternative to wet stripping, plasma cleaning methods have been extensively investigated.[56,57] In this regard, oxygen plasmas are typically used and are efficient in stripping residual polymer from SS. Remote oxygen plasmas are often preferred with the goal of minimizing plasma damage of the substrate.[48] The removal of organic polymer using oxygen plasmas has other widespread applications in semiconductor processing as well. For example, Ar/O_2 chemistries are widely used for lithography in processes such as resist thinning. This technique is useful in reducing the gate length without increasing the complexity of the lithography.[58,59] Photoresist ashing is also performed using O_2 chemistries to remove the masking photoresist layer. [60] O_2 based chemistries also find applications in the etching of organic and hybrid low-k dielectrics, which are patterned using SiO_2 or SiN_x hardmasks.[28,29]

There are potential drawbacks to using O_2 plasmas for cleaning of low-k PS materials such MSQ and HSQ.[27] Typically oxygen plasmas oxidize these materials into SiO_2-like material and this results in an increase in their dielectric constants.[50] As a result other alternate stripping techniques, which use H_2 based chemistries and NF_3/Ar are being considered.[55,56,61]

Post etch processing of ILD also involves deposition of a thin film of metal barrier layer and a seed layer deposition subsequent to the residual polymer cleaning and preceding the metallization.[62,63] The deposition of thin films on porous materials is challenging as the pore morphology may have significant effects on the functionality, conformality, and reliability of the capping barrier layers and the metal seed layer.[64] Deposition of such thin barrier and seed films

is typically achieved by means of physical vapor deposition (PVD), chemical vapor deposition (CVD), or atomic layer deposition (ALD).[64,65]

During the deposition of thin films onto a meso-connected (interconnected) porous network, the transport of the deposition reactants into the pore chains is inefficient, which could result in an exposed pore being unabridged, a phenomenon referred to as creation of pin holes.[38] Meso-connectivities have dimensions (2-20 nm), which are comparable to the average pore radius. Micro-connectivity (closed pores) consists of atomic level connectivities inherent to the material and whose dimensions (a few Å) are typically small in comparison to the average pore radius. As such, pinholes due to atomic level connectivities are typically not a problem. For example, deposition of a TaN barrier coating onto an MSQ based film with meso-connectivities and average pore radius 3-5 nm using PVD was found to have pinholes, which was detected by an increase in the sheet resistance.[64] The presence of a partially porous diffusion barrier can also lead to contamination during the subsequent metallization process.[66] During thin film deposition onto interconnected porous substrates using CVD and ALD, the precursors can penetrate and deposit material through the entire dielectric network, which also affects the integrity of the film.[65] As a result, sealing of interconnected pore networks and conformal deposition onto closed pore networks during barrier layer depositions is important to the implementation of PS as ILDs.

The goal of this work was to investigate the suitability of PS as an ILD. To this end, we developed a surface reaction mechanism for etching of SS and PS in fluorocarbon plasmas, investigated etching of PS in fluorocarbon plasmas and compared the results with etching of SS. As a second step, cleaning of the residual fluorocarbon polymer from the etched PS trenches was investigated. A surface reaction mechanism for etching of fluorocarbon polymer in O_2 plasmas

was developed and applied to the stripping of residual fluorocarbon and resist removal. To complete the picture, deposition of a barrier coating onto the cleaned trenches using Cu IMPVD was investigated. Problems posed by the pore morphologies and PS film characteristics during the various processing steps were quantified. Remedies to these problems in the form of optimal process conditions have been suggested wherever possible. The effect of PS film properties, in particular the morphological properties such as the pore diameter, porosity and the interconnectivity, were quantified and suitable pore structures have been suggested.

1.4 Summary

In Chapter 2, a detailed description of the Hybrid Plasma Equipment Model (HPEM), which is the equipment scale model used in this work, is presented. The different modules of the HPEM and the physics used for our simulations are explained. The Plasma Chemistry Monte Carlo Module (PCMCM) in the HPEM generates the Energy and Angular Distributions (EADs) of the different ion and neutral species on the wafer. Typical results from the HPEM and PCMCM are presented.

In Chapter 3, the Monte Carlo Feature Profile Model (MCFPM) used for the profile simulations in this work is explained in detail. The MCFPM uses the EADs from the PCMCM as input. A two-phase algorithm developed for investigating porous dielectrics has been incorporated into the MCFPM. Surface reaction mechanisms developed for fluorocarbon etching of SiO_2/Si and for etching of fluorocarbon polymer in O_2 plasma are described. The reaction mechanism for Cu IMPVD developed by Lu *et al*. has been adopted to studying deposition onto PS films and is summarized.[67] Typical results for integrated modeling (etch, strip and fill) of SS and PS using the MCFPM are presented.

In Chapter 4, fluorocarbon etching of SS and PS is discussed. Validation of the surface reaction mechanism for fluorocarbon etching and the two-phase model discussed in Chapter 3 by comparison to experiments is presented. [68,69] Results from profile simulations of PS etching in CHF_3 plasma are explained. We found that the ER of SS increases as a function of self-bias after a threshold, and saturates at high biases. Etching of PS follows similar trends as SS with ERs in general being higher due to the inherent lower mass densities of PS. However the mass corrected etch rates of PS depend on the filling of pores by polymer, which can either enhance or reduce the ERs. Pore filling is most significant for interconnected porous networks having large pores and high porosities. Profiles become less tapered with increasing bias and decreasing polymerizing fluxes. The taper of profiles has little dependence on the pore radius and porosity; however open pore networks tend to produce bowed profiles.

In Chapter 5, post-etch processing, namely, strip of residual fluorocarbon and photoresists and deposition of barrier coating is presented. Validation of the surface reaction mechanism for etching of fluorocarbon polymer in O_2 plasmas discussed in Chapter 3, based on results for blanket etching of PTFE in Ar/O_2 plasma is presented.[28] This surface reaction mechanism has been extended to studying stripping of residual fluorocarbon polymer from etched trenches. Copper IMPVD, developed earlier for studying trench filling in nonporous films, was investigated for PS as a surrogate to deposition of barrier coating or seed layer.[67] Based on experimental trends, we found that there is little etching of fluorocarbon polymer in the absence of simultaneous O atom and energetic ion fluxes and our reaction mechanism reflects that. Stripping was found to be less effective for interconnected PS films with larger average pore radius and porosities due to there being unfavorable view angles of the incident energetic fluxes. This effect was more pronounced for vias and trenches having high aspect ratios.

Unfavorable view angles also resulted in non-conformal metal deposition in closed pore networks and creation of pinholes in interconnected networks during Cu IMPVD.

In Chapter 6, etching of PS and SS films in complex gas mixtures ($C_4F_8/Ar/O_2$) is presented. The reaction mechanisms developed for fluorocarbon etching of SiO_2 based dielectrics and oxygen etching of organic polymer were coupled and the coupled reaction mechanism was validated by comparison to experiments for both blanket and profile etching of SS in ICP and Magnetically Enhanced Reactive Ion Etching (MERIE) reactors. Blanket etching of SS and PS films showed a maximum in etch rates for both Ar and O_2 additives. Profile simulations in the MERIE reactor showed higher resist etching for larger Ar mole fractions and larger power deposition, which was a result of increased sputtering of the resists. Etch stop due to thick sidewall passivation was observed for etching of high aspect ratio features in both C_4F_8 and C_4F_8/Ar ICPs. O_2 additives and lower pressures decreased the sidewall thickness and helped etching of such features.

In Chapter 7, conclusions are made about the overall significance of the work and recommendations for future work are suggested.

1.5 Figures

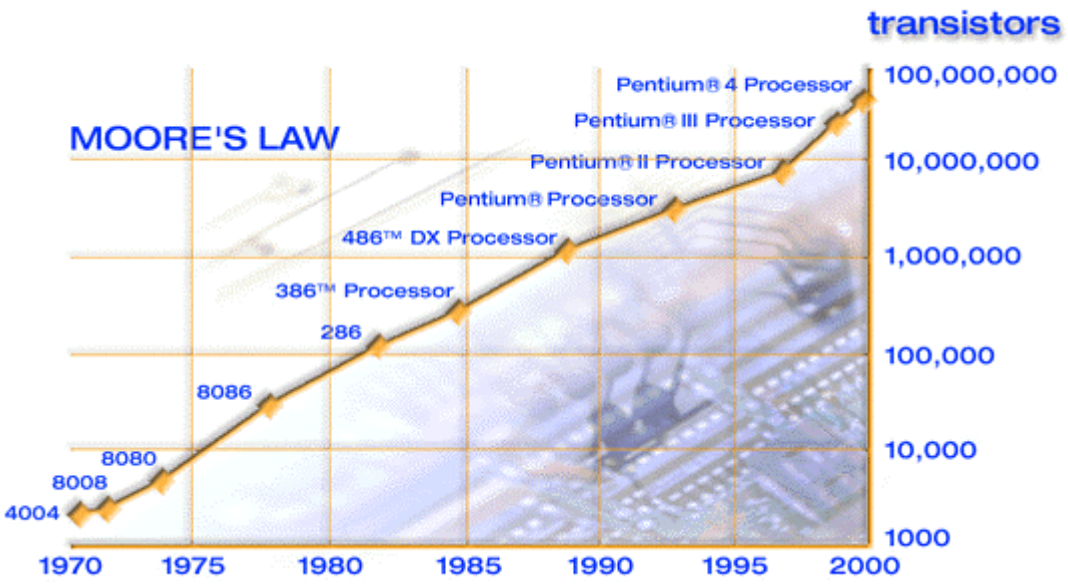

Fig. 1.1. Graphical depition of Moore's law.[70]

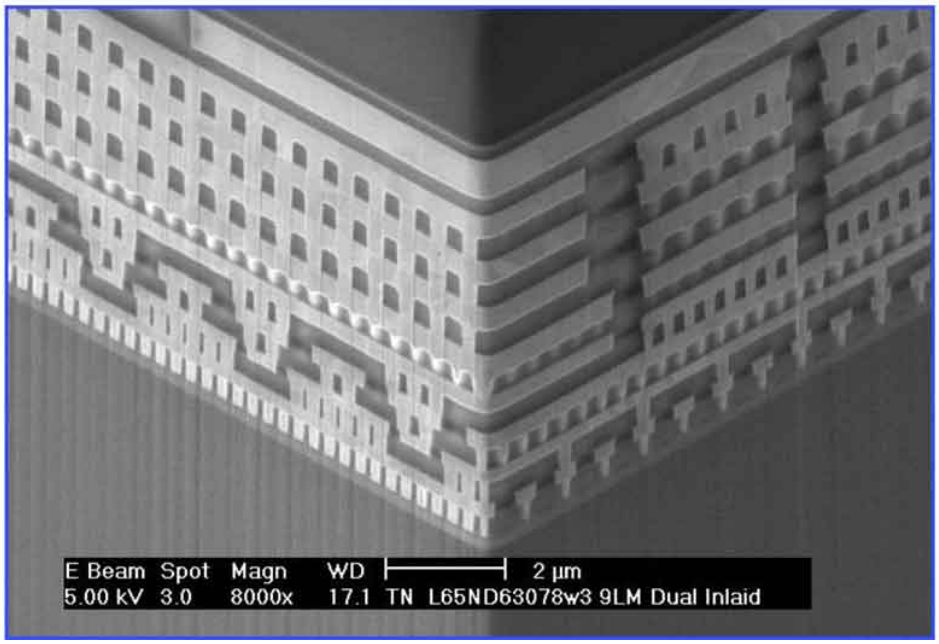

a)

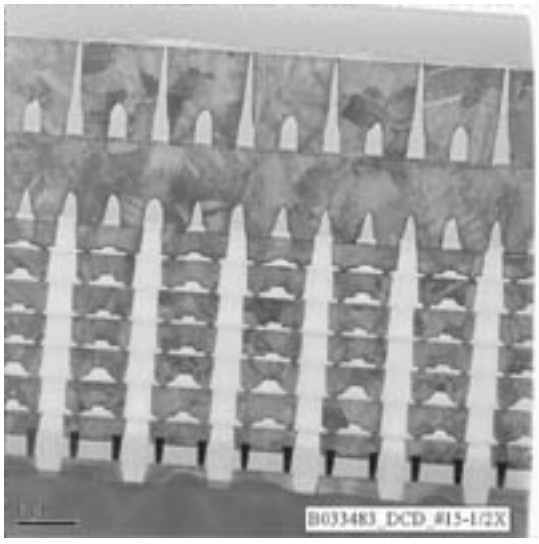

b)

Fig. 1.2. Nine level copper interconnects with low-k ILD (a) Motorola's HiPerMOS7 SOI [71] and (b) Taiwan Semiconductor Manufacturing Company (TSMC) integrated porous ILD.[72]

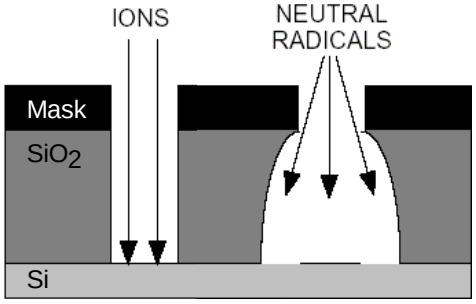

Figure 1.3. The ions are directed to the bottom of the trench, which helps in attaining high aspect ratio features. The neutral radicals have an isotropic profile and results in isotropic etch profile.

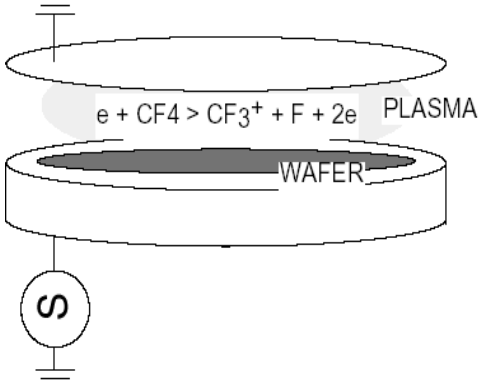

Figure 1.4. Schematic of a typical capacitively coupled plasma (CCP) reactor.

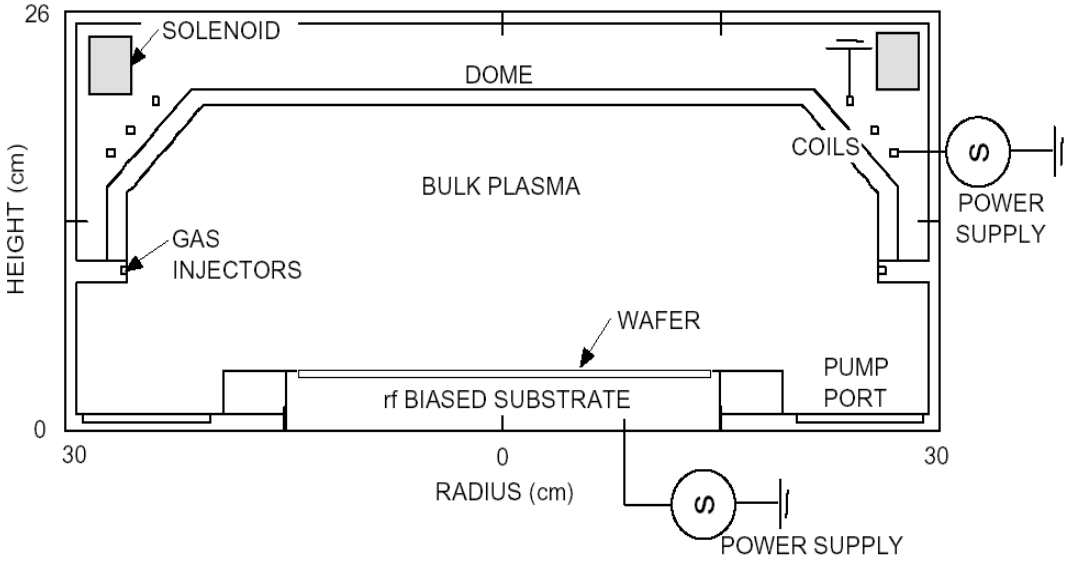

Fig. 1.5. Schematic of a typical Inductively Coupled Plasma (ICP) reactor.

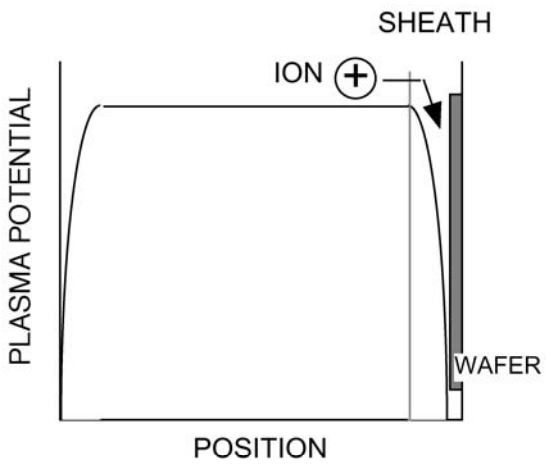

Figure 1.6 Schematic of plasma potential. Ions accelerated in the sheath are capable of initiating etching and deposition.

Inorganic	Organic	Hybrid
SiO_2	Parylene-N	Benzocyclobutene (BCB)
$SiO_{2-\delta}F_\gamma$	Parylene-F	Methyl silsesquioxane (MSQ)
Hydrogen silsesquioxane (HSQ)	Polyarylene ether (PAE-2)	Porous MSQ
Porous HSQ	Polytetrafluoroethylene (PTFE)	Organosilicate glasses (OSG)
Xerogels*	SiLK/porous SiLK	
	Fluorinated polyimide (FPI)	
	FLARE/Porous FLARE	
Fluorocarbon etching chemistry	Oxygen etching chemistry	Fluorocarbon and/ or oxygen chemistry
Resist mask	SiO_2 or Si_3N_4 mask	SiO_2 or Si_3N_4 mask

*contain residual organic groups and could therefore also be listed under hybrid materials

Fig. 1.7: Classification of low dielectric constant materials used in microelectronic fabrication.[27]

1.6 References

[1] C. Y. Chang and S. M. Sze, *ULSI Technology* (McGraw-Hill, 1996).

[2] S.-J. Wang, H.-H. Park, and G.-Y. Yeom, Jap. J. Appl. Phys. **39,** 7007 (2000).

[3] J. W. Coburn and H. F. Winters, Annu. Rev. Mater. Sci. **13,** 91 (1983).

[4] G. DiPeso, V. Vahedi, D. W. Hewett, and T. D. Rognlien, J. Vac. Sci. Technol. A **12,** 1387 (1994).

[5] J. H. Tsai and C. Wu, Phys. Rev. A **41,** 5626 (1990).

[6] L. C. Pitchford, P. Belenguer, and J. P. Boeuf, *Microwave Discharges: Fundamentals and Applications***,** 359 (1993).

[7] M. Dalvie, M. Surendra, and G. S. Selwyn, Appl. Phys. Lett. **62,** 3207 (1993).

[8] D. P. Lymberopoulos and D. J. Economou, J. Appl. Phys. **73,** 3668 (1993).

[9] J. P. D. Passchier and W. J. Goedheer, J. Appl. Phys. **74,** 3744 (1993).

[10] W. J. Goedheer, P. M. Meijer, J. Bezemer, J. D. P. Passchier, and W. G. J. H. M. van Sark, IEEE Trans. Plasma Sci. **23,** 644 (1995).

[11] P. L. G. Ventzek, R. J. Hoekstra, T. J. Sommerer, and M. J. Kushner, Appl. Phys. Lett. **63,** 605 (1993).

[12] P. L. G. Ventzek, R. J. Hoekstra, T. J. Sommerer, and M. J. Kushner, J. Vac. Sci. Technol. B **12,** 461 (1994).

[13] U. Kortshagen, I. Pukropski, and L. D. Tsendin, Phys. Rev. E **51,** 6063 (1995).

[14] D. J. Economou, T. J. Bartel, R. S. Wise, and D. P. Lymberopoulos, IEEE Trans. Plasma Sci. **23,** 581 (1995).

[15] T. Panagopoulos, D. Kim, V. Midha, and D. Economou, J. Appl. Phys. **91,** 2687 (2002).

[16] J. I. Ulacia F. and J. P. McVittie, J. Appl. Phys. **65,** 1484 (1989).

[17] T. S. Cale, G. B. Raupp, and T. H. Gandy, J. Appl. Phys. **68,** 3645 (1990).

[18] P. W. May, D. F. Klemperer, and D. Field, J. Appl. Phys. **73,** 1634 (1993).

[19] G. S. Hwang and K. P. Giapis, J. Appl. Phys. **81,** 3433 (1997).

[20] G. S. Hwang and K. P. Giapis, J. Appl. Phys. **82,** 572 (1997).

[21] G. S. Hwang and K. P. Giapis, Phys. Rev. Lett. **79,** 845 (1997).

[22] G. S. Hwang and K. P. Giapis, Appl. Phys. Lett. **71,** 29282930 (1997).

[23] J. P. Chang, A. P. Mahorowala, and H. H. Sawin, J. Vac. Sci. Technol. A **16,** 217 (1998).

[24] A. P. Mahorowala, H. Sawin, R. Jones, and A. H. Labun, J. Vac. Sci. Technol. B **20,** 1055 (2002).

[25] A. P. Mahorowala and H. Sawin, J. Vac. Sci. Technol. B **20,** 1084 (2002).

[26] R. J. Hoekstra, M. J. Grapperhaus, and M. J. Kushner, J. Vac. Sci. Technol. A **15,** 1913 (1997).

[27] G. S. Oehrlein, T. E. F. M. Standaert, and P. J. Matsuo, in *Solid State Technology*; *Vol. May 2000* (2000), p. 125.

[28] T. E. F. M. Standaert, P. J. Matsuo, X. Li, G. S. Oehrlein, T. M. Lu, R. Gutmann, C. T. Rosenmayer, J. W. Bartz, J. G. Langan, and W. R. Entley, J. Vac. Sci. Technol. A **19,** 435 (2001).

[29] D. Fuard, O. Joubert, L. Vallier, and M. Bonvalot, J. Vac. Sci. Technol. B **19,** 447 (2001).

[30] D. Fuard, O. Joubert, L. Vallier, M. Assous, P. Berruyer, and R. Blanc, J. Vac. Sci. Technol. B **19,** 2223 (2001).

[31] P. Ho, J. E. Johannes, R. J. Buss, and E. Meeks, J. Vac. Sci. Technol. A **19,** 2344 (2001).

[32] M. Matsui, F. Uchida, M. Kojima, T. Tokunaga, F. Yano, and M. Hasegawa, J. Vac. Sci. Technol. A **20,** 117 (2002).

[33] W. D. Gidley, W. E. Frieze, T. L. Dull, J. Sun, A. F. Yee, C. V. Nguyen, and D. Y. Yoon, Appl. Phys. Lett. **76,** 1282 (2000).

[34] W. Wu, W. E. Wallace, L. E. K., G. W. Lynn, C. G. Glinka, T. E. Ryan, and H. Ho, J. Appl. Phys. **87,** 1193 (2000).

[35] M. R. Baklanov, K. P. Mogilnikov, V. G. Polovinkin, and F. N. Dultsev, J. Vac. Sci. Technol. B **18,** 1385 (2000).

[36] W. D. Gidley, W. E. Frieze, T. L. Dull, A. F. Yee, T. E. Ryan, and H. Ho, Phys. Rev. B **60,** R5157 (1999).

[37] M. P. Petkov, M. H. Weber, K. G. Lynn, K. P. Rodbell, and S. A. Cohen, Appl. Phys. Lett. **74,** 2146 (1999).

[38] K. Maex, M. R. Baklanov, D. Shamiryan, F. Iacopi, S. H. Brongersma, and Z. S. Yanovistskaya, J. Appl. Phys. **93,** 8793 (2003).

[39] T. E. F. M. Standaert, P. J. Matsuo, S. D. Allen, G. S. Oehrlein, and T. J. Dalton, J. Vac. Sci. Technol. A **17,** 741 (1999).

[40] A. J. Bariya, C. W. Frank, and J. P. McVittie, J. Electrochem. Soc. **137,** 2575 (1990).

[41] T. E. F. M. Standaert, M. Schaepkens, N. R. Rueger, P. G. M. Sebel, G. S. Oehrlein, and J. M. Cook, J. Vac. Sci. Technol. A **16,** 239 (1998).

[42] M. Matsui, T. Tatsumi, and M. Sekine, J. Vac. Sci. Technol. A **19,** 2089 (2001).

[43] G. S. Oehrlein and J. F. Rembetski, IBM J. Res. Develop. **36,** 140 (1992).

[44] N. R. Rueger, J. J. Beulens, M. Schaepkens, M. F. Doemling, J. M. Mirza, T. E. F. M. Standaert, and G. S. Oehrlein, J. Vac. Sci. Technol. A **15,** 1881 (1997).

[45] M. Matsui, T. Tatsumi, and M. Sekine, J. Vac. Sci. Technol. A **19,** 1282 (2001).

[46] K. Miyata, M. Hori, and T. Goto, J. Vac. Sci. Technol. A **15,** 568 (1997).

[47] S. J. Fonash, J. Electrochem. Soc. **137,** 3885 (1990).

[48] H. Seo, S. B. Kim, J. Song, Y. Kim, H. Soh, Y. C. Kim, and H. Jeon, J. Vac. Sci. Technol. B **20,** 1548 (2002).

[49] K. Ueno, V. M. Donnelly, and Y. Tsuchiya, J. Vac. Sci. Technol. B **16,** 2986 (1998).

[50] D. Shamiryan, M. R. Baklanov, S. Vanhaelemeersch, and K. Maex, J. Vac. Sci. Technol. B **20,** 1923 (2002).

[51] Y. Wang, S. W. Graham, L. Chan, and S. Loong, J. Elctrochem. Soc **144,** 1522 (1997).

[52] G. S. Oehrlein, G. J. Scilla, and S. Jeng, Appl. Phys. Lett. **52,** 907 (1988).

[53] D. K. Schroder, *Semiconductor Material and Device Characterization* (John Wiley & Sons, Inc., New York, 1990).

[54] S. D. Gendt, P. Snee, I. Cornelissen, M. Lux, R. Vos, P. W. Mertens, D. M. Knotter, and M. M. Heyns, Symp. VLSI. Technol. Dig. Tech. Papers**,** 168 (1998).

[55] H. Ying, J. P. Barnak, Y. L. Chen, and R. J. Nemanich, Mat. Res. Soc. Symp. Proc **386,** 285 (1995).

[56] A. Somashekhar, H. Ying, P. B. Smith, D. B. Aldrich, and R. J. Nemanich, J. Electrochem. Soc. **146,** 2318 (1999).

[57] D. Louis, E. Lajoinie, F. Pires, W. M. Lee, and D. Holmes, Mic. Engg **41/42,** 415 (1998).

[58] F. Greer, J. W. Coburn, and D. B. Graves, J. Vac. Sci. Technol. A **18,** 2288 (2000).

[59] C.-Y. Sin, B.-H. Chen, W. L. Loh, J. Yu, P. Yelehanka, A. See, and L. Chan, J. Vac. Sci. Technol. B **20,** 1974 (2002).

[60] F. Greer, L. Van, D. Fraser, J. W. Coburn, and D. B. Graves, J. Vac. Sci. Technol. B **20,** 1901 (2002).

[61] H. Cerva, E. G. Mohr, and J. Oppolzer, J. Vac. Sci. Technol. B **5,** 590 (1992).

[62] J. A. Cunningham, Semicon. Int **23,** 97 (2000).

[63] E. J. O'Sullivan, A. G. Schrott, P. M, C. J. Sambucetti, J. R. Marino, P. J. Bailey, S. Kaja, and K. W. Semkow, IBM J. Res. Develop. **42,** 607 (1998).

[64] F. Iacopi, Z. Tokei, M. Stucchi, S. H. Brongersma, D. Vanhaeren, and K. Maex, Mic. Engg **65,** 123 (2003).

[65] W. Besling, A. Satta, J. Schuhmacher, T. Abell, V. Sutcliffe, A. M. Hoyas, G. Beyer, D. Gravesteijn, and K. Maex, Proc. IITC**,** 288 (2002).

[66] F. Iacopi, Z. Tokei, M. Stucchi, F. Lanckmans, and K. Maex, IEEE Electron. Dev. Lett **24,** 147 (2003).

[67] J. Lu and M. J. Kushner, J. Vac. Sci. Technol. A **19,** 2652 (2001).

[68] T. E. F. M. Standaert, E. A. Joseph, G. S. Oehrlein, A. Jain, W. N. Gill, P. C. J. Wayner, and J. L. Plawsky, J. Vac. Sci. Technol. A **18,** 2742 (2000).

[69] M. Schaepkens, T. E. F. M. Standaert, N. R. Rueger, P. G. M. Sebel, G. S. Oeherlein, and J. M. Cook, J. Vac. Sci. Technol. A **17,** 26 (1999).

[70] Intel research in Si, *http://www.intel.com/research/silicon/mooreslaw.htm* .

[71] Fred Huang, Motorola (private communications, 2003).

[72] L. Peters, in Semiconductor International, Nov 2003, (2003).

2. HYBRID PLASMA EQUIPMENT MODEL

2.1. Introduction

The Hybrid Plasma Equipment Model (HPEM) has been developed at the University of Illinois for simulating low-temperature, low-pressure plasma processes such as plasma etching and plasma-assisted deposition.[1-22] Two important parameters for plasma processes include the power source and the gas source. The power source, typically capacitively or inductively coupled, generates electromagnetic fields that accelerate electrons and drive electron impact processes to produce the plasma. The partially ionized plasma, as a conductive body, is capable of affecting the electric fields inside the process chamber.

The HPEM addresses plasma physics and plasma chemistry in a modular fashion. The main modules are the Electromagnetics Module (EMM), the Electron Energy Transport Module (EETM), and the Fluid-chemical Kinetic Module (FKM). Starting with an initial estimate of plasma properties, the EMM computes the inductively coupled electric fields determined by the inductive coils, and the magnetostatic fields induced by permanent magnets or dc current loops. These fields are then used in the EETM to obtain electron impact source functions and transport coefficients. This is achieved by either solving the electron energy equation or by a Monte-Carlo simulation. Results of the EETM are transferred to the FKM to determine plasma source and sink terms. The FKM solves the fluid continuity equations for species densities and plasma conductivity. Electrostatic fields are also derived in the FKM by either solving Poisson's equation or assuming quasi-neutrality. The outputs of the FKM are then fed back to the EMM and EETM modules for updated computations. The whole process iterates until results reach a preset convergence criterion, or until a preset number of total iterations are finished. For

simulating an ICP system, all three modules should be used. For an rf capacitively coupled plasma (CCP), only the EETM and FKM modules are used since there is no inductively coupled power source. The Plasma Chemistry Monte Carlo Module (PCMCM) computes energy and angular dependencies of fluxes at specified surface locations by using outputs from the HPEM and is typically executed at the end of the HPEM after species densities, fluxes and electric properties have converged.

Several off-line modules of the HPEM have been developed for other specific purposes. The Monte Carlo Feature Profile Model (MCFPM) uses the results of the PCMCM to simulate micro-scale feature profile evolution and is discussed in Chapter 3.[15,23-25] The physics of the three main modules contained in the HPEM will be described in Section 2.2, followed by description the PCMCM in Section 2.3. In Section 2.4, typical results from the HPEM and PCMCM will be presented. A flow diagram of the HPEM is shown in Fig. 2.1.

2.2 Description of the Main Modules of the HPEM

2.2.1 The Electromagnetics Module

The solution for the electromagnetic fields requires knowledge of the plasma conductivity, which is obtained from the other modules. The EMM provides time-harmonic azimuthal electromagnetic fields, and it provides the static magnetic fields generated by the permanent magnets or by equivalent dc loops, that is, currents that change on time scales which are long compared to the time in which the plasma reaches quasi-equilibrium.

The EMM module calculates the spatially dependent azimuthal electric fields by solving Maxwell's equation under time harmonic conditions. Assuming azimuthal symmetry, Maxwell's equation for electric fields is reduced to

$$-\nabla.\frac{1}{\mu}\nabla E_\theta = \omega^2 \varepsilon E_\theta - i\omega J_\theta \tag{2.1}$$

where μ is the permeability, E_θ is the azimuthal electric field, ω is the frequency of the source current, ε is the permittivity, and J_θ is the total current consisting of driving and conduction currents. The conduction current J_c is calculated from $J_c = \sigma E_\theta$, where σ is the conductivity. At pressures where the electrons are sufficiently collisional, the conductivity of the plasma is

$$\sigma = \frac{q_e^2 n_e}{m_e} \frac{1}{\nu_{me} + i\omega} \tag{2.2}$$

where q_e is the unit electron charge, n_e represents electron density, m_e denotes electron mass, ν_{me} is the momentum transfer collision frequency of electrons, and ω is the driving frequency. Maxwell's equations are solved using the method of successive over relaxation (SOR). The weighting coefficients and the convergence criterion for the SOR are adjustable simulation parameters.

The static magnetic fields are solved in the radial and axial directions assuming azimuthal symmetry. Under these conditions, the magnetic field can be represented as a vector potential which has only a single component in the θ direction. The current loops, which provide source terms when solving for vector potential **A**, by differentiation, yield the static magnetic fields

$$\nabla \times A = B \quad ; \quad \nabla \times \frac{1}{\mu} \nabla \times A = j \tag{2.3}$$

where μ is the permeability and **j** is the current density of the source current loops. The vector potential is solved as a boundary value problem using SOR, with the same convergence criteria as the electric field.

A circuit module (CM) is included in the EMM which models a matchbox circuit as well as the coils. The impedance of the matchbox is matched to the coil impedance, allowing the deposited power to be maximized. The source voltage is also adjusted from iteration to iteration, allowing the power specified by the input file to be matched and maintained.

2.2.2 The Fluid Kinetics Module

In the FKM, the continuum transport equations for the gas species are solved simultaneously with the electrostatic potential to determine the spatial distribution of species densities as well as the momentum flux fields within the reactor. To solve for these plasma properties, the electron transport properties and the chemical reaction rates are obtained from the EETM. Ion and neutral transport coefficients are obtained from a database or by using Lenard-Jones parameters. To self-consistently consider the electrostatic fields, either Poisson's equation can be included, or quasi-neutrality allowing ambipolar fields can be assumed. The continuity equation for all species is

$$\frac{\partial N_i}{\partial t} = - \nabla \cdot \Gamma_i + S_i \tag{2.4}$$

which can be used to solve for the species densities where N_i, Γ_i, and S_i are the respective density, flux, and sources for species i.

The electron flux Γ_i is determined by the drift diffusion equation

$$\Gamma_i = \mu_i q_i N_i \overline{E}_s - D_i \nabla N_i \tag{2.5}$$

where μ_i is the mobility of species i, D_i is the diffusion coefficient, q_i is the species charge in units of elementary charge, and E_s is the electrostatic field. In this work, we instead used Scharfetter-Gummel discretization for fluxes.[26] In this method the flux $\vec{\varphi}_{i+\frac{1}{2}}$ between density mesh points (i, i+1) separated by Δx is given by

$$\vec{\varphi}_{i+\frac{1}{2}} = \frac{\alpha \overline{D}(n_{i+1} - n_i \exp(\alpha \Delta x))}{(1 - \exp(\alpha \Delta x))} \tag{2.6}$$

where

$$\alpha = -q\overline{\mu}\left(\frac{\Phi_{i+1} - \Phi_i}{\Delta x}\right)$$

and $\overline{D}$ and $\overline{\mu}$ are the average diffusion coefficient and mobility in the interval. The ion and neutral flux calculation can be done using the drift diffusion equation or by including the effects of momentum by the replacement of the diffusional term with terms for pressure, advection, and collisionality

$$\frac{\partial \Gamma_i}{\partial t} = -\frac{1}{m_i}\nabla\left(N_i k T_i\right) - \nabla\cdot\left(N_i \bar{v}_i \bar{v}_i\right) + \frac{q_i}{m_i} N_i\left(\bar{E}_s + \bar{v}_i \times \bar{B}\right) - \nabla\cdot\bar{\bar{v}}_i - \sum_j \frac{m_j}{m_i + m_j} N_i N_j \left(\bar{v}_i - \bar{v}_j\right)\nu_{ij} \tag{2.7}$$

where T_i is the species temperature, $\bar{v}_i$ is the species velocity given by Γ_i / N_i, and ν_{ij} is the collision frequency between species i and species j. The viscosity is included for neutrals only. Determination of the time-dependent electrostatic fields is accomplished either by solution of Poisson's equation or based on quasi-neutrality allowing an ambipolar approximation. Poisson's equation is given by

$$\nabla\cdot\left(\left(\varepsilon - \Delta t\sigma + \Delta t\sum_i q_i^2 \mu_i N_i^2\right)\nabla\varphi^{t+\Delta t}\right) = -\rho^t + \Delta t\nabla\cdot\left(\sum_i q_i D_i \nabla N_i^t - \sum q_j \Gamma_j^t\right) \tag{2.8}$$

where σ is the material conductivity and is nonzero only outside of the plasma region and e is elemental charge; q_i, μ_i, N_i, and Γ_i are the charge state, mobility, density, and flux of species i at time t, respectively; Γ_j is the flux for species j at time t; and $\phi^{t+\Delta t}$ is the electric potential at time t + Δt. Poisson's equation is calculated semi-implicitly by approximating the charge density linearly as

$$\rho^{t+\Delta t} = \rho^t + \Delta t \cdot \left.\frac{\partial \rho}{\partial t}\right|^{t+\Delta t} \tag{2.9}$$

where $\rho^{t+\Delta t}$ is the charge density at time t+Δt, and ρ^{t} is the charge density at time t. The evolution rate of the charge density $\partial\rho/\partial t$ is determined by the divergence of the total current density j:

$$\frac{\partial \rho}{\partial t} = -\nabla \cdot j + S, \tag{2.10}$$

where S is the source function of charges. In the plasma region, $j = q_i(-D_i \nabla n_i + q_i \mu_i(-\nabla\varphi))$ for electrons and $\mathbf{j} = q\Gamma$ for ions. In materials, $j = \sigma(-\nabla\varphi)$ where σ is the material conductivity. By making the potential fully implicit in this scheme while using explicit terms for the assumedly more slowly varying species properties such as density and temperature, the time step used in the SOR solution can be lengthened beyond the dielectric relaxation time and greatly accelerate solution over the fully explicit formulation.

The second option is to compute electrostatic fields using a quasi-neutrality approximation over the entire plasma region. Under such an assumption the electron density can be set equal to the total ion density at all locations. To maintain this charge neutrality requires that

$$-\nabla \cdot \Gamma_e + S_e = \sum_i q_i(-\nabla \cdot \Gamma_i + S_i) \tag{2.11}$$

or

$$\nabla \cdot (\mu_e n_e \nabla\varphi + D_e \nabla n_e) + S_e = \sum_i q_i(\nabla \cdot (-\mu_i n_i \nabla\varphi + D_i \nabla n_i) + S_i) \tag{2.12}$$

where S_e and S_i represent electron and ion source functions, respectively, due to both internal and external sources such as electron beams. The flux terms are replaced by their drift diffusion approximations and the terms are rearranged to get

$$\sum_i q_i \nabla \cdot \left(q_i n_i \mu_i \nabla \varphi - D_i \nabla n_i \right) = \sum_i q_i S_i \tag{2.13}$$

where the summations are taken over all charged species including both electrons and ions. By reducing the system to a steady-state solution, the dielectric relaxation time is removed as a limit allowing much larger time steps to be taken, which are limited only by the Courant limit.

A semi analytic sheath model (SM) has also been integrated with the FKM to represent the fields and fluxes at gas-solid boundaries under conditions where the actual sheath thickness is less than the mesh spacing. A multi species form of Riley's unified sheath model is used to relate the sheath charge *Q* and boundary conditions to the potential drop.[27] This potential drop across the sheath produced by the semi analytic sheath model is then applied as a jump condition at plasma wall boundaries in solving Poisson's equation for the entire reactor.

2.2.3 The Electron Energy Transport Module

In the Electron Energy Transport Module, the power deposition into the electrons, as well as the electron impact sources, is modeled and the electron transport properties are computed. These can be solved in two different ways in the HPEM. The first method is to solve the 2-D electron energy equation. Electron transport properties as a function of temperature are obtained by solving the 0-D Boltzmann equation. The second method is to run a Monte Carlo simulation,

in which electron pseudo-particles are moved in the computed fields and have collisions with the other plasma species. The trajectories are integrated over a period of time and the statistics are collected to generate the electron energy distribution functions (EEDs), which are then used to calculate the rate coefficients.

2.2.3.1 The Electron Energy Equation Method

The Electron Energy Equation Method first numerically solves the 0-D Boltzmann equation for a range of values of electric field divided by total gas density (E/N) in order to create a table of values, which correlate E/N with an EED. The 0-D Boltzmann equation is expressed as

$$\frac{\partial f_e}{\partial t} - \frac{eE}{m_e} \cdot \nabla_v f_e = \left(\frac{\delta f_e}{\delta t} \right)_{collision}, \tag{2.14}$$

where $f_e = f_e(t, \mathbf{r}, \mathbf{v})$ is the electron distribution function, ∇_v is the velocity gradient, m_e is the electron mass, and $\left(\frac{\delta f_e}{\delta t} \right)_{collision}$ represents the effect of collisions. The resulting values are then used as a lookup table, which yields electron mobility, thermal conductivity, energy-loss rate due to collisions and electron impact rate coefficients as a function of electron temperature. T_e is defined as 3/2 $<\varepsilon>$, where $<\varepsilon>$ is the average energy computed from the EEDs.

With the EEDs known as a function of temperature, the steady state electron energy equation is solved as follows:

$$\nabla\kappa\nabla T_e + \nabla \cdot (\Gamma_e T_e) = P_h - P_l \,, \tag{2.15}$$

where κ is the thermal conductivity, T_e is the electron temperature, Γ_e is the electron flux, P_h is the electron heating due to deposition, and P_l is the power loss due to inelastic collisions. The electron flux Γ is computed in the FKM, and the power deposition rate is computed from the time-averaged value of j.E, where $j = \sigma E - qD\nabla n_e$. The electric field is both the inductive field computed in the EMM and the capacitively coupled field computed in the FKM. The above equation is discretized and solved by SOR, with the transport coefficients updated based on the local electron temperature.

2.2.3.2 The Electron Monte Carlo Method

The Monte Carlo method is a fully kinetic treatment, which resolves the gyro motion of electrons in magnetic fields using a semi-implicit technique. Noncollisional heating is kinetically resolved by producing electron currents, which are used to correct the assumption of collisional power deposition in the EMM.

The Electron Monte Carlo Simulation (EMCS) tracks the trajectory of electron pseudo-particles by moving them in the computed electric and magnetic fields as a function of time. A group of electrons is initialized from a Maxwellian distribution and randomly distributed within the rf period, with starting locations randomly determined within the reactor volume weighted by the electron density computed in the FKM. The electron energy range is divided into discretized energy bins for collision determination and this binning also helps in collecting statistics. The

collision frequency ν_i within any energy bin is computed by summing all possible collision within the energy range

$$\nu_i = \left(\frac{2\varepsilon_i}{m_e} \right)^{\frac{1}{2}} \sum_{j,k} \sigma_{ijk} N_j \tag{2.16}$$

where ε_i is the average energy within the bin, σ_{ijk} is the cross section at energy i, for species j and collision process k, and N_j is the number density of species j. The time between the collisions is randomly determined using the maximum collision frequency for all energy bins $\Delta t = \frac{-1}{\upsilon} \ln(r)$, r = (0,1). At the time of a collision, the reaction that occurs is chosen randomly from all the possible reactions for that energy bin. A null collision cross section makes up the difference between the actual collision frequency and the maximum collision frequency at any given spatial location. In this work electron-electron collisions are not considered. The velocity of the electrons is adjusted based on the type of collision it undergoes. If the collision is null then the electron's trajectory is unaltered. Particles are integrated using the Lorentz equation.

$$\frac{d\bar{v}}{dt} = \frac{q_e}{m_e} \left(\bar{E} + \bar{v} \times \bar{B} \right) \tag{2.17}$$

and

$$\frac{d\bar{r}}{dt} = \bar{v} \tag{2.18}$$

where $\bar{v}$, $\overline{E}$, and $\overline{B}$ are the electron velocity, local electric field, and magnetic field respectively. Eqs. (2.17) and (2.18) are updated using a second-order predictor corrector scheme. Electric fields are both the inductive fields computed in the EMM and the time-dependent static fields computed in the FKM. Time steps are chosen to be less than both 1% of the rf period and 1% of the cyclotron frequency, and small enough that the particles do not cross more than one-half computational cell in one time step. Several hundred to a few thousand particles are integrated in time for many rf cycles, typically greater than 100 rf cycles.

The statistics for computing the electron energy distributions (EEDs) are updated every time an electron is moved in the mesh, which is at every time step. These statistics are collected into an array for energy i and location l:

$$F_{il} = \sum_j w_j \delta((\varepsilon_i \pm 1/2\ \Delta\varepsilon_i) - \varepsilon_j)\delta(\vec{r}_l \pm \Delta\vec{r}) - \vec{r}_j) \tag{2.19}$$

where the summation is over particles, w_j is the weighting of the particle, ε_i is the energy and r_k is the bin location. The weighting w_j is a product of three factors: the relative number of electrons each pseudo-particle represents, the time step used to advance the trajectory, and a spatial weighting obtained using the method of finite-sized particles (FSP). At the end of the EMCS, the electron temperature, collision frequency and electron-impact rate coefficients are computed as a function of position from the EEDs. The EEDs f_{ik} are obtained from the raw statistics F_{ik} by requiring normalization of each spatial location.

$$\sum_i F_{ik}\Delta\varepsilon_i = \sum_i f_{ik}\varepsilon_i^{0.5}\Delta\varepsilon_i = 1 \tag{2.20}$$

The electron temperature is defined by convention to be 2/3 <ε>. The electron impact rate coefficient (k_m) for electron impact process m and location l is computed as

$$k_{ml} = \int_0^\infty \left(\frac{2\varepsilon}{m_e}\right)^{\frac{1}{2}} \sigma_m(\varepsilon) f_l(\varepsilon) \varepsilon^{\frac{1}{2}} d\varepsilon = \sum_i \left(\frac{2\varepsilon_i}{m_e}\right)^{\frac{1}{2}} \sigma_{mi} f_{il}(\varepsilon) \varepsilon_i^{\frac{1}{2}} \Delta\varepsilon \tag{2.21}$$

$$k_{ml} = \frac{\sum_i F_{il} \upsilon_i \sigma_{mi} \Delta\varepsilon_i}{\sum_i F_{il} \Delta\varepsilon_i} \tag{2.22}$$

2.2.4 The Plasma Chemistry Monte Carlo Module

To obtain the energy and angular distributions of reactive species to the substrate, the PCMCM was developed for the HPEM. The PCMCM calculates the trajectories of plasma species in the gas phase and their collisions with surfaces. This module was originally a postprocessor to the HPEM. It used volumetric sources of plasma species, time-dependent electric fields, and sheath properties exported from the HPEM to obtain the angular and energy distributions of the fluxes using Monte Carlo techniques.[6] The PCMCM functions in a similar manner but also accounts for nonthermal, or in-flight fluxes, resulting from sputter sources in addition to the volumetric sources. Sputtered atoms and neutralized ions which are reflected from the target have kinetic energies of several eV. These species are not initially in thermal equilibrium with the buffer gas, which has a temperature of ≤0.3 eV. Under certain process conditions, these energetic particles may not thermalize prior to reaching the wafer. The trajectories and energies of these nonequilibrium particles are already tracked by the sputter

algorithms in the FKM. Statistics on the energy and angular distributions of the particles as they strike selected surfaces are collected and passed to the PCMCM.

Based on these quantities, a rate of generation of species *i* as a function of position, $G_i(\vec{r})$ ($cm^{-3}s^{-1}$), is computed. This generation term accounts for all sources of species *i* on the right-hand side of reactions in the mechanism. The rate $G_i(\vec{r})$ also includes source functions on surfaces due to, for example, sputtering. In a similar fashion, a consumption rate $C_i(\vec{r})$ ($cm^{-3}s^{-1}$) is computed based on all reactions containing species *i* on the left-hand side of reactions in the mechanism. A local elastic collision frequency with each species is also computed. These elastic frequencies are added to the local consumption frequency $C_i(\vec{r})\Delta V(\vec{r})$, where $\Delta V(\vec{r})$ is the volume of the computational cell at location $\vec{r}$ to yield a total interaction frequency $\nu_T(\vec{r})$. Null collision techniques are used at each spatial location to provide a reactor wide collision frequency ν_i for each species *i*.

Pseudoparticles of species *i* are launched from each computational cell at a time randomly chosen in the rf cycle with a weighting (or total number) proportional to $G_i(\vec{r})\Delta V(\vec{r})$. The velocity is randomly chosen from a Maxwell-Boltzmann distribution having a local temperature $T_i(\vec{r})$ for volumetric sources where the spatially dependent temperature for each species is computed by HPEM. The trajectories of the pseudoparticles are integrated for the time

$$\Delta t = -\frac{1}{\nu_i}\ln(r), \tag{2.23}$$

where Δt is the time step for movement of the pseudoparticle and r is a random number distributed on (0,1). For ions, acceleration by the local electric field is accounted for. The time step used to increment the trajectory is limited by the time required to cross a specified fraction of the cell (typically 0.2). For ions, additional constraints are applied including a specified fraction of the rf cycle (typically 0.05), or the time to cross a specified fraction of the sheath width (typically 0.01).

At the end of the time step, Monte Carlo techniques are use to determine if the collision is real or null. If real, another random number is used to determine if the collision is elastic or consuming. If consuming, the particle is removed from the simulation. If elastic, the collision partner is identified using another random number and the velocity of the pseudoparticle is changed appropriately using standard elastic collision techniques. The one exception is for charge exchange collisions which are separately accounted for in the sum of collision frequencies. If an ion undergoes a charge exchange collision, its identity is changed to the neutral counterpart and the trajectory is retained. The trajectories are advanced until the pseudoparticles reach the vicinity of a surface. If the surface is chosen as one for which statistics on incident species are desired, ions are then integrated through the sheath, a computationally expensive process. For surfaces not selected, the particles are removed from the simulation. A similar process is followed for the neutrals, except for integration through the sheath.

2.3. Typical Results from the HPEM

Typical results from HPEM include 2-D distributions of fields, power deposition, source functions, species densities, species fluxes and 1-D distribution of fluxes at the wafer. Results from the PCMCM include EADS at different specified locations. In this section HPEM and PCMCM results for an example case is presented. The cylindrical ICP reactor used for this study is shown in Fig. 2.2. Inductive power is supplied through a three-turn coil, 16 cm in diameter. The coil sits on a 2 cm thick quartz window, which is 23 cm in diameter. The wafer is on a substrate 7 cm below the quartz window and which can be independently biased. For the base case, the CHF_3 flow rate is 40 sccm and the pressure is 6 mTorr. The coil source current is at 13.56 MHz and delivers an inductive power of 1400 W. The rf bias was varied to control the dc bias on the wafer. All the plasma properties for this case are presented for a dc bias of -100 V.

Power deposition is shown in Fig. 2.2(b). In this system the ionization produced by the inductive coils dominates over the ionization induced by the capacitive bias (which is typical for most ICP systems). As a result the power deposition is restricted to the top of the reactor to within the skin depth of the electromagnetic field, which is a few cm. Large power depositions highly dissociate the gas and populate the smaller molecules such as CF_2, CF, CF_3, H and F. The CF_2^+ density and source functions are shown in Fig. 2.3. As diffusive transport dominates at low pressures, CF_2^+densities are larger near the center of the reactor. The CF_2^+ source functions is reflective of the density. For the same reasons the CF_2 density, which is shown in Fig. 2.4, is large at the center of the reactor. CF_2 density is also high near the feed nozzle as it is a product of the dissociation of CHF_3, which peaks near the nozzle. Fluxes of the prominent ions and

neutrals on the wafer as a function of the radius are shown in Fig. 2.5. The prominent ions are CF_2^+, CF_3^+ and F^+. The prominent neutrals are F, H, CF_2 and CF.

The EADs of CF_3^+, F^+ and CF_2 at the center of the wafer obtained from the PCMCM are shown in Fig. 2.6. The rf bias on the wafer produces a negative dc component on the substrate. This results in the sheath voltage drop peaking above the wafer, contributing to the energetic ion bombardment of the wafer surface. As a result, the ions are directed towards the wafer with average energies ≈ 200 eV. This also leads to a fairly narrow angular distribution of the ion fluxes and creates an anisotropic ion flux. In contrast, the neutral flux has energies of <1 eV and a broad angular distribution (isotropic).

2.4 Figures

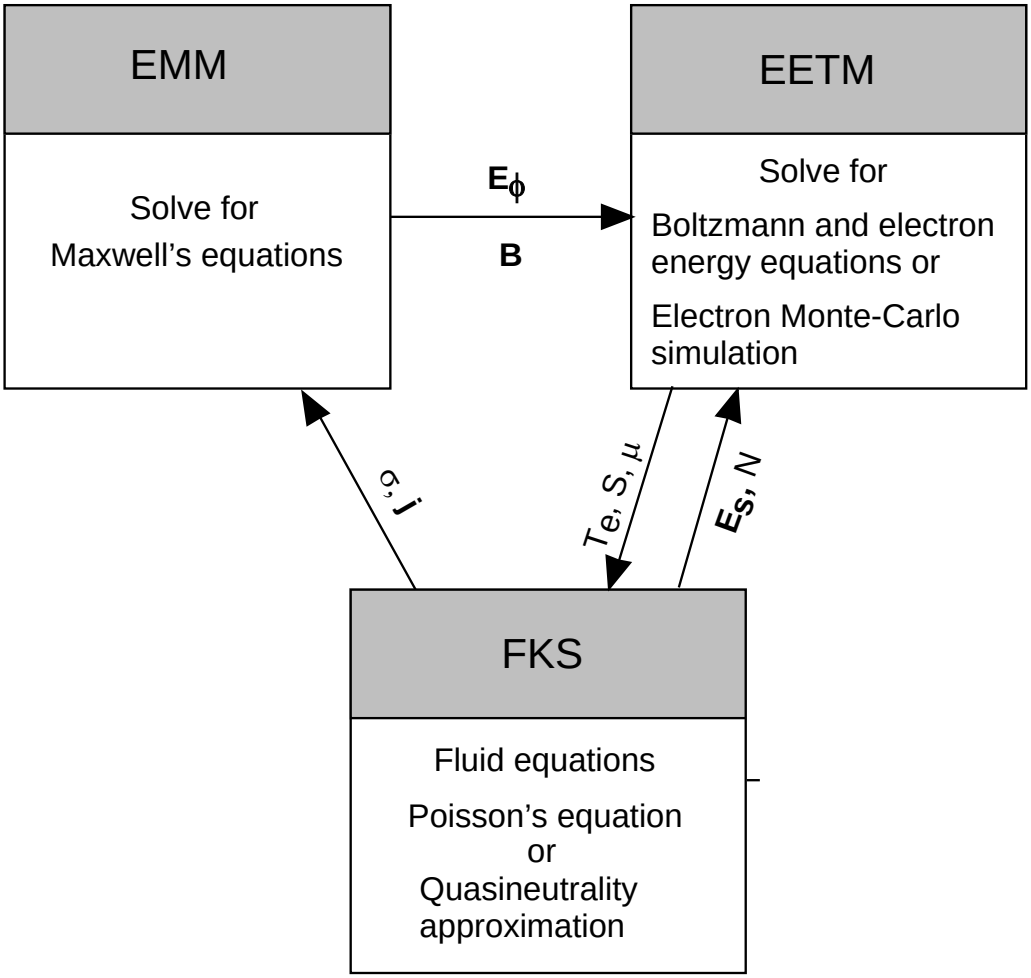

Fig. 2.1. Schematic of the modular HPEM

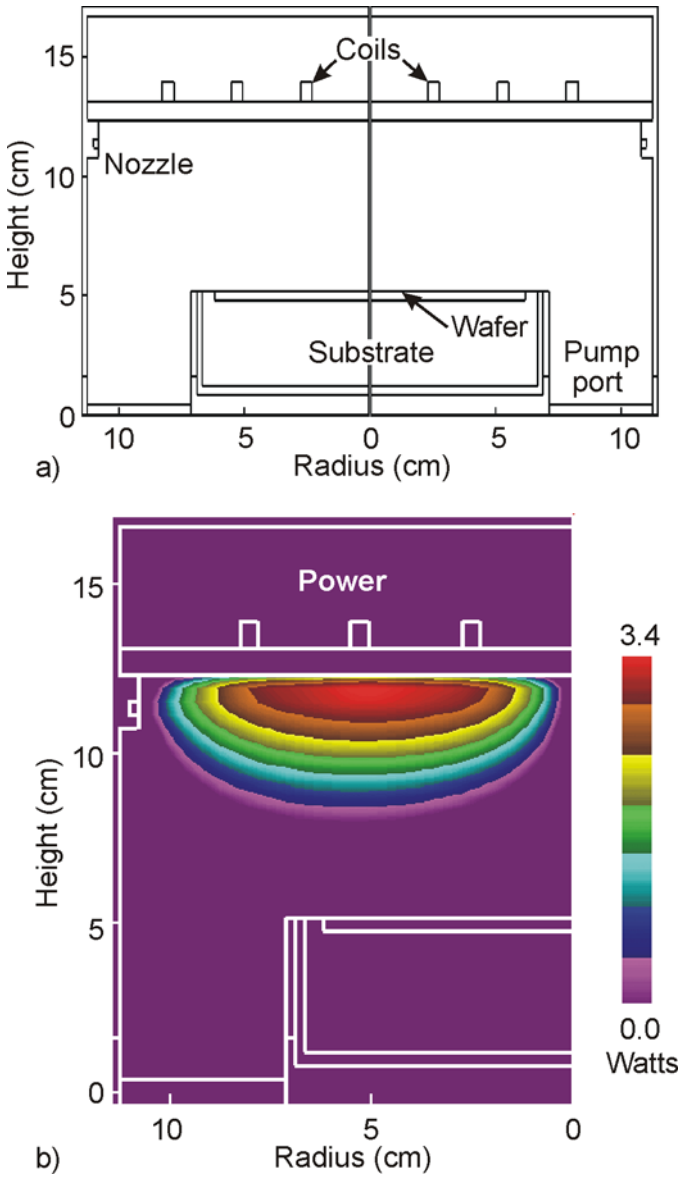

Fig. 2.2. (a) Schematic of an ICP reactor . (b) Power deposition for process conditions: CHF_3, 6 mTorr, 40 sccm gas flow rate, 1400 W ICP power, -100 V dc bias.

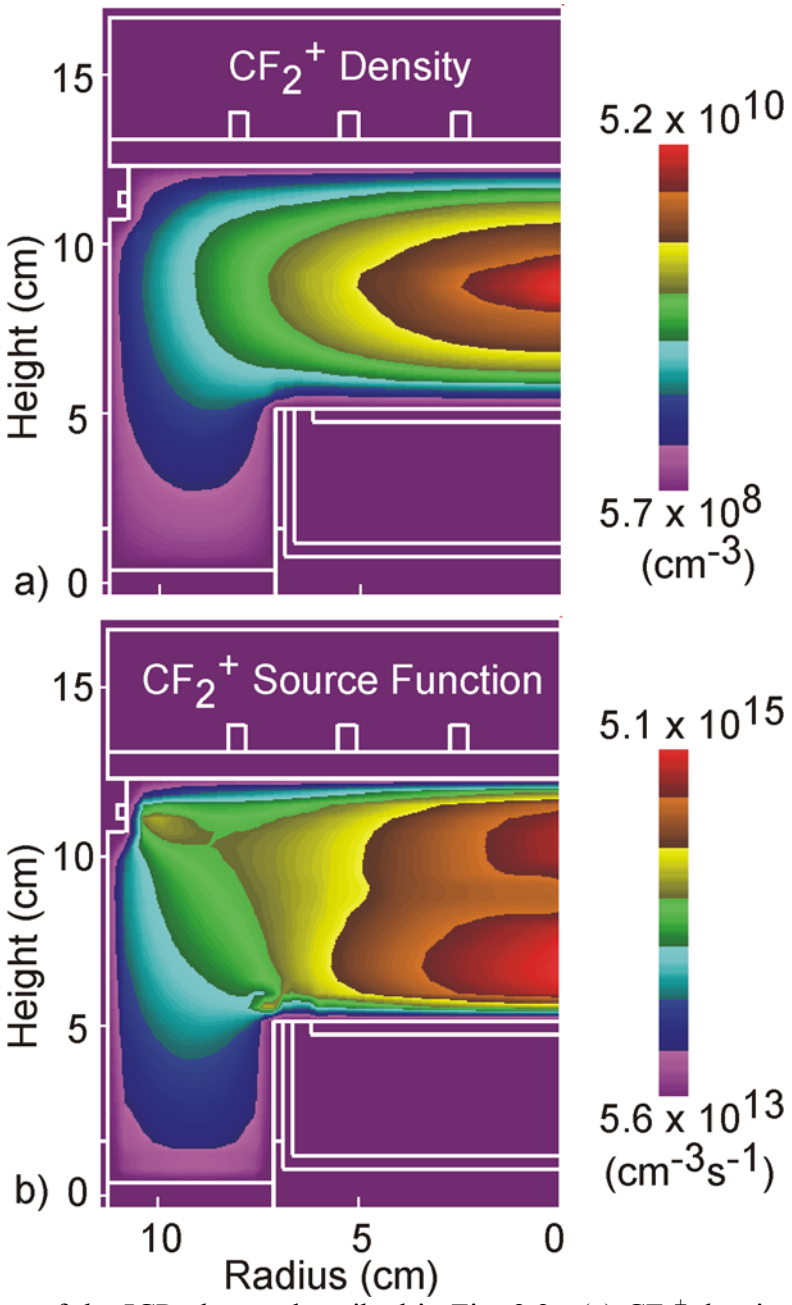

Fig. 2.3. Properties of the ICP plasma described in Fig. 2.2. (a) CF_2^+ density. (b) CF_2^+ source function.

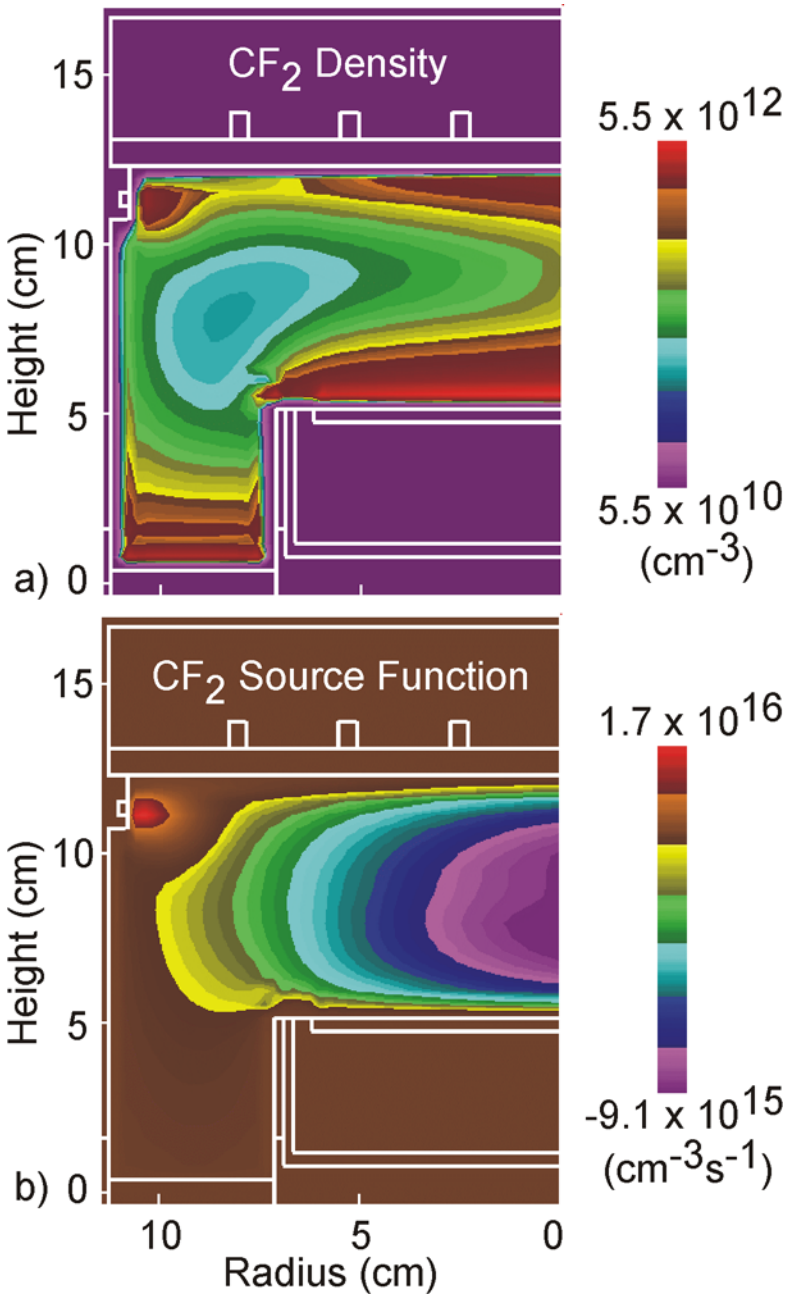

Fig. 2.4. Properties of the ICP plasma described in Fig. 2.2. (a) CF_2 density. (b) CF_2 source function.

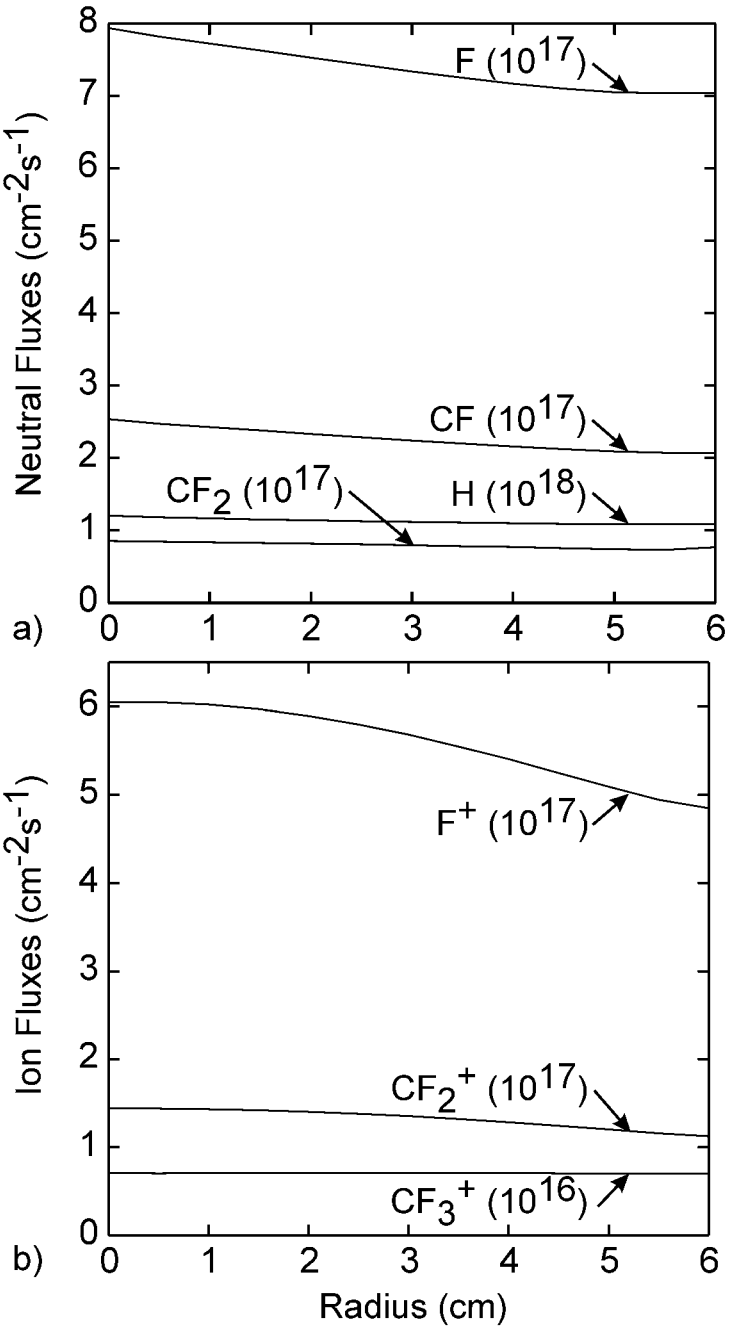

Fig. 2.5. Fluxes to the surface as a function of radius for the ICP plasma described in Fig. 2.2. (a) Fluxes of CF_2, CF, H and F. (b) Fluxes of F^+, CF_2^+ and CF_3^+.

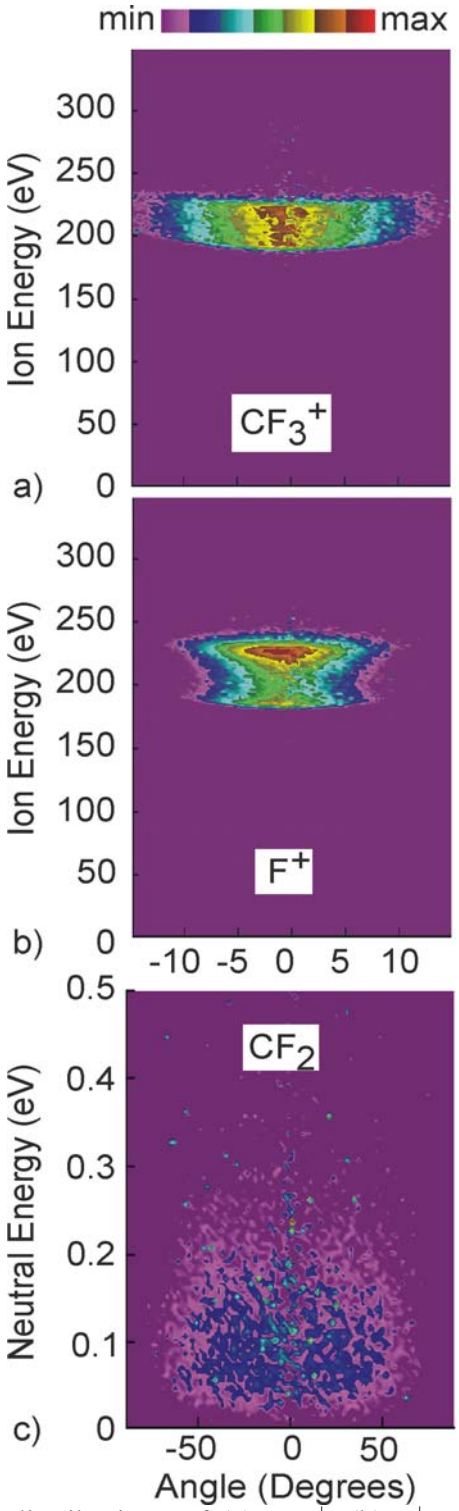

Fig. 2.6. Energy and angular distributions of (a) CF_3^+, (b) F^+ and (c) CF_2 at the center of the wafer for the ICP described in Fig. 2.2.

2.5. References

[1] T. J. Sommerer and M. J. Kushner, J. Appl. Phys. **71,** 1654 (1992).

[2] P. L. G. Ventzek, R. J. Hoekstra, T. J. Sommerer, and M. J. Kushner, Appl. Phys. Lett. **63,** 605 (1993).

[3] P. L. G. Ventzek, R. J. Hoekstra, T. J. Sommerer, and M. J. Kushner, J. Vac. Sci. Technol. B **12,** 461 (1994).

[4] P. L. G. Ventzek, M. J. Grapperhaus, and M. J. Kushner, J. Vac. Sci. Technol. B **12,** 3118 (1994).

[5] F. Y. Huang and M. J. Kushner, J. Appl. Phys. **78,** 5909 (1995).

[6] R. J. Hoekstra and M. J. Kushner, J. Appl. Phys. **79,** 2275 (1996).

[7] W. Z. Collison and M. J. Kushner, Appl. Phys. Lett. **68,** 903 (1996).

[8] H. H. Hwang and M. J. Kushner, Appl. Phys. Lett. **68,** 3716 (1996).

[9] M. J. Grapperhaus and M. J. Kushner, J. Appl. Phys. **81,** 569 (1997).

[10] S. Rauf and M. J. Kushner, J. Appl. Phys. **81,** 5966 (1997).

[11] M. J. Kushner, J. Appl. Phys. **82,** 5312 (1997).

[12] M. J. Grapperhaus, Z. Krivokapic, and M. J. Kushner, J. Appl. Phys. **83,** 35 (1998).

[13] S. Rauf and M. J. Kushner, IEEE Trans. Semiconductor. Manufact. **11,** 486 (1998).

[14] S. Rauf and M. J. Kushner, J. Appl. Phys. **83,** 5087 (1998).

[15] R. J. Hoekstra and M. J. Kushner, J. Vac. Sci. Technol. B **16,** 2102 (1998).

[16] S. Rauf and M. J. Kushner, J. Vac. Sci. Technol. A **17,** 704 (1999).

[17] D. Zhang and M. J. Kushner, J. Appl. Phys. **87,** 1060 (2000).

[18] X. Xu, S. Rauf, and M. J. Kushner, J. Vac. Sci. Technol. A **18,** 213 (2000).

[19] D. Zhang and M. J. Kushner, J. Vac. Sci. Technol. A **19,** 524 (2001).

[20] R. L. Kinder and M. J. Kushner, J. Vac. Sci. Technol. A **19,** 76 (2001).

[21] R. L. Kinder and M. J. Kushner, J. Appl. Phys. **90,** 3699 (2001).

[22] A. Sankaran and M. J. Kushner, J. Appl. Phys. (2002).

[23] R. J. Hoekstra, M. J. Grapperhaus, and M. J. Kushner, J. Vac. Sci. Technol. A **15,** 1913 (1997).

[24] A. Sankaran and M. J. Kushner, in preparation for J. Vac. Sci. Technol. A.

[25] J. Lu and M. J. Kushner, J. Vac. Sci. Technol. A **19,** 2652 (2001).

[26] D. L. Scharfetter and H. K. Gummel, IEEE Transactions on Electronic Devices **ED-16,** 64 (1969).

[27] M. E. Riley, *Sandia Report SAND 95-0775* (UC-401, 1995).

3. MONTE CARLO FEATURE PROFILE MODEL

3.1. Introduction

The Monte Carlo Feature Profile Model (MCFPM) has been developed to allow self-consistent determination of topographical feature evolution for semiconductor processing in plasma reactors.[1-3] To date, the model has focused on etching, stripping and ionized metal physical vapor deposition (IMPVD), but has the capability to include other processes such as plasma enhanced chemical vapor deposition (PECVD) and physical vapor deposition (PVD). The MCFPM is integrated with the Hybrid Plasma Equipment Model (HPEM) through the use of energy and angular distributions (EADs) produced by the Plasma Chemistry Monte Carlo Module (PCMCM) in the HPEM for arbitrary radial location on the substrate.

The MCFPM is described in Section 3.2. The computation mesh used in the MCFPM and the algorithms for particle motion are presented in Section 3.2.1. The physics of the interaction of energetic particles with the surface is captured in Section 3.2.2. The surface diffusion algorithm used for deposition process is described in Section 3.2.3. The modifications made to the MCFPM in this work to address porous two-phase substrates are discussed in Section 3.2.4. The surface reaction mechanisms developed in this work for fluorocarbon etching of SiO_2/Si substrates and oxygen etching of organic polymer are explained in Section 3.3. Finally, sample results for integrated modeling (etch, strip and fill) for nonporous and porous SiO_2 films obtained using the MCFPM are presented in Section 3.4.

3.2. Description of the Model

The MCFPM is a Monte Carlo model, which simulates the use of statistically weighted pseudoparticles representative of the fluxes of active species to the feature surface. Through

ballistic transport and interaction with the mesh delineated surface, time integrated surface evolution is obtained.

3.2.1. Computational Mesh and Particle Motion

The MCFPM resolves wafer features (masks, photoresists, semiconductors) on the submicron scale utilizing a rectilinear mesh. The mesh spacing is typically $\approx 1 \times 1$ nm , which is $\approx 4 \times 4$ or fewer atoms. Each cell is assigned a material identity (e.g., poly-Si, photoresist, SiO_2, plasma) which may change during the simulation. Solid species, including adsorbates or passivation, are represented by the identity of the computational cell. Gas phase species (i.e., radicals and ions) are represented by computational pseudoparticles. Pseudo-particles are launched towards the surface from random locations above the trench with energies and angles sampled from the EADs obtained from the PCMCM. The EADs produced by the PCMCM are flux weighted probability distribution functions (F) which must be converted and normalized as cumulative distribution functions (f):

$$f(\varepsilon , \theta, r) = \frac{F(\varepsilon , \theta, r)}{\int \int F((\varepsilon , \theta)\, d\varepsilon\, d\theta} \tag{3.1}$$

The pseudoparticles are launched with a frequency computed from the total flux of radicals or ions incident onto the substrate so that each pseudoparticle represents a fraction of the number of atoms in a mesh cell based on the gas-to-material weighting ratio:

$$W_g = \frac{1}{\gamma} W_S \tag{3.2}$$

where W_g is the gas particle weighting, W_s is the mesh or surface cell weighting, and γ is the gas-to-surface ratio, which was set to 1 for this work. The pseudoparticle trajectories are advanced in time where the calculation of position and velocity are separated, allowing solution of two linear equations:

$$v_i = v_{i-1} + \frac{qE}{m} \Delta t \text{ and } x_i = x_{i-1} + v_i \Delta t \tag{3.3}$$

where v and x represent the velocity and position of the particle, and the subscripts indicate the former or current velocity and position; q and m indicate the charge and mass of the particle, respectively; and Δt indicates the time-step taken by the particle. This method is used because under the majority of cases the effects of charging are ignored and the electric field E is set to zero, allowing solution of the second linear equation only. Particle motion can be sequenced in the following steps:

1. At any instant of the particle's motion, the time step for its current move is determined by the time required to move the minimum distance to a surface.
2. Based on this time step and the solution to Eq. (3.3), the new velocity and position of the particle is determined. At this point the time step is reset so that the next move can be performed.

3. If the distance to a surface is still greater than one mesh cell, this new distance is used to calculate the time step for the next move and step 2 is repeated. The particle is thus moved until a material containing cell is occluded.
4. Only for $\gamma > 1$, if the particle is within one mesh cell of a surface, the particle is moved back to its previous position, the previous time-step is halved, and the particle is moved again. This process is iterated until the particle moves within a fraction of the material containing cell, generally $0.05 \times$ (Cell Width).

The effects of surface charging on the profile evolution can be addressed. Electron trajectories can be simulated as low-temperature isotropic fluxes which impinge upon the feature during the low-potential swing of the sheath. This macroscopically balances the current due to the ions. To resolve the electric fields due to the charged surfaces of the feature, an iterative explicit solution of Poisson's equation is determined utilizing successive overrelaxation (SOR):

$$\nabla \cdot \varepsilon \nabla \varphi^{t+\Delta t} = -\rho^{t} \tag{3.4}$$

SOR is used to accelerate solution by multiplying the calculated $\Delta\phi$ by an overrelaxation factor greater than one. Neumann boundary conditions are used at the top and bottom of the feature by assuming that the electric field above the feature matches the sheath field from the FKS and that the electric field below the feature is approximately zero. The left and right boundaries are assumed to follow a periodic Dirichlet condition.

3.2.2 Energetic Particle Interaction

The specifics of the interaction of energetic particles with surface species are determined by the EADs. The source of energetic particles is ions accelerated through the sheath, with energies of up to 100s eV and angular spreads <5-10° from the vertical. We have assumed that ions neutralize upon interaction with the surface and so do not distinguish between energetic ions and energetic neutrals. Energetic particles can either specularly or diffusively reflect from surfaces, with an energy loss which is larger for diffusive scattering and small for specular.

Following the work of Donnelly *et al*. and Graves *et al*., our generalized reaction probability for a particle of energy E incident onto a surface at an angle θ from the local vertical of the surface is [4,5]

$$p(\theta) = p_0 \left[\frac{E^n - E_{th}^n}{E_r^n - E_{th}^n} \right] f(\theta) \tag{3.5}$$

where E_{th} is the threshold energy of the process, E_r is a reference energy, p_0 is the probability for normal incidence at E_r and $f(\theta)$ is the relative probability at angle of incidence θ. Based on the work of Graves *et al*. $f(\theta)$ is an empirical function typical of chemically enhanced sputtering with a maximum value near $\theta = 60°$.[5]

The reflection of particles from surfaces was given both specular and diffusive character. To account for surface roughness on spatial scales not resolved by our model, we specified that a fraction $f_d = 0.25$ was diffusively scattered. The energy of specularly reflected particle was scaled such that forward scattered particles retain the majority of their energy. The specularly reflected particle energy for incident energy E_I is

$$E_s(\theta) = E_I \left(\frac{E_I - E_c}{E_{ts} - E_c} \right) \left(\frac{\theta - \theta_c}{90^\circ - \theta_c} \right) \tag{3.6}$$

for $\theta > \theta_c$, $E_c < E_I < E_{ts}$. Particles having $\theta < \theta_c$ or $E_I < E_c$ are said to diffusively scatter. Particles having $E_I > E_{ts}$ are said to retain all of their energy subject to the angular correction. We used E_{ts} = 100 eV, E_c = 0 eV and θ_c = 60°. The final reflected energy of the particle is a weighted sum of the specularly reflected energy and diffusively reflected energy.

The construction of the probability arrays for interaction of gas phase with surface cells is problematic due to the energy dependence of the reaction probability and the requirement that probabilities add to unity. This process is facilitated by use of a null process for all combinations of incident gas phase species and surface species. The null process is reflection without reaction. As the probability of energy dependent process changes, the null portion of the probability array is rescaled to ensure that the sum of probabilities is unity. Should an etch yield exceed unity, the null reaction is eliminated and the array rescaled.

3.2.3 Surface Diffusion

The MCFPM is also capable of addressing surface diffusion during deposition of materials.[3] We only used this option for diffusion of metal atoms on metal underlayers. All depositing metal atoms are first physisorbed, which are treated differently from the underlying material even if they have the same composition. The physisorbed atoms diffuse on the surface before they are chemisorbed onto the underlying material. An adsorbed cell can diffuse into any unoccupied adjacent cell in the mesh. The probability that an adsorbed cell i moves to another

cell j is dependent on their potential energy values, which are based on effective Morse potentials.

$$\Phi_{ij} = \Phi_0 \left\{ \exp\left(-2 \frac{r_{ij} - r_0}{a_0} \right) - 2 \exp\left(- \frac{r_{ij} - r_0}{a_0} \right) \right\} \tag{3.7}$$

where r_{ij} is the distance between the center of the cells. Φ_0 was set to 0.3 eV based on the predictions by Lu *et al*.[3] r_0 and a_0 were set to 1.6 nm and 5 nm based on mesh scale lengths as opposed to atomic lengths. The probability of diffusion to all possible locations is summed and normalized. The final diffusion path is then chosen randomly. Based on the chosen value of the activation energy for diffusion from i to j (E_{ij}), the adsorbed cell either chemisorbs or diffuses. The frequency of such trials is governed by the jump frequency ν,

$$\nu = - \nu_{ij} \ln(r) \tag{3.8}$$

where

$$\nu_{ij} = \nu_0 \exp\left(- \frac{E_{ij}}{k_b T_s} \right) \tag{3.9}$$

and

$$\nu_0 = 2k_b T_s/h \tag{3.10}$$

where h is the Planck's constant, k_b is the Boltzman's constant and T_s is the substrate temperature. At 393 K, $\nu_0 = 1.6 \times 10^{12}$ s^{-1}. Based on the specified threshold jump frequency (ν_t), the cell chemisorbs if $\nu<\nu_t$. ν_t was chosen to be 10^8 s^{-1} based on earlier studies.[3]

3.2.4 Two Phase Porous Substrates

PS is modeled as being stoichiometric SiO_2 with vacuum pores. The pore radii and locations are randomly chosen and distributed in the numerical mesh used by the MCFPM with a Gaussian distribution of radii having probability

$$p(r) \sim \exp(-((r-r_0) / \Delta r)^2) \tag{3.11}$$

where r is the radius of the incorporated pore, r_0 is the average pore radius and Δr is the standard deviation. Algorithms were developed to include the capability of creating both closed and interconnected pore networks.

The interconnectivity of the network is the fraction of pores that are connected to another pore. PS having an interconnectivity of 0% consists of isolated pores. In PS having an interconnectivity of 100%, every pore is connected to at least one other pore in a low fractal dimension manner. To create an interconnected structure, the following procedure is used. Based on the specified fractional interconnectivity, a pore is randomly chosen to be isolated or connected. Pore locations and radii are then chosen randomly. As pores are created in the mesh, the numerical cells which are on the inside of pores are tracked. Pores which overlap result in

some fraction of the mesh cells being owned by both pores. For an isolated pore, mesh cells can be owned by only a single pore. For an interconnected pore, at most two pores can own any given mesh cell. If a randomly placed pore overlaps a cell which is already owned by the maximum allowed pores, the placement is disallowed. The end result is that the pores are chain-like with a low fractal dimension. Higher fractal dimensions can be obtained by allowing ownership by additional pores. The pore placement process is repeated until the desired porosity is achieved.

As etching proceeds, computationally solid mesh cells may become isolated from the remainder of the mesh. For nonporous single-phase materials, such cells are dropped or moved vertically to rejoin a solid surface. This is a more difficult challenge when modeling PS, in that the unopened vacuum pores must be differentiated from the bulk. During pore creation, the maximum pore dimension in each column of the mesh is stored. As etch evolves, a solid mesh cell is treated as being isolated if its vertical distance to the closest surface is greater than the maximum pore size in that column. At such time, the isolated solid mesh cell is transitioned to a surface.

3.3 Surface Reaction Mechanisms

Surface reaction mechanisms, in general, are an intrinsic property of the gas phase reactant species (incident on the surface) and the surface species. As such, reaction mechanisms should be independent of the process conditions, such as the plasma source or the gas chemistry. The process conditions may determine the energies and magnitudes of the incident reactant fluxes, however the reaction mechanism should not change. We have attempted to address this issue by developing a generalized reaction mechanism applicable to etching of SiO_2 in at least

three different fluorocarbon chemistries initially consisting of the feedstock gases of C_2F_6, CHF_3 or C_4F_8. A surface reaction mechanism for etching of fluorocarbon polymer in O_2 plasma has been developed and applied to the stripping of residual fluorocarbon from etched PS films. As a part of integrated modeling, Cu IMPVD onto the stripped vias was investigated as a surrogate to barrier layer. The reaction mechanism developed by Lu *et al*. has been adopted and applied towards this.[3]

3.3.1 Fluorocarbon Plasma Etching of SiO_2 and Si

The reaction mechanism for etching of SiO_2 and Si in fluorocarbon plasmas is schematically shown in Fig. 3.1 and is listed in Table 3.1. The fluxes to the substrate consist of polymerizing neutral radicals, energetic ionic species and neutral etching radicals. The polymerizing radicals are CF, CF_2, C_2F_3, and C_2F_4. The reaction proceeds by the formation of a steady state polymer layer on top of the substrate.[6,7] The initial layer of polymer on SiO_2 forms a $SiO_2C_xF_y$ complex, which is the precursor to etching. Further polymer growth is problematic as polymerizing radicals are thought to have little probability of sticking to the $SiO_2C_xF_y$ complex. In this regard it has been proposed that low energy ion bombardment promotes the formation of polymer by activating surface sites.[8-10] For example, Goto *et al*. investigated polymer growth using a CF_2 beam in an Ar microwave plasma with Ar^+ energies in the low 10's eV.[8] They found that polymer deposition was significantly higher in the presence of Ar^+ than when only a CF_2 beam was used. Similarly, Booth *et al*. observed a high CF_2 sticking rate in low power rf discharges.[9]

To address this activation process, polymer deposition on the $SiO_2C_xF_y$ complex is modeled by a two step process. The $SiO_2C_xF_y$ complex sites in the presence of low energy ion

bombardment are activated to form the intermediate $SiO_2C_xF_y$*. The probability of activation of the $SiO_2C_xF_y$ sites for incident energy E_i scales as

$$p(E_i) = p_0 \times \max\left(0, 1 - \frac{E_i}{E_c}\right), \tag{3.12}$$

where E_c is the maximum energy of the process, and p_0 is the probability at zero incident energy. CF_x and C_xF_y radicals have a higher sticking probability to the activated sites and thus forms the first layer of the polymer. Subsequent polymer growth can occur on top of this first layer.

Once the substrate is covered with a monolayer of polymer, the incoming radicals and ions do not see the underlying substrate and hence the growth in polymer must be independent of the underlying substrate. However Schaepkens *et al*. observed that prior to saturation the polymer layer is thinner on SiO_2 than on Si.[11] This suggested polymer consumption processes at the SiO_2-polymer interface. The oxygen atoms in SiO_2 can react with the carbon and fluorine in the polymer network to consume polymer and simultaneously release etch products like CO_x, COF_x. Oehrlein *et al*. observed that the SiO_2 and Si etch rates in general decrease with increasing polymer layer thickness, which scales inversely with bias.[11-13] This suggested that the polymer consumption process at the interface increased at higher substrate biases and is enhanced by energetic ions. This process is modeled as a chemical enhanced sputtering process, with an energy dependence following Eq. (3.5). The $SiO_2C_xF_y$ complex formed at the polymer-wafer interface undergoes chemically enhanced sputtering and dissociates into $SiOCF_y$ and releases COF_x as etch products. $SiOCF_y$ in turn undergoes chemically enhanced sputtering to dissociate in to SiF_3 and releases CO_x as etch products. SiF_3 is finally sputtered to etch away the

wafer and in the process release SiF_3 as etch product. SiF_3 is also consumed by F atom etching to release SiF_4.

Polymer formation and consumption process occur simultaneously, producing a steady state polymer layer thickness. Other main polymer consumption processes are physical sputtering and F atom etching. Similar to chemically enhanced sputtering, physical sputtering of the polymer layer increases with ion energy as in Eq. (3.5). In the case of F atom etching, F radicals terminate the dangling bonds of carbon in the polymer chains to release volatile etch products such as CF_2. For fluorocarbon gas chemistries with H in the gas phase such as CHF_3, the H radicals can stick to the fluorocarbon polymer network as side chains and functional groups. As a result, the polymer composition in such systems can be significantly different from that of pure fluorocarbon chemistries. We account for this possibility in our model by hydrogenated polymer species. This specie has reactions similar to the fluorocarbon polymer, except for the probability and the threshold energy of the physical sputtering reaction.

Etching in Si is similar to SiO_2, in that it proceeds through the formation of a steady state polymer layer. The fluorocarbon radicals have a significant sticking probability to the Si surface, even in the absence of ion activation. Further, the process of oxygen in SiO_2 consuming the polymer layers is absent in Si. As a result, polymer layers are generally thicker during Si etching. This in turn lowers the physical sputtering of the polymer by energetic ions due to a lower delivery of activation energy. This compounds the increase in the polymer layer thickness. The main etch mechanism in Si is fluorination by F radicals to form SiF, SiF_2 and SiF_3 progressively. SiF_x is consumed by ion sputtering to release SiF_n gas and by F atom etching of SiF_3 to release SiF_4.

Typically when ions hit the surface, apart from activating reactions on the surface, they also deliver energy to the underlying layers. For example, ions hitting the polymer surface in addition to sputtering the polymer at the point of contact, may also deliver energy to the interface complex sites and induce chemically enhanced sputtering of the complex to release etch products. However, this delivery of activation energy is not incorporated into our surface reaction mechanism.

3.3.2 Etching of Organic Polymer in Oxygen Plasma and Cu IMPVD

The removal of organic polymer using plasmas has widespread applications and has been extensively characterized. Early applications include reactive ion etching of organic material in multilevel resist systems in an oxygen plasma.[14,15] Recent applications are the removal of organic contaminants and residual polymers following fluorocarbon etching.[16,17] O_2 plasmas currently are also being investigated for patterning organic low-k dielectrics. Investigations of the mechanisms concentrate on the contribution of the major reactive species $O_2(^1\Delta)$, $O(^4S)$, $O(^1D)$, O^+ and O_2^+.[18,19] The effectiveness of removal of organic material in both fluorocarbon and hydrocarbon polymers by O_2 plasmas is due to the reaction of oxygen with the carbon in the polymer. This results in the breaking of the C-F and C-H bonds and in the formation of volatile byproducts such as H_2O and CO_x in case of hydrocarbon polymers and COF_x, CO_x and F_x in case of fluorocarbon polymers.[14]

In high-pressure (0.5-5 Torr) oxygen discharges, O atoms are the primary etchant species.[20,21] Etching by O radicals was found to be thermally activated with E_{act} = 0.25–0.5 eV for a variety of organic materials that were etched such as poly-methyl-metha-acrylate (PMMA) and a phenol formaldehyde based photoresist (AZ 1350J, Shipley Co.).[20,21] The substrates are typically heated to 100s °C. Similar trends are found in low-pressure reactive ion etching (RIE)

of polyimide in Ar/O_2 plasma, where, for example, Selwyn reported that the O radicals are the main etchant species.[22] Harper et al investigated etching of polyimide by Ar^+ and O_2^+ beams. They found that the etching was six times slower using the Ar^+ ion beam, differences attributed to increased activation by the neutral O radicals on the surface sites.[23] Similar low etch rates were observed in pure O_2 plasmas with low ion activation. For example, Egitto *et al*. observed little etching of polyimide in pure O_2 plasmas where they shielded the polymer from ion bombardment allowing only diffusion of radicals and thermal ions to the polymer surface.[24] When polymer films are exposed to such oxygen discharges without ion bombardment, their top surfaces are oxidized, creating a passivation layer, which stops further etching.

These observations suggest an ion-assisted mechanism for the etching of organic materials. Greer *et al*. observed that the etching of photoresist by an oxygen ion beam is limited by the availability of O radicals at low pressures and by ions at higher pressures.[25] In modeling of this etch mechanism, Baggerman *et al*. proposed a similar process.[15] Steinbruchel *et al*. suggested a surface-damage promoted etching mechanism, where the ion impact creates a damaged surface with higher reactivity, which on subsequent attack by neutrals release the etch products.[14] Joubert *et al*. suggested an alternate reaction pathway where oxygen radicals first adsorb on the polymer surface. The etch reaction is then completed by activation by energetic ions.[26]

Based on these observations and suggested reaction pathway by Joubert *et al*[26], we modeled the fluorocarbon polymer etch mechanism as a two-step ion-assisted process. Oxygen atoms first react with the polymer to produce an activated polymer site (P_s*). Upon delivery of activation energy by ions, the activated polymer complex evolves volatile etch products.

$$P_S + O_g \rightarrow P_S^* \tag{3.13}$$

$$P_S^* + I_g^+ \rightarrow (COF)_g + I_h \tag{3.14}$$

where P is the polymer, P* is the activated polymer complex, I^+ is the ion, I_h is the hot neutral, O is the etchant and COF_x is the volatile gas product. The subscripts s and g denote surfaces and gas phase species. The polymer surface can also be directly sputtered by ions to release non-oxygen-containing volatile etch products such as CF_x with an energy dependence governed by Eq. (3.5). The threshold energy and probability for this reaction are based on the reaction mechanism developed for ion sputtering of the fluorocarbon polymer formed during etching of SS. Photoresists are modeled similar to fluorocarbon polymer. The reaction mechanism for oxygen etching of fluorocarbon polymer and photoresist is listed in Table 3.2.

The surface reaction mechanism used for Cu IMPVD has been discussed earlier and is listed in Table 3.3.[3] The primary ions, Ar^+ and Cu^+, sputter Cu and SiO_2 surfaces with an energy dependence given by Eq. (3.5). The angular dependence of sputtering has an energy dependence similar to chemically enhanced sputtering reaction with a maximum near ≈60°. Specular reflection, as given by Eq. (3.6) has $E_c = 0$ eV and $\theta_c = 70°$. In addition to sputtering, deposition also occurs with Cu^+ bombardment. All ions not deposited are converted to hot neutrals at the surface and are treated similarly to ions in the reaction mechanism. Cu ground state and Cu* [$Cu(^2D_{5/2})$] deposit on SiO_2 and Cu surfaces. The sticking probability of Cu and Cu* was estimated to be 0.70 on SiO_2 and 0.95 on Cu.

3.4 Integrated Modeling Using the MCFPM

The capabilities of MCFPM span from simulating feature evolution from etching of the dielectric to deposition of copper interconnects. A schematic of process flow from etching of dielectrics to Cu deposition is shown in Fig. 3.2. Typical profile simulations for integrated modeling obtained using the MCFPM, namely, fluorocarbon etching, stripping of residual fluorocarbon polymer, resist removal and barrier coating using Cu IMPVD, are presented in this section. Profiles for integrated modeling of SS film are shown in Fig. 3.3, and for PS film with closed pores of 16 nm average pore radius and 50% porosity are shown in Fig. 3.4. The ICP reactor used for both etching and stripping conditions is explained in Section. 2.3. Process conditions for etching are as described in Section. 2.3. Process conditions for residual fluorocarbon and resist stripping are a Ar/O_2 = 94/6 flow rate of 40 sccm, pressure of 4 mTorr, ICP power deposition of 600 W at 13.56 MHz and substrate rf bias of 80 V at 3.4 MHz. The process conditions are optimal for the etching, stripping and Cu IMPVD of the SS film. The etching of SS produces fairly vertical sidewalls. The stripping process is efficient in removing both the resist and the residual fluorocarbon. The sputtering damage during the stripping process is also minimal. The Cu IMPVD process for barrier coating is conformal on the SS film.

For the PS film the taper of the etched via is similar to the SS film. The presence of pores, however, gives a jagged topology to the final profile. As the process conditions are highly polymerizing (large fluxes of fluorocarbon radicals), the pores get filled with polymer, which is problematic during the stripping process, where the polymer inside the larger pores are not cleaned completely. The stripping process is efficient for resist removal. Cu IMPVD is not conformal onto the PS film and the presence of pores creates voids in the barrier coating.

3.5 Tables

Table 3.1: Surface reaction mechanism for fluorocarbon etching of porous and solid SiO_2.

Species	Symbol
Ions	CF_3^+
Polymerizing Radicals	CF_x, C_xF_y
Fluorocarbon polymer	P
Hydrogenated polymer	HP
Activated Species	*
Gas phase species	g
Hot neutrals	h
Surface species	s

Reaction[a,b]	p_0	E_c(eV)	Reference
Formation of complex at polymer-SiO_2 interface:	p_0		
$SiO_{2s} + CF_{xg} \rightarrow SiO_2CF_{xs}$	0.1		
$SiO_{2s} + C_xF_{yg} \rightarrow SiO_2C_xF_{ys}$	0.1		
Low energy Ion activation to form activated complex site	p_0	E_c(eV)	
$SiO_2CF_s + CF_{3g}^+ \rightarrow SiO_2CF_s^* + CF_{3h}$	0.1	70	Eq. (3.12)
$SiO_2CF_{2s} + CF_{3g}^+ \rightarrow SiO_2CF_{2s}^* + CF_{3h}$	0.1	70	Eq. (3.12)
$SiO_2C_2F_{3s} + CF_{3g}^+ \rightarrow SiO_2C_2F_{3s}^* + CF_{3h}$	0.1	70	Eq. (3.12)
$SiO_2C_2F_{4s} + CF_{3g}^+ \rightarrow SiO_2C_2F_{4s}^* + CF_{3h}$	0.1	70	Eq. (3.12)
$SiO_2CF_s + CF_{3g}^+ \rightarrow SiO_2CF_s + P_s$	0.1	70	Eq. (3.12)
$SiO_2CF_{2s} + CF_{3g}^+ \rightarrow SiO_2CF_{2s} + P_s$	0.1	70	Eq. (3.12)

$SiO_2C_2F_{3s} + CF_{3g}^+ \rightarrow SiO_2C_2F_{3s} + P_s$	0.1	70			Eq. (3.12)
$SiO_2C_2F_{4s} + CF_{3g}^+ \rightarrow SiO_2C_2F_{4s} + P_s$	0.1	70			Eq. (3.12)

Ion activated dissociation of complex	p_0	E_{th}(eV)	E_r(eV)	n	
$SiO_2CF_s + CF_{3g}^+ \rightarrow SiO_{2s} + CF_g + CF_{3h}$	0.08	70	140	0.97	Eq. (3.5)
$SiO_2CF_{2s} + CF_{3g}^+ \rightarrow SiO_{2s} + CF_{2g} + CF_{3h}$	0.08	70	140	0.97	Eq. (3.5)
$SiO_2C_2F_{3s} + CF_{3g}^+ \rightarrow SiOCF_{3s} + CO_g + CF_{3h}$	0.90	70	140	0.97	Eq. (3.5)
$SiO_2C_2F_{3s} + CF_{3g}^+ \rightarrow SiO_{2s} + C_2F_{3g} + CF_{3h}$	0.03	70	140	0.97	Eq. (3.5)
$SiO_2C_2F_{4s} + CF_{3g}^+ \rightarrow SiOCF_{4s} + CO_g + CF_{3h}$	0.90	70	140	0.97	Eq. (3.5)
$SiO_2C_2F_{4s} + CF_{3g}^+ \rightarrow SiO_{2s} + C_2F_{4g} + CF_{3h}$	0.03	70	140	0.97	Eq. (3.5)
$SiOCF_{3s} + CF_{3g}^+ \rightarrow SiF_{2s} + COF_g + CF_{3h}$	0.01	70	140	0.97	Eq. (3.5)
$SiOCF_{4s} + CF_{3g}^+ \rightarrow SiF_{3s} + COF_g + CF_{3h}$	0.01	70	140	0.97	Eq. (3.5)
$SiO_2CF_s^* + CF_{3g}^+ \rightarrow SiO_{2s} + CF_g + CF_{3h}$	0.08	70	140	0.97	Eq. (3.5)
$SiO_2CF_{2s}^* + CF_{3g}^+ \rightarrow SiO_{2s} + CF_{2g} + CF_{3h}$	0.08	70	140	0.97	Eq. (3.5)
$SiO_2C_2F_{3s}^* + CF_{3g}^+ \rightarrow SiOCF_{3s} + CO_g + CF_{3h}$	0.90	70	140	0.97	Eq. (3.5)
$SiO_2C_2F_{3s}^* + CF_{3g}^+ \rightarrow SiO_{2s} + C_2F_{3g} + CF_{3h}$	0.03	70	140	0.97	Eq. (3.5)
$SiO_2C_2F_{4s}^* + CF_{3g}^+ \rightarrow SiOCF_{4s} + CO_g + CF_{3h}$	0.90	70	140	0.97	Eq. (3.5)
$SiO_2C_2F_{4s}^* + CF_{3g}^+ \rightarrow SiO_{2s} + C_2F_{4g} + CF_{3h}$	0.03	70	140	0.97	Eq. (3.5)
$SiOCF_{3s}^* + CF_{3g}^+ \rightarrow SiF_{2s} + COF_g + CF_{3h}$	0.01	70	140	0.97	Eq. (3.5)
$SiOCF_{4s}^* + CF_{3g}^+ \rightarrow SiF_{3s} + COF_g + CF_{3h}$	0.01	70	140	0.97	Eq. (3.5)
$SiF_{3s}^* + CF_{3g}^+ \rightarrow SiF_{3g} + CF_{3h}$	0.99	70	140	0.97	Eq. (3.5)

Reactions with polymerizing species	p_0
$SiO_2CF_s + CF_{xg} \rightarrow SiO_2C_2F_{3s}$	0.10
$SiO_2CF_{2s} + CF_{xg} \rightarrow SiO_2C_2F_{4s}$	0.10
$SiO_2CF_s^* + CF_{xg} \rightarrow SiO_2CF_s + P_s$	0.5
$SiO_2CF_{2s}^* + CF_{xg} \rightarrow SiO_2CF_{2s} + P_s$	0.5
$SiO_2C_2F_{3s}^* + CF_{xg} \rightarrow SiO_2C_2F_{3s} + P_s$	0.5
$SiO_2C_2F_{4s}^* + CF_{xg} \rightarrow SiO_2C_2F_{4s} + P_s$	0.5
$SiO_2CF_s^* + C_xF_{yg} \rightarrow SiO_2CF_s + P_s$	0.5
$SiO_2CF_{2s}^* + C_xF_{yg} \rightarrow SiO_2CF_{2s} + P_s$	0.5
$SiO_2C_2F_{3s}^* + C_xF_{yg} \rightarrow SiO_2C_2F_{3s} + P_s$	0.5
$SiO_2C_2F_{4s}^* + C_xF_{yg} \rightarrow SiO_2C_2F_{4s} + P_s$	0.5
$Si_s + CF_{xg} \rightarrow Si_s + P_s$	0.15
$Si_s + C_xF_{yg} \rightarrow Si_s + P_s$	0.15
$SiF_s + CF_{xg} \rightarrow SiF_s + P_s$	0.15
$SiF_{2s} + CF_{xg} \rightarrow SiF_{2s} + P_s$	0.15
$SiF_s + C_xF_{yg} \rightarrow SiF_s + P_s$	0.15
$SiF_{2s} + C_xF_{yg} \rightarrow SiF_{2s} + P_s$	0.15
$SiF_{3s} + CF_{xg} \rightarrow SiF_{3s} + P_s$	0.15
$SiF_{3s} + C_xF_{yg} \rightarrow SiF_{3s} + P_s$	0.15

Fluorination	p_0
$Si_s + F_g \rightarrow SiF_s$	0.05

$SiF_s + F_g \rightarrow SiF_{2s}$	0.05				
$SiF_{2s} + F_g \rightarrow SiF_{3s}$	0.05				
$SiF_{3s} + F_g \rightarrow SiF_{4g}$	0.10				
$SiO_2CF_s + F_g \rightarrow SiF_{2s} + CO_{2g}$	0.01				
$SiO_2CF_{2s} + F_g \rightarrow SiF_{3s} + CO_{2g}$	0.01				

Reactions on polymer surface	p_0	E_{th}(eV)	E_r(eV)	n	
$P_s + F_g \rightarrow CF_{2g}$	0.03				
$P_s + H_g \rightarrow P_s + HP_s$	0.90				
$P_s + C_xF_{yg} \rightarrow P_s + P_s$	0.15				
$P_s + CF_{xg} \rightarrow P_s + P_s$	0.15				
$P_s + CF_{3g}^+ \rightarrow CF_{3h} + CF_{2g}$	0.15	70	140	0.97	Eq. (3.5)
$HP_s + F_g \rightarrow CF_{2g}$	0.03				
$HP_s + H_g \rightarrow HP_s + HP_s$	0.99				
$HP_s + C_xF_{yg} \rightarrow HP_s + HP_s$	0.05				
$HP_s + CF_{xg} \rightarrow HP_s + HP_s$	0.05				
$HP_s + CF_{3g}^+ \rightarrow CF_{3h} + CF_{2g}$	0.28	125	175	0.98	Eq. (3.5)

a. Reactions for CF_{3g}^+ are generic for all ions. All ions return as a hot neutral. Ions and hot neutrals have the same mechanism.
b. In reactions with no chemical change, the gas species are reflected of the surface. These reactions are not shown in the table.

Table 3.2: Surface reaction mechanism for oxygen etching of fluorocarbon polymer and photoresists.

Species	Symbol
Fluorocarbon polymer	P
Photoresist	R
Activated Species	*
Ions	I^+
Gas phase species	g
Hot neutrals	I_h
Surface species	s

Reaction[a,b]	p_0	E_{th}, E_r, n[c]	Reference
$P_s + O_g \rightarrow P_s*$	0.50		
$P_s* + I_g^+ \rightarrow COF_{xg} + I_h$	0.03	45, 100, 0.4	Eq. (3.5)
$P_s + I_g^+ \rightarrow CF_{xg} + I_h$	0.15	70, 140, 0.97	Eq. (3.5)
$R_s + O_g \rightarrow R_s*$	0.01		
$R_s* + I_g^+ \rightarrow COF_{xg} + I_h$	0.30	100, 500, 0.8	Eq. (3.5)
$R_s + I_g^+ \rightarrow CF_{xg} + I_h$	0.20	100, 500, 0.8	Eq. (3.5)

a. Reactions for CF_{3g}^+ are generic for all ions. All ions return as a hot neutral. Ions and hot neutrals have the same mechanism.
b. In reactions with no chemical change, the gas species are reflected of the surface. These reactions are not shown in the table.
c. Threshold and reference energies are in eVs.

Table 3.3: Surface reactions for Cu deposition in an Ar buffer gas. s refers to surface species and g refers to gas species.

Reaction[a,b]	p_0	E_{th}, E_r, n[c]	Reference
$Ar^+ + Cu_s \rightarrow Ar_g + Cu_g$	0.35	45, 100, 1	Eq. (3.5)
$Ar^+ + SiO_{2s} \rightarrow Ar_g + SiO_{2g}$	0.10	45, 100, 0.5	Eq. (3.5)
$Cu^+ + Cu_s \rightarrow Cu_g + Cu_g$	0.35	45,100, 1	Eq. (3.5)
$Cu^+ + Cu_s \rightarrow Cu_s + Cu_s$	0.55		
$Cu^+ + Cu_s \rightarrow Cu_g + Cu_s$	0.10		
$Cu^+ + SiO_{2s} \rightarrow Cu_g + SiO_{2g}$	0.10	45,100,0.5	Eq. (3.5)
$Cu^+ + SiO_{2s} \rightarrow Cu_s + SiO_{2s}$	0.80		
$Cu^+ + SiO_{2s} \rightarrow Cu_s + SiO_{2g}$	0.10		
$Cu_g + Cu_s \rightarrow Cu_s + Cu_s$	0.95		
$Cu_g + SiO_{2s} \rightarrow Cu_s + SiO_{2s}$	0.70		

a. Reactions for CF_{3g}^+ are generic for all ions. All ions return as a hot neutral. Ions and hot neutrals have the same mechanism.
b. In reactions with no chemical change, the gas species are reflected of the surface. These reactions are not shown in the table.
c. Threshold and reference energies are in eVs.

3.6 Figures

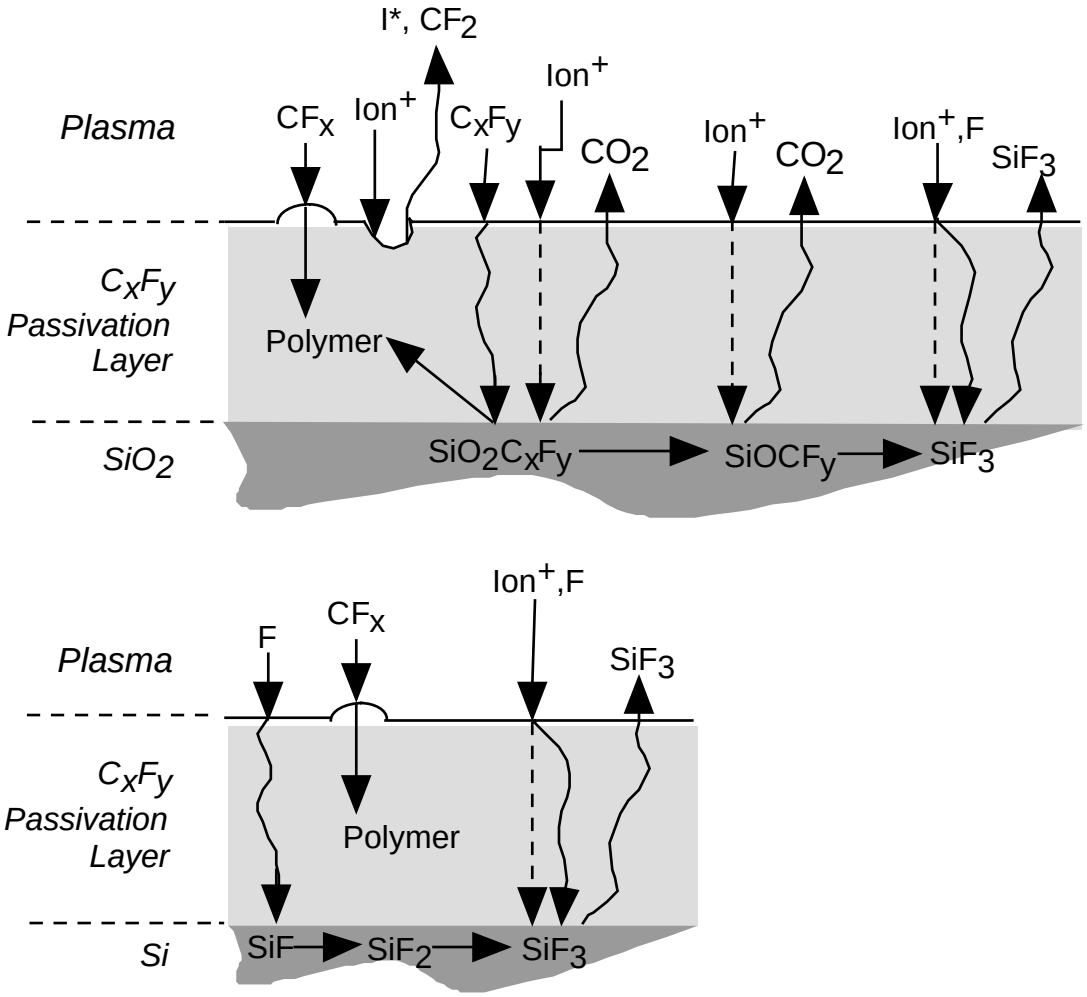

Fig. 3.1. Schematic of surface reaction mechanism for fluorocarbon etching of SiO_2/Si. I^+ refers to an ion. I* refers to a hot neutrals. The dashed lines represent energy transfer through the polymer. The curved lines represent species diffusion through the polymer.

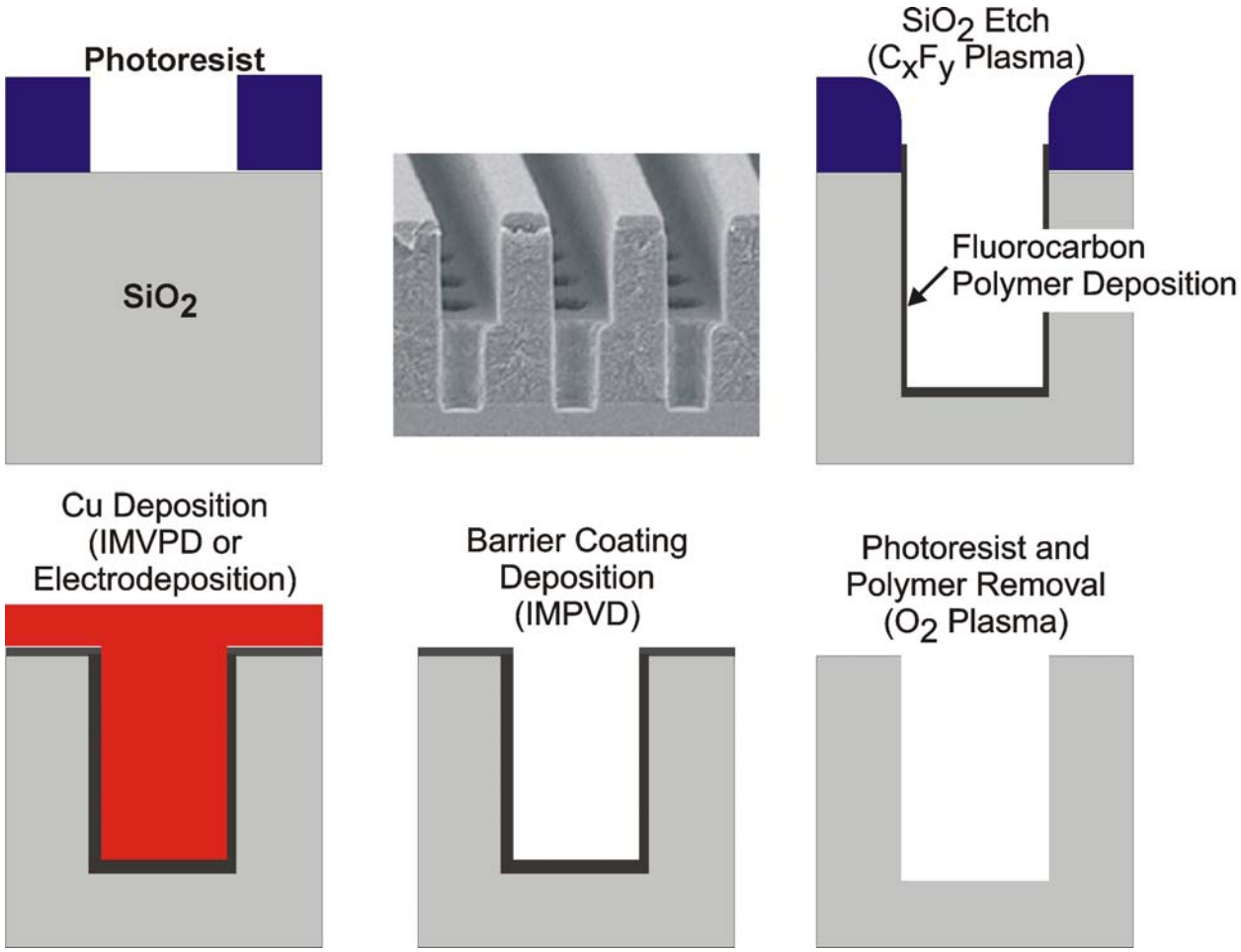

Fig. 3.2. Schematic of process flow from etching of dielectric to copper deposition during microelectronics fabrication.

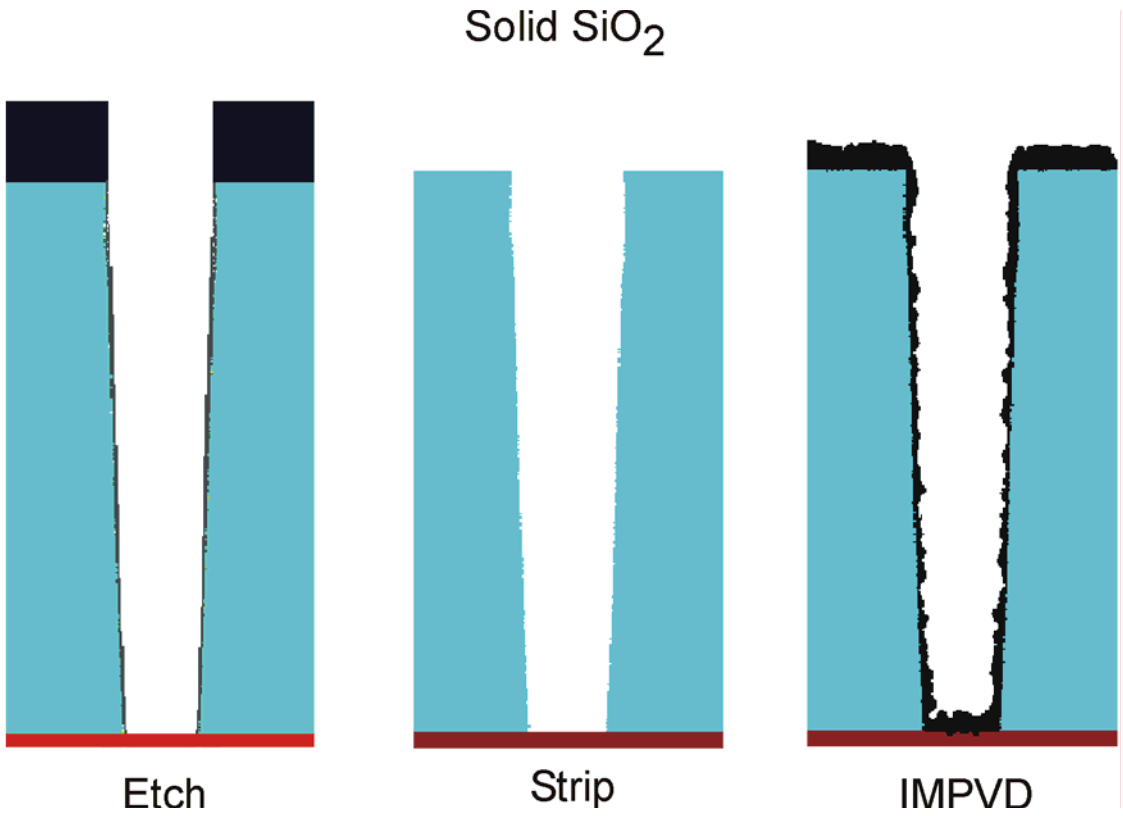

Fig. 3.3. Etch, strip and fill of a solid SiO_2 film. Etching process conditions: CHF_3, 6 mTorr, 40 sccm gas flow rate, 1400 W ICP power, -65 V dc bias. Stripping process conditions: Ar/O_2 = 94/6, 4 mTorr, 40 sccm gas flow rate, 1400 W ICP power at 13.56 MHz, 80 V rf bias at 3.4 MHz.

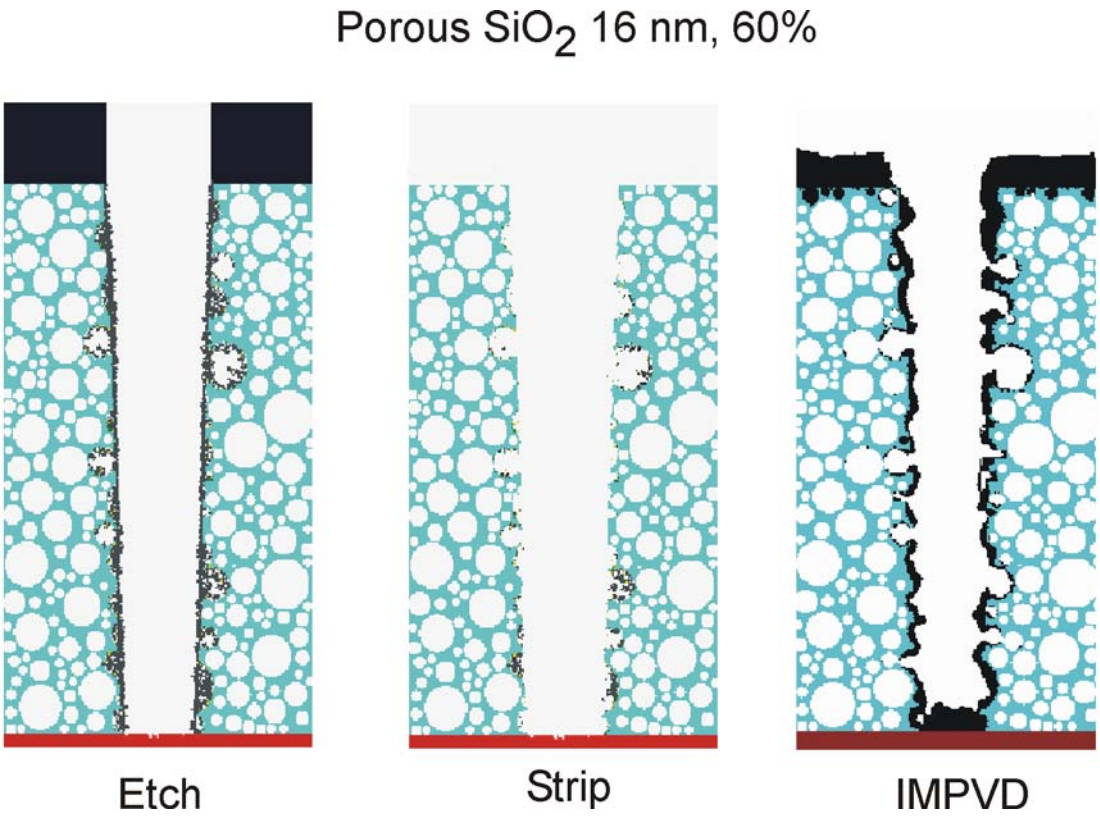

Fig. 3.4. Etch, strip and fill of a porous SiO_2 film. Process conditions are as described in Fig. 3.3.

3.7 References

[1] R. J. Hoekstra, M. J. Grapperhaus, and M. J. Kushner, J. Vac. Sci. Technol. A **15,** 1913 (1997).

[2] R. J. Hoekstra and M. J. Kushner, J. Vac. Sci. Technol. B **16,** 2102 (1998).

[3] J. Lu and M. J. Kushner, J. Vac. Sci. Technol. A **19,** 2652 (2001).

[4] C. C. Cheng, K. V. Guinn, V. M. Donnelly, and I. P. Herman, J. Vac. Sci. Technol. A **12,** 2630 (1994).

[5] C. F. Abrams and D. B. Graves, J. Appl. Phys. **86,** 2263 (1999).

[6] M. Matsui, T. Tatsumi, and M. Sekine, J. Vac. Sci. Technol. A **19,** 2089 (2001).

[7] B. E. E. E. Kastenmeier, P. J. Matsui, and G. S. Oehrlein, J. Vac. Sci. Technol. A **`6,** 2047 (1998).

[8] M. Inayoshi, M. Ito, M. Hori, T. Goto, and M. Hiramatsu, J. Vac. Sci. Technol. A **16,** 233 (1998).

[9] J. P. Booth, G. Cunge, P. Chabert, and N. Sadeghi, J. Appl. Phys. **85,** 3097 (1999).

[10] D. C. Gray, I. Tepermeister, and H. H. Sawin, J. Vac. Sci. Technol. B **11,** 1243 (1993).

[11] M. Schaepkens, T. E. F. M. Standaert, N. R. Rueger, P. G. M. Sebel, G. S. Oeherlein, and J. M. Cook, J. Vac. Sci. Technol. A **17,** 26 (1999).

[12] N. R. Rueger, J. J. Beulens, M. Schaepkens, M. F. Doemling, J. M. Mirza, T. E. F. M. Standaert, and G. S. Oehrlein, J. Vac. Sci. Technol. A **15,** 1881 (1997).

[13] G. S. Oehrlein and J. F. Rembetski, IBM J. Res. Develop. **36,** 140 (1992).

[14] C. Steinbruchel, B. J. Curtis, H. W. Lehmann, and R. Widmer, IEEE Trans. Plasma Sci. **14,** 137 (1986).

[15] E. J. H. Collart, J. A. G. Baggerman, and R. J. Visser, J. Appl. Phys. **78,** 47 (1995).

[16] K. Ueno, V. M. Donnelly, and Y. Tsuchiya, J. Vac. Sci. Technol. B **16,** 2986 (1998).

[17] D. Shamiryan, M. R. Baklanov, S. Vanhaelemeersch, and K. Maex, J. Vac. Sci. Technol. B **20,** 1923 (2002).

[18] J. A. G. Baggerman, R. J. Visser, and E. J. H. Collart, J. Appl. Phys. **75,** 758 (1994).

[19] W. E. Vanderlinde and A. L. Ruoff, J. Vac. Sci. Technol. B **6,** 1621 (1988).

[20] D. L. Flamm and V. M. Donnelly, Plasma Chem. Plasma Proc. **1,** 317 (1981).

[21] J. M. Cook and B. W. Benson, J. Electrochem. Soc **130,** 2459 (1983).

[22] G. S. Selwyn, J. Appl. Phys. **60,** 2771 (1986).

[23] M. E. Harper, J. J. Cuomo, and H. R. Kaufman, Annu. Rev. Mater. Sci **13,** 413 (1983).

[24] F. D. Egitto, F. Emmi, R. S. Horwath, and V. Vukanovic, J. Vac. Sci. Technol. B **3,** 893 (1985).

[25] F. Greer, L. Van, D. Fraser, J. W. Coburn, and D. B. Graves, J. Vac. Sci. Technol. B **20,** 1901 (2002).

[26] O. Joubert, J. Pelletier, and Y. Arnal, J. Appl. Phys. **65,** 5096 (1989).

4. FLUOROCARBON ETCHING OF POROUS AND NONPOROUS SiO_2

4.1 Introduction

Increases in RC delay times in interconnect wiring for microelectronics as feature sizes decrease has motivated investigations into the use of low-k insulators, and in particular PS. Profile evolution and maintenance of critical dimensions during plasma etching of PS are problematic due to the exposure of open pores. To investigate these issues, the surface reaction mechanism for fluorocarbon plasma etching of SiO_2 in C_2F_6, CHF_3 and C_4F_8 gas chemistries, which was described in Section 3.3.1 has been incorporated into the two-phase MCFPM (described in Chapter 3) and the results from this investigation are presented in this chapter. Validation of the surface reaction mechanism and the two-phase model will be presented in Section 4.2 and 4.3. Results from the MCFPM for etching of PS and SS in high aspect ratio (HAR) trenches will be discussed in Section 4.4 followed by concluding remarks in Section 4.5.

4.2 Validation of Surface Reaction Mechanism for Fluorocarbon Etching of SiO_2/Si

The surface reaction mechanism for fluorocarbon etching of SiO_2/Si, described in Section. 3.3.1 was calibrated and validated for blanket etching of SiO_2 and Si in C_2F_6, C_4F_8 and CHF_3 chemistries. The cylindrical ICP reactor used for this study, shown in Fig. 4.1, is patterned after that used by Schaepkens *et al*.[1] Inductive power is supplied through a 3-turn coil, 16 cm in diameter. The coil sits on a 2 cm thick quartz window, which is 23 cm in diameter. The wafer is on a substrate 7 cm below the quartz window and can be independently biased. For the base case, the gas flow rate is 40 sccm and the pressure is 6 mTorr. The coil source current is at 13.56 MHz and delivers an inductive power of 1400 W. The rf bias voltage was varied to obtain the

required dc self-bias for comparison to experiments. Power deposition and selected neutral and ion densities in a C_2F_6 plasma are shown in Fig. 4.1.

Power deposition is restricted to the top of the reactor to within the skin depth of the electromagnetic field, which is a few cm. The large electron density ($\approx 10^{11}$ cm^{-3}) highly dissociates the C_2F_6 feedstock gases, whose density peaks near the input nozzle. As a result of the high degree of dissociation, the major neutral radicals are CF, CF_2, and F, and the most prominent ions are CF_2^+, F^+ and CF_3^+. As diffusive transport dominates at low pressures, CF_2 and CF_2^+densities are larger near the center of the reactor. Due to large rates of recombination of CF_2^+ at the walls, the CF_2 density increases near the walls of the reactor.

Radical and ion fluxes to the wafer for the base case conditions for a C_2F_6 plasma are shown in Fig. 4.2. Lower F atom and ion fluxes may result in a thicker passivation layer near the edge of the wafer. In contrast, decreasing polymerizing neutral fluxes may result in a thinner polymer near the edges. The net result of the two opposing effects is that the etch rates near the edge of the wafer were slightly lower than at the center. Total ion energy distribution for the base case conditions for a C_2F_6 plasma is shown in Fig. 4.3. The ions have a fairly narrow spread in energy averaged ≈200 eV and the distribution is representative of the prominent ions, namely CF_2^+, CF_3^+ and F^+. The angular spread of the distribution <10°.

ER as a function of self-bias for blanket etching of SiO_2 and Si in a C_2F_6 plasma compared to experiments for the base case conditions is shown in Fig. 4.4(a).[1] The onset of the etching of SiO_2 occurs at -20 V self bias. At low biases and low ion energies, the polymer thickness is large (several nm) due to ion-activated polymer deposition, which is most efficient at low energies. There is also only nominal ion sputtering of the polymer at low energies. For reference self generated dc bias voltages as functions of the applied rf bias for these conditions

are shown in Fig. 4.4(c). The relationship between the self-bias and rf bias is fairly linear for all the chemistries. The onset of etching at around -20 V self bias occurs when the polymer is thin enough to allow the delivery of activation energy to the polymer-SiO_2 interface, which initiates the etching reaction releasing volatile etch products like CO_2, COF_x and SiF_x. The ER increases with self-bias, which corresponds to a monotonic decrease in the polymer thickness due to less ion activation of the polymer precursor and more sputtering. At high self-bias and ion energies, the polymer reduces to sub-monolayer thickness leading to insufficient passivation and the ER increase saturates. Similar trends occur for etching of SiO_2 in C_4F_8, as also shown in Fig 4.4.[2] Process conditions in this case are 10 mTorr pressure, 50 sccm gas flow rate and 1400 W ICP power at 13.56 MHz.

The deposition of polymer on Si is rapid due to the lack of polymer-wafer interactions such as those between CF_x in polymer with O in SiO_2,. A thicker polymer layer also lowers the delivery of activation energy to the underlying Si. The net result is that the ERs of Si are typically lower than that of SiO_2. However, the variation of ER with respect to self-bias for Si etching is similar to that of SiO_2 etching.

The thickness of the polymer is critical to determining etch rates and threshold biases. Polymer formation, assisted by low energy ions, and polymer consumption processes (ion assisted reaction at the solid interface and polymer sputtering), promoted by high-energy ions, simultaneously govern the passivation layer thickness. The threshold bias for etching qualitatively delineates the energy of ions below which ion-assisted polymer formation dominates and above which ion-assisted activation at the interface or sputtering dominates. Since the behavior of etch rates as a function of bias voltage is a sensitive function of threshold energy (E_{th}) for ion-activated reactions at the interface, this value was calibrated across all three

chemistries (CHF_3, C_2F_6 and C_4F_8). An example of the calibration process is shown in Fig. 4.5, where etch rate is shown as a function of self-bias for different values of E_{th} for C_2F_6 plasma at 6 mTorr. The average ion energy is roughly V_{dc}, however, the range of ion energies extend to as large as $V_{dc} + V_{rf}$. As E_{th} decreases a larger proportion of the ion EADs extends above the activation energy, there by reducing the bias voltage at which etching begins. At high biases, where significant fractions of ions have energies above the activation energy, increasing the E_{th} had little effect on the etch rate. Based on these results, and similar parameterizations for C_4F_8 and CHF_3, we chose $E_{th} = 70$ eV.

Polymer growth is initiated at the SiO_2 surface through activation by low energy ions. After the first layer of polymer is formed, the neutral fluorocarbon radicals deposit on the existing polymer layer, thereby increasing the polymer thickness. As the thickness of the polymer critically depends on the rate of incorporation, the sticking probability of fluorocarbon radicals on polymer was also calibrated across the three chemistries. This parameterization is shown in Fig. 4.5(b) for C_2F_6 plasma at 6 mTorr. Larger p_0 for fluorocarbon sticking increases the polymer thickness and lowers the etch rates. The significance of this effect increases with substrate bias. Based on these results we chose $p_0 = 0.15$.

The removal of polymer is dominated by ion sputtering. While keeping the threshold energy for sputtering at 70 eV, the reference probability was parameterized for calibration purposes across the three chemistries. This parameterization is shown in Fig. 4.5(c) for C_2F_6 at 6 mTorr. Lowering the sputtering probability leads to a thicker polymer layer, which would require a larger fraction of ions above E_{th} for etching to proceed. This pushes the onset of etching to higher bias voltages. Even at high biases the polymer thickness is large enough that the etch

rates do not saturate with low sputtering probabilities. Based on these results, we chose p_0 = 0.15 for polymer sputtering.

ER as a function of self-bias for SiO_2 and Si in a CHF_3 plasma is shown in Fig 4.6.[1] The process conditions are 6 mTorr pressure, 40 sccm gas flow rate and 1400 W ICP power at 13.56 MHz. Etching of SiO_2 and Si show dissimilar trends. The onset of etching for SiO_2 is ≈-40 V self-bias and for Si is -100 V self bias. Selected radical and ion fluxes to the center of the wafer for the above process conditions for C_2F_6, C_4F_8 and CHF_3 chemistries are listed in Table 4.1. The ratio of F fluxes in C_2F_6 to that in CHF_3 is ≈3.5, which results in higher etching of the polymer and lowers the etch rates in C_2F_6 as compared to CHF_3. In the case of Si etching, since the most prominent etching mechanism is by F atoms, the reduction in the F radical flux has a large effect on the etch rates. As a result there is better selectivity between SiO_2 and Si for CHF_3.

Note that there is a discrepancy in the ERs between model and experiments at higher biases. This is likely due to the omission of H radicals from the surface reaction mechanism. The H radicals are able to cross-link to the fluorocarbon polymer chains and thus change the polymer composition. This different polymer composition was accounted for in the surface reaction mechanism by treating the hydrogenated polymer (HP) as a different species. p_0 and E_{th} for physical sputtering of HP were modified to address this difference. E_{th} was increased to 125 eV and the sputtering probability was increased to 0.28. At low biases, a significant proportion of the ions do not possess the activation energy for the sputtering process. Increasing E_{th} reduces sputtering and increases the polymer thickness. Increasing the sputtering probability compensates and the net result is that there is no change in the threshold for the onset of etching. However, at high biases, the majority of the ions possess the activation energy for sputtering.

Hence, increasing E_{th} to 125 eV has only a nominal effect on the polymer layer thickness. As a result, at these biases the increased p_0 increases the etch rates and bridges the discrepancies noted earlier. The resulting ERs as a function of self-bias are shown in Fig 4.6(b) and are in better agreement with the experiments.

4.3 Etching of Porous Silica (PS)

To validate the mechanism for PS, comparisons were made to experiments for two porous materials (r_0 = 2 nm, 30% porosity; and r_0 = 10 nm and 58% porosity).[2] The Δr_0 (standard deviation of the radius of pore network) was maintained at 50% for r_0 for all cases, unless otherwise specified. ERs as a function of self-bias for PS and SS in CHF_3 and C_4F_8 plasmas are shown in Fig. 4.7 and 4.8. The process conditions are 10 mTorr, 50 sccm gas flow rate and 1400 W ICP power at 13.56 MHz. In general, the ER of PS is higher than SS for otherwise the same conditions due to their inherently lower mass densities. This trend is observed for both CHF_3 and C_4F_8 chemistries. The threshold bias for etching and the dependence of ER on self-bias is similar for PS and SS because of the same governing fundamental reaction chemistry.

To isolate the effects of pores on ER, a corrected ER (ER_c) is defined as

$$ER_c = ER\ (1-p), \tag{4.1}$$

where p is the porosity and ER is the gross etch rate. ER_c is effectively the etch rate per unit mass. If pore morphology had no kinetic effect on etching, then the ER_c of PS should be equal to the ER of SS. ER_c as function of self-bias for CHF_3 and C_4F_8 chemistries is shown in Figs. 4.7(c) and 4.8(c) respectively. In CHF_3 plasmas, the ER_c of 2 nm PS is greater than that of ER of

SS and the ER_c of 10 nm PS is lower than that of SS for all values of self-bias. This result implies that smaller pores enhance the fundamental ER in CHF_3 plasmas. However, in C_4F_8, the ER_c of both 2 nm and 10 nm PS are lower than that of SS, with the ER_c of 10 nm PS being the lowest.

In highly polymerizing environments, a critical parameter, which determines the kinetics of the etching process is the steady-state polymer layer thickness (L). L can vary from a few to many nms, typically 3-8 nms for the chemistries investigated here. This thickness depends on the magnitude and energies of the incident fluxes, which in turn depend on the gas chemistry and process conditions.[2,3] In the case of PS, as the pores are exposed during etching, they can be filled with polymer. Hence the ratio L/r_0, where r_0 is the average pore radius, is significant. For CHF_3 etching of PS with 2 nm pores, L is typically 5-6 nm and greater than r_0. As a result the increase in the local polymer thickness due to pore filling is fractionally small compared to L. Hence pore filling does not lower the ER_c of PS in comparison to ER of SS. Any enhancements are likely physiochemical effects. During the etching of blanket SS, the incident ions are, on average, normal to the surface whereas the optimum angle for chemically enhanced sputtering is ≈60°. When small pores are filled they do not significantly add to the polymer thickness. However, they do present non-normal surfaces to the plasma, which enable more rapid chemically enhanced sputtering. The activation of the polymer-wafer surface is therefore likely to be faster, which produces enhanced ERs. The difference in the ER_c of PS and ER of SS at the threshold self-bias of -40 V is marginal (less than 10%). With an increase in ion energies, this difference increases to as much as 50%.

In the case of C_4F_8 plasmas, L is ≈3-4 nm and comparable to r_0 for 2 nm pores and so on a fractional basis there is an increase in the local polymer thickness. The pore filling effect in

this case is large enough to negate the possible enhancement due to perhaps more optimal chemically enhanced sputtering and results in a slightly lower ER_c. In this case the difference in the ER_c of PS and ER of solid SiO_2 remains fairly uniform at about 50 nm/min.

With 10 nm pores, L is significantly less than r_0 with both CHF_3 and C_4F_8 plasmas. As the pores are opened up by the etching process, they are filled with polymer, resulting in the local polymer thickness on top of the SiO_2 bounding the pore being significantly larger than L. This results in a lower delivery of activation energy to the polymer-SiO_2 interface and a slower rate of etching. Larger open pores also tend to have polymer-SiO_2 interfaces exposed to the ion flux at shallower angles, which is less optimum for activating etch processes. A significant proportion of flux reaching interfaces at other sites on the surfaces of the pores consists of reflected neutrals with energies lower than the incident ion flux. The net result of these effects is that the ER_c of 10 nm PS is significantly lower (~40-50%) than the ER of SS for both CHF_3 and C_4F_8 chemistries.

Computed ER_c and ER as a function of porosity for 2 nm and 10 nm PS etched using a CHF_3 chemistry are shown in Fig. 4.9. The process conditions are the base case with a self-bias of -65 V. As porosity increases with 2 nm pores, there is an increase in the total area of the polymer-SiO_2 interface, which results in increased rates of activation at the interface due to chemically enhanced sputtering. As a consequence, the ER_c increases until a porosity of $\approx$ 25%. As the porosity increases further, the cumulative effect of an increased polymer thickness over a larger number of local pores increases the pore filling effect. This causes the ER_c to saturate. For the 10 nm PS, enhancement in the ER_c is obtained only at low porosities ($\leq$15%). The pore filling effect eventually dominates and causes the ER_c to fall below the ER of solid SiO_2 at a porosity of $\approx$35% at which time the gross ER is maximum. The presence of polymer in pores at

locations which have no view angle to the plasma and so have low sputtering rate, exacerbates this effect. In general large r_0 and larger porosities produce ER_c, which may be smaller than SS.

ER as a function of the interconnectivity for PS samples (10 nm, 60%; and 15 nm, 60%) for the base case conditions and self-bias voltages of -65 V and -110 V in a CHF_3 plasma is shown in Fig. 4.10. Since the total porosity remains the same, ER_c is directly proportional to ER. In an interconnected network, adjacent pores are linked to form a chain with a low fractal dimension as opposed to forming a larger pore. As a result, when one pore opens up during etching, the entire pore chain is exposed to the plasma. As interconnectivity increases, the average length of the opened pore chains increases. Neutral radicals which are polymer precursors can diffuse deep into the interconnected pores. Since polymer formation is a low energy assisted process, reflected low energy neutrals, which are able to penetrate into the pore chains, are able to activate polymer formation even though they have no direct line-of sight to the incident flux. However, the reflected neutrals do not deliver sufficient activation energy within the pore chains to either activate etching at the polymer-wafer interface or to sputter the polymer. This leads to polymer build-up, sometimes deep within the network, which leads to lower ERs at high interconnectivity.

4.4 Profile Simulations of PS Etching in CHF_3 Plasmas

A frequent challenge during microelectronic fabrication is the need to etch vias or trenches having high aspect ratios (HAR) and vertical sidewalls. The goals are often difficult to achieve due to the complex surface reactions on the sidewalls and bottom of the trench. In the case of etching of PS, this is even a more difficult goal to meet due to the complex morphology of the porous and interconnected structures. The challenges of using PS do not stop with the

etching of the via or trench but also extend to the subsequent processing of the vias such as cleaning of the residual polymer.

The time evolution of an HAR profile in a 15 nm, 60% porosity and 0% interconnectivity PS film etched using a CHF_3 plasma for base case conditions (with a self-bias of -65 V) is shown in Fig 4.11. The width of the trench is 100 nm and the aspect ratio is 5. The opening of pores, then filling with polymer and the subsequent etching of the filled pore occurs sequentially as the profile evolves. The filling of pores slows down the etching in the vertical direction due to the thicker effective polymer layers. However, the filling of pores or lining of pores with polymer on the sidewalls does not cause any additional tapering of the profile. The tapering of the profile is a result of the sidewall passivation, which stops lateral etching, and is more dependent on the process conditions than on the pore morphology. Although the filling of the side pores does not significantly change the taper of the final etched via, it does create a problem in the subsequent removal of the filled polymer. Also the presence of pores on the sidewalls leads to a jagged topology of the etched via, which is more pronounced for larger radii, which could present challenges for the later deposition of barrier coatings or seed layers.

Etch depths and corrected etch depths after equal etch times as a function of porosity for HAR trenches for different average pore radii (r_0 = 4 nm, 10 nm and 15 nm) are shown in Fig. 4.12. In agreement with earlier observations for blanket etching, smaller pore radii enhance the rate of etching. This effect is more pronounced as the porosity increases due to there being a larger surface area for more favorable angles of incidence of the ions. However, as the pore radius increases the effect of pore filling starts to dominate and the ER_c starts to decrease. For 10 nm PS, the maxima in ER_c is at ≈20% porosity and the ER_c decreases below the ER of SS at ≈50% porosity. Larger pores, (15 nm) for which filling is even more effective, show little if any

enhancement. The maximum in ER_c occurs at ≈10% porosity and the ER_c is less than ER of SS for porosities >30%.

Etch depths and corrected etch depths for HAR trenches after equal etch times as a function of pore radius for etching of a 50% PS film in a CHF_3 plasma are shown in Fig. 4.13. Profiles of the trenches are also shown. The process conditions are the base case with a self-bias of -65 V. The final tapers for the different pore radii are quantitatively similar, substantiating the earlier observation that the average pore radius and porosity have little effect on the taper of the profile, at least not in any systematic manner. However, etched vias with larger pores have a more jagged topology and would be harder to clean. As the pore radii increases, L/r_0 decreases monotonically. This produces a uniform increase in the pore filling, and so ER and ER_c decrease uniformly.

Etch depth after equal etch times and the profile as a function of interconnectivity for 10 nm, 60% PS etched in a CHF_3 plasma are shown in Fig. 4.14. The taper is given by the ratio W_b/W_t, where W_b is the width of the taper 400 nm above the bottom of the trench and W_t = 100 nm is the width at the top of the trench. Although the pore radius and porosity have little effect on the taper, interconnectivity decreases the taper. From a near vertical profile for a closed pore network, the profile gradually bows with increasing interconnectivity. The presence of interconnected paths open up more surface area for etching to proceed, which despite the pore filling leads to some bowing. The downside is that polymer can be found deep within the pore network. In accordance with earlier observations for blanket etching, the etch depth decreases with increase in interconnectivity due to polymer build-up.

The critical dimensions of the etched profiles depend on the incident magnitudes and energies of the reactant fluxes. With porous substrates, the pore filling effect might be expected

to be sensitive to changes in the incident fluxes and process conditions. To this end, the ratio of the incident polymerizing flux to the ion flux, Φ_n/Φ_{ion}, has been artificially varied to investigate the effect of the composition of the incident flux on etch characteristics. These simulations do not, however, correspond to any particular set of process conditions. The ER, ER_c and taper of PS (2 nm, 30%; and 10 nm, 58%) and SS as a function of Φ_n/Φ_{ion} for etching in a CHF_3 are shown in Fig. 4.15 (Φ_n/Φ_{ion} = 0.4 corresponds to the base case with a self-bias of –110 V). The sidewall passivation generally increases with increasing Φ_n/Φ_{ion} due to the larger flux of the polymerizing radicals. This results in lower rates of etching and produces a narrower profile. An increase in Φ_n/Φ_{ion} also produces thicker polymer layers on the bottom of the trench, which slows the rate of etching. At low values of Φ_n/Φ_{ion} there is insufficient passivation on the bottom of the trench, such that the polymer thickness approaches and broaches a monolayer, and the etch rates are lower than the optimal value. As a consequence, there is a maximum for the ER of SS at $\Phi_n/\Phi_{ion} \approx 2.5$.

ER and taper of PS follow similar trends with respect to Φ_n/Φ_{ion}. As the polymerizing flux increases, pore filling increases and the ER_c of PS decreases below the ER of SS at $\Phi_n/\Phi_{ion} \approx 3$. However, with an increase in the polymerizing flux, pore filling increases disproportionately as pores are opened resulting in excessive polymer build-up on the local sites. This leads to a non-linear increase in the effective polymer layer thickness. Hence the gross ER of the porous materials decreases below the ER of solid SiO_2 at $\Phi_n/\Phi_{ion} \approx 3$. For the same reasons, cessation of etching in porous materials occurs at Φ_n/Φ_{ion} values which are less than that for SS. Profiles of HAR trenches of SS and PS (10 nm, 58%) for the same conditions are shown in Fig. 4.16. The occurrence of etch stop at lower depths and the increase in taper as Φ_n/Φ_{ion} increases is seen for both SS and PS.

ER, ER_c and taper for HAR trenches as a function of self-bias for base case CHF_3 etching are shown in Fig. 4.17. An increase in the bias leads to larger average ion energies. This reduces the passivation layer thickness on both the side walls and the trench bottom. This produces wider profiles as the profiles transition from tapered to vertical to bowed as the bias is increased. However, the increase in etch rate with bias saturates at high biases, in accordance with earlier observations for blanket etching. The scaling with respect to self-bias remains the same for both PS and SS. The saturation of the etch rate with bias for PS in HAR occurs at lower biases than for blanket etching. This is likely due to the lower average ion/neutral energy at the bottom of the trench due to sidewall scatter. ER_c shows an increased enhancement as the self-bias increases. Higher energy ions reduce the polymer build-up due to pore filling by improved sputtering of the polymer and an increased delivery of activation energy.

4.5 Concluding Remarks

The surface reaction mechanism for etching of porous and solid SiO_2 in fluorocarbon gas chemistries was validated by comparison to experiments. Etching of porous silica and solid SiO_2 were found to obey similar scaling laws. However, the mass corrected etch rates may differ from the etch rates of solid SiO_2 depending on the degree of pore filling by polymers and the propensity of chemically enhanced sputtering. For small pores, where $L/r_0 > 1$, etch rates are enhanced due to there being a larger proportion of ions striking the surface with near optimal angles and increasing the chemical sputtering. Whereas for $L < r_0$ in larger pores, pore filling reduces the etch rates due to there being a larger effective polymer thickness. This is most significant at high porosities, large average pore radius and high interconnectivities.

Etch rates for high aspect ratio trenches showed dependencies similar to blanket etching. The profiles changed from tapered to bowed with increasing bias and decreasing Φ_n/Φ_{ion} values. The pore filling effect showed acute response to increasing neutral fluxes. Scaling laws for the taper of the profile for solid SiO_2 are applicable to PS as well. Pore radius and porosity have little effect on the taper of the profile. However the profile becomes bowed as the porous network becomes more interconnected. The pore filling effect on sidewalls, although has no immediate effect on the taper of the profile, is problematic during the later removal of the polymer and the filling of the pores.

4.6 Tables

Table 4.1: Total fluxes of the reactants to the center of the wafer

	Flux ($cm^{-2}s^{-1}$)		
Species	C_2F_6 [a)]	C_4F_8 [b)]	CHF_3 [a)]
CF_3^+	9.32×10^{15}	5.69×10^{15}	2.78×10^{15}
CF_2^+	1.45×10^{16}	1.34×10^{16}	5.70×10^{15}
F^+	2.88×10^{16}	2.63×10^{16}	1.39×10^{16}
F_2^+	3.16×10^{14}	6.04×10^{14}	6.34×10^{14}
$C_2F_4^+$	6.68×10^{13}	1.48×10^{15}	2.87×10^{11}
$C_2F_5^+$	1.85×10^{13}	1.41×10^{13}	7.41×10^{11}
CHF_2^+	-	-	1.59×10^{14}
H_2^+	-	-	1.17×10^{15}
H^+	-	-	8.42×10^{14}
CF_2	2.71×10^{16}	3.85×10^{17}	8.24×10^{15}
CF	2.07×10^{16}	3.26×10^{17}	5.48×10^{15}
F	5.35×10^{16}	5.77×10^{16}	1.56×10^{16}
H	-	-	1.15×10^{16}
C_2F_3	9.57×10^{11}	5.51×10^{15}	3.50×10^{09}
C_2F_4	4.66×10^{12}	2.15×10^{16}	3.91×10^{11}

a. 6 mTorr, 40 sccm, 1400 W ICP, -100 V self bias
b. 10 mTorr, 50 sccm, 1400 W ICP, -110 V self bias

4.7 Figures

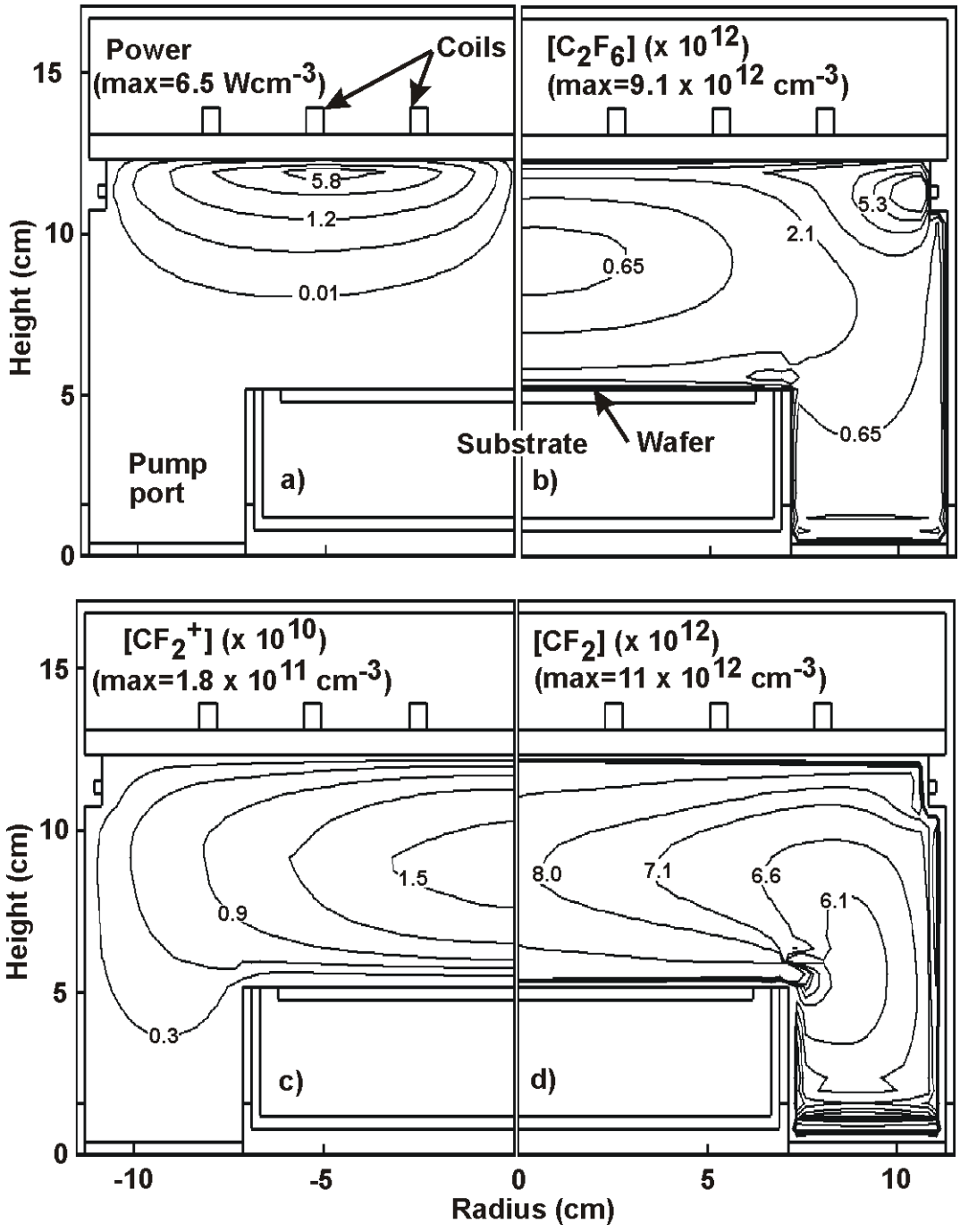

Fig. 4.1. Plasma properties for the base case (C_2F_6, 1400 W ICP power, 6 mTorr, 40 sccm) and -110 V self-bias. (a) Power, (b) C_2F_6 density, (c) CF_2^+ and (d) CF_2 density. Large power creates a dissociative plasma, which populates the smaller molecules.

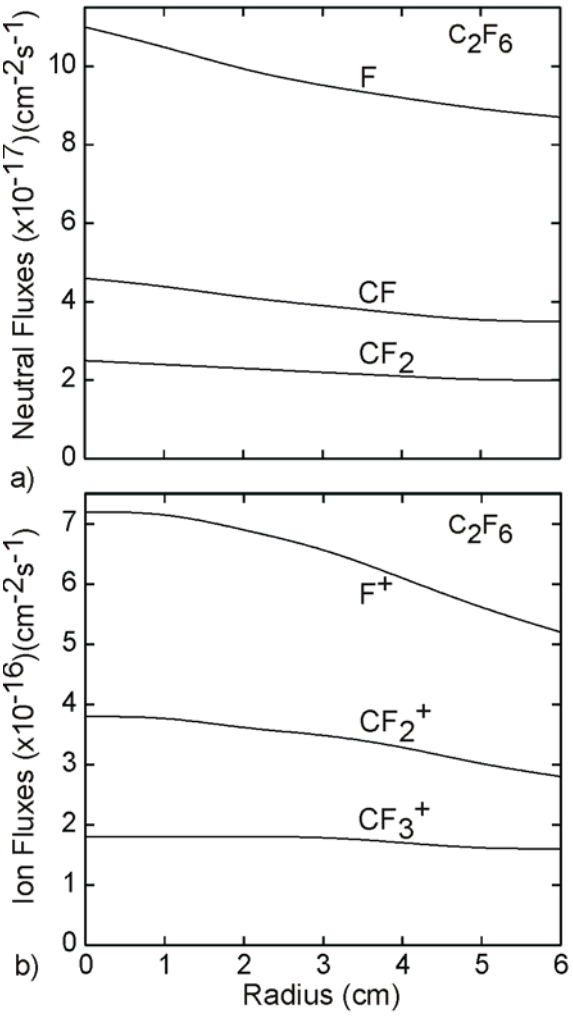

Fig. 4.2. Fluxes to the surface as a function of radius for the base case conditions for C_2F_6 plasma. (a) Fluxes of CF_2, CF and F. (b) Fluxes of F^+, CF_2^+ and CF_3^+. Decreasing polymerizing flux with radius is compensated by decreased physical sputtering and delivery of activation energy by the ions.

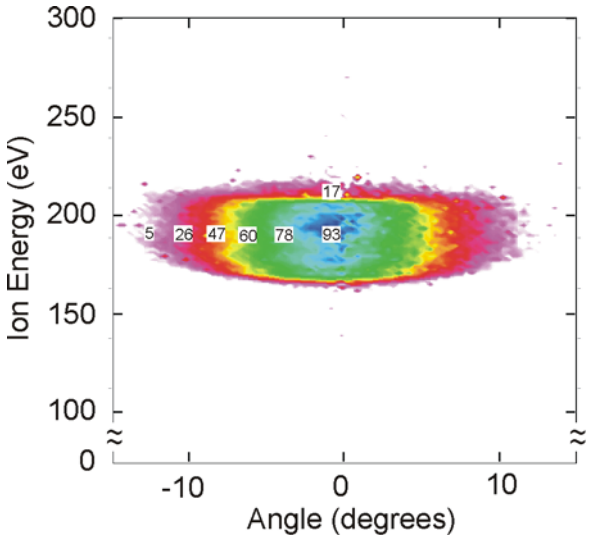

Fig. 4.3. Total ion angular and energy distributions incident on and averaged over the wafer for the base case conditions. Ion angular distributions indicate anisotropic fluxes to the wafer.

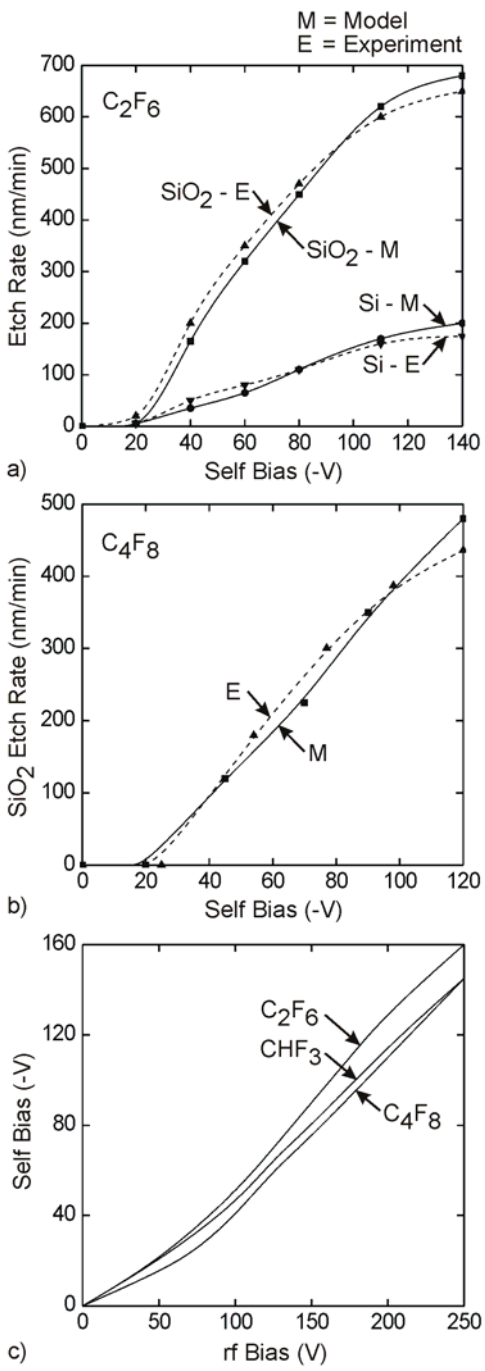

Fig. 4.4. A comparison of simulated and experimental results of SiO_2 and Si etch rates as a function of self-bias voltage for (a) C_2F_6 and (b) C_4F_8 plasmas. (c) Relation between the self generated dc bias and the applied rf bias for all gas chemistries. Etch rates increase with self-bias after a threshold bias and stagnates at high biases. Etch rates of Si are lower due to thicker polymer layers, which is the source of selectivity. Experimental results are from Ref. 1and 2.

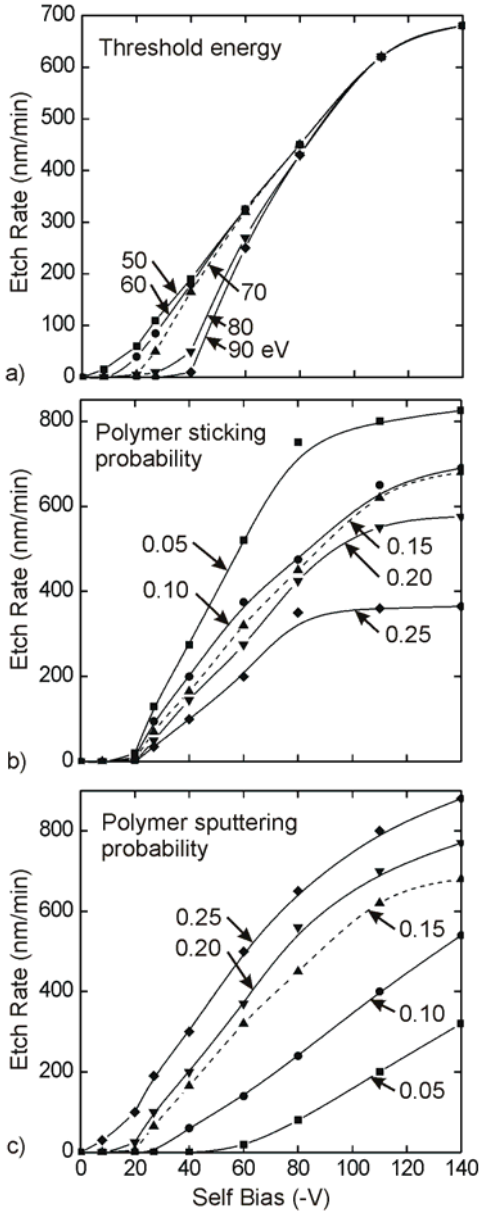

Fig. 4.5. Variation of ER of SiO_2 in C_2F_6 plasma with parameters in the reaction mechanism. (a) Threshold energy of ion activated processes, (b) fluorocarbon radical sticking probability and (c) polymer sputtering probability. The threshold in self-bias for onset of etching increased with the threshold of ion activated processes and decreasing polymer sputtering probability. Increase in polymer sticking decreased etch rates at high self-biases.

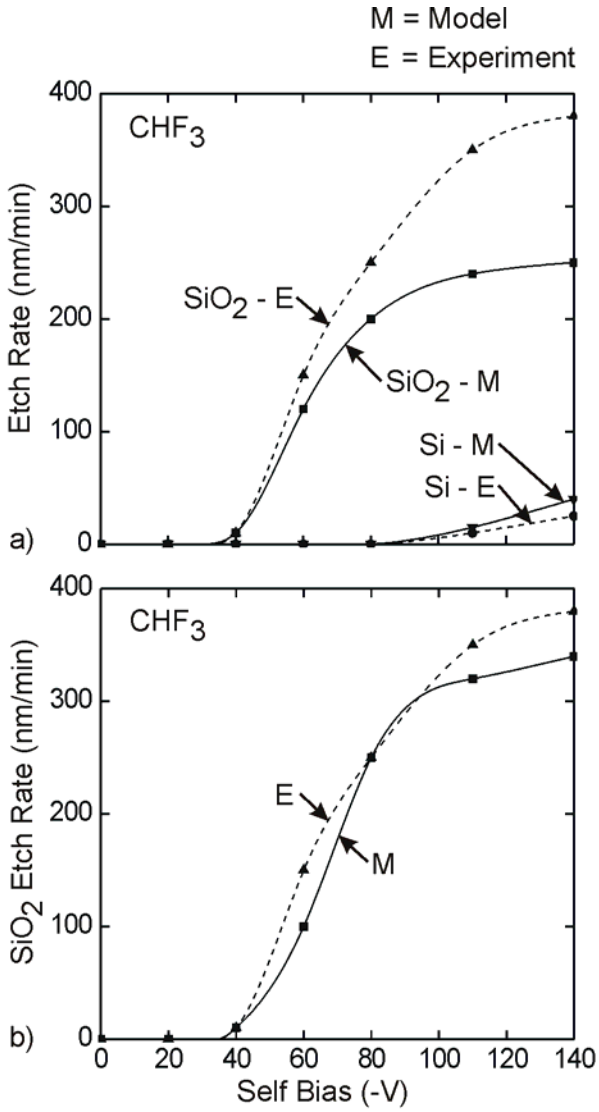

Fig. 4.6. A comparison of simulated and experimental results of SiO_2 and Si etch rates as a function of self-bias voltage for CHF_3 plasmas. (a) Etch rates before accounting for H radicals in the reaction mechanism. (b) Etch rates after accounting for H radicals in the reaction mechanism. H radicals cross link to the polymer and change the polymer composition, which are accounted for by modifying polymer sputtering rates. Experimental results are from Ref. 1.

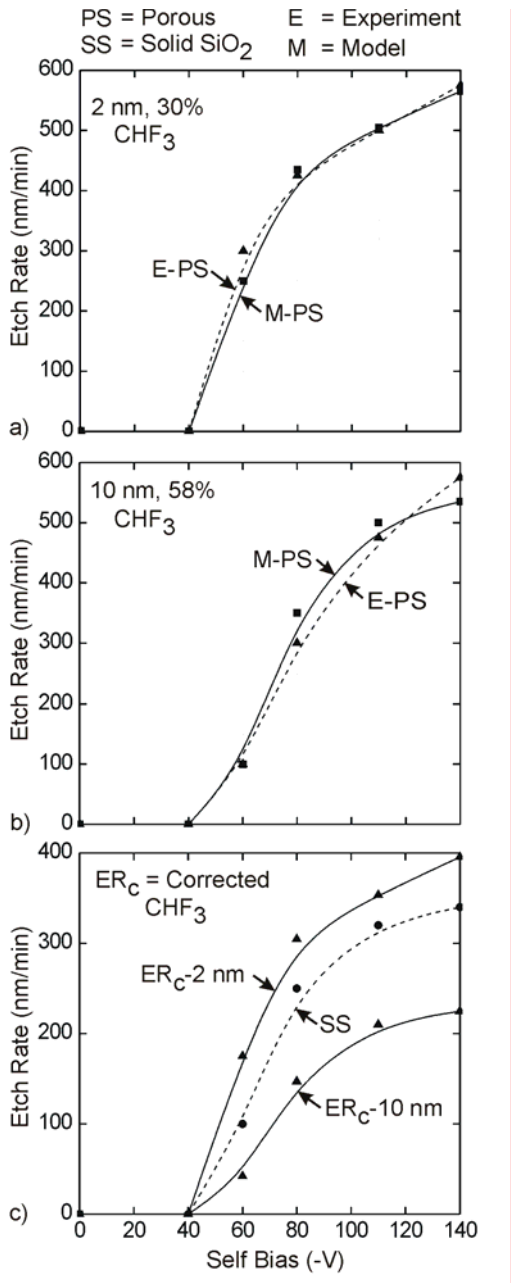

Fig. 4.7. SS and PS etch rates as a function of self-bias voltage for a CHF_3 plasma for the base case conditions. (a) PS with r_0 = 2 nm, 30% porosity, Δr = 1.2 nm. (b) r_0 = 10 nm pore, 58% porosity, Δr = 5 nm. (c) Corrected etch rates. Corrected etch rates are enhanced by small pores and depressed by large pores, which also depends on the steady state polymer thickness. Experimental results are from Ref. 2.

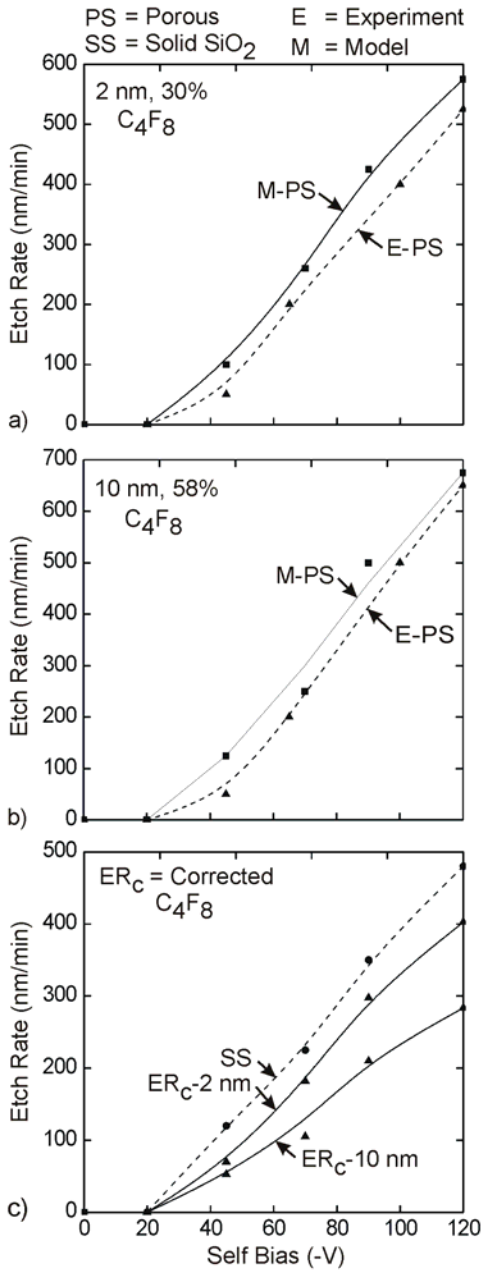

Fig. 4.8. SS and PS etch rates as a function of self-bias voltage for a C_4F_8 plasma for the base case conditions. (a) PS with r_0 = 2 nm, 30% porosity, Δr = 1.2 nm. (b) r_0 = 10 nm pore, 58% porosity, Δr = 5 nm. (c) corrected etch rates. Corrected etch rates are depressed by both small and large pores, due to a thinner steady state polymer thickness. Experimental results are from Ref. 2.

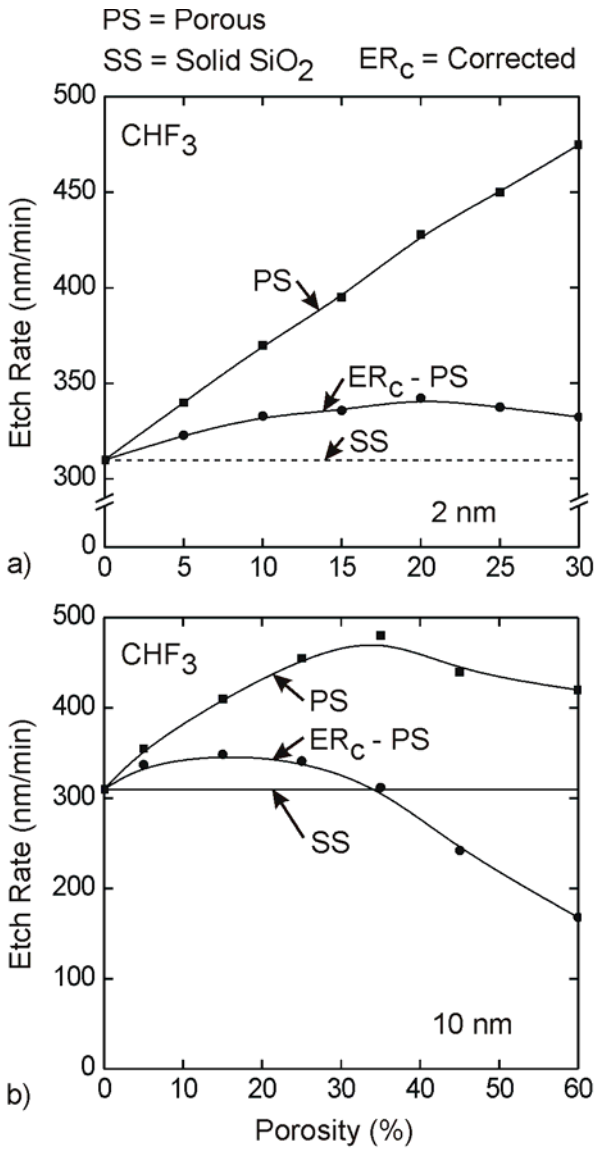

Fig. 4.9. SS and PS etch rates as a function of porosity for a CHF_3 plasma for the base case conditions. (a) PS with r_0 = 2 nm, 30% porosity, Δr = 1.2 nm. (b) r_0 = 10 nm pore, 58% porosity, Δr = 5 nm.. Etch rate enhancements for small pores are pronounced at higher porosities and pore filling is prominent for large pores at high porosities.

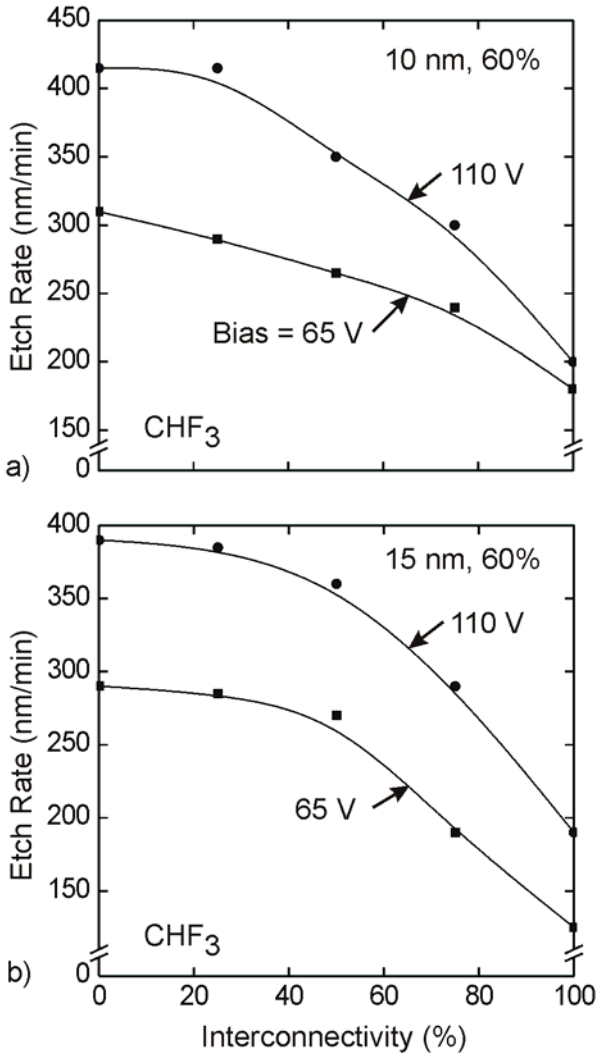

Fig. 4.10. SS and PS etch rates as a function of pore interconnectivity for a CHF_3 plasma for the base case conditions for two self-bias voltages. (a) PS with r_0 = 10 nm pores, 60% porosity, Δr = 5 nm. (b) r_0 = 15 nm pore, 60% porosity, Δr = 7.5 nm. Pore filling reduces etch rates at higher pore interconnectivities.

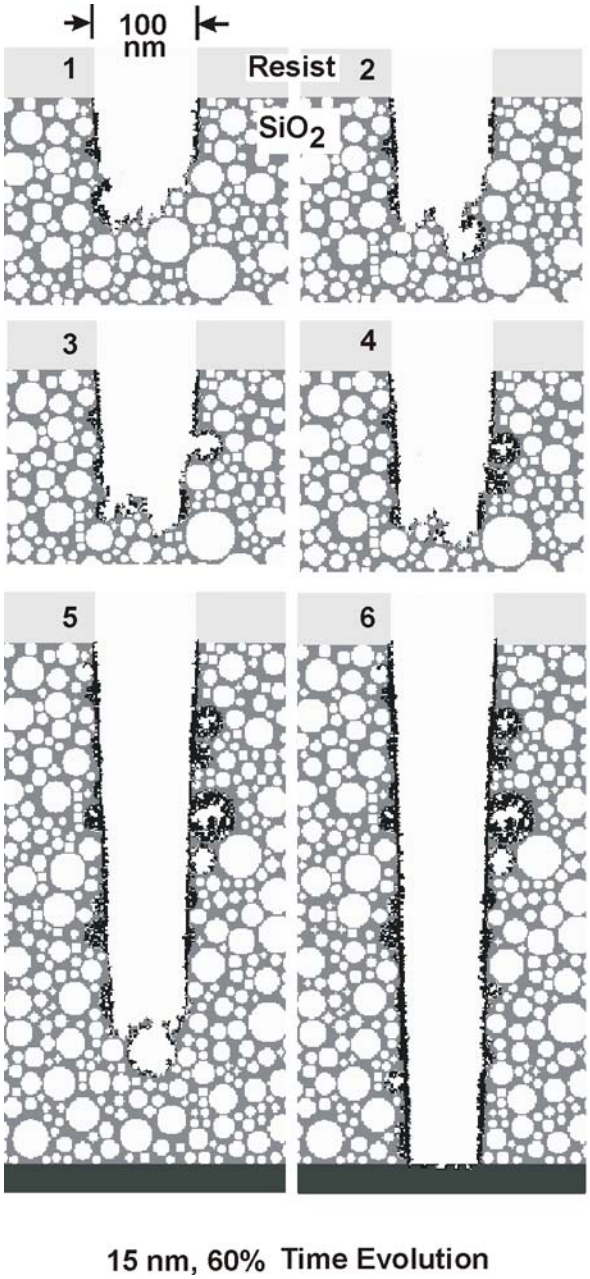

Fig. 4.11. A time sequence of etch profiles for PS having closed pore network with r_0 = 15 nm, 60 % porosity and Δr = 7.5 nm. The aspect ratio is 5. The black shading represents polymer. The sequence of profiles captures pore breakthrough, polymer filling in the vertical and lateral directions. Pore filling slows the etch process but has little effect on the taper in this case.

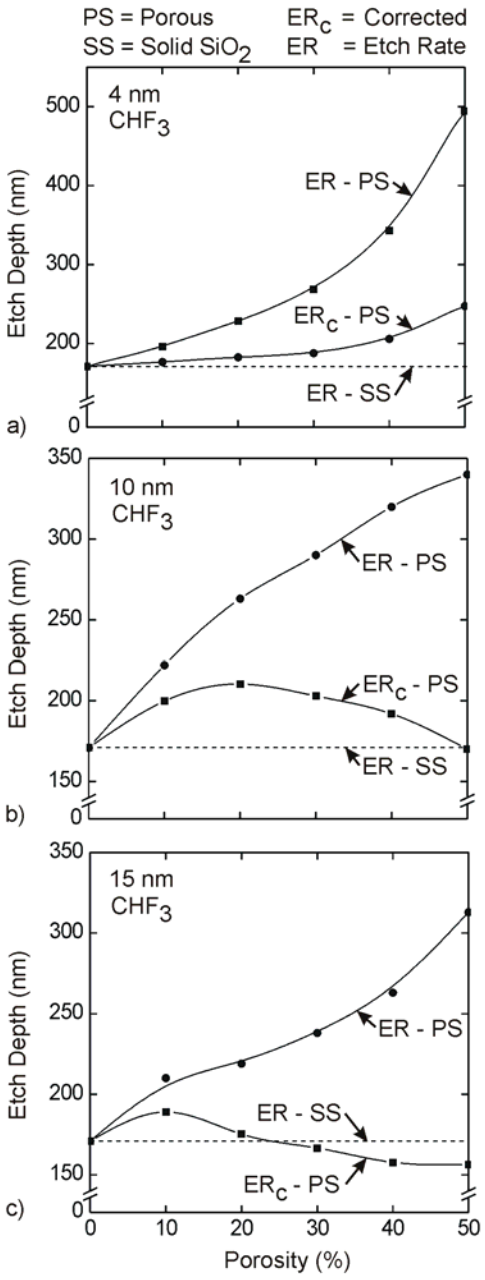

Fig. 4.12. Etch rates of PS as a function of porosity for etching of HAR vias in CHF_3 plasma for base case conditions for (a) r_0 = 4 nm, Δr = 2 nm, (b) r_0 = 10 nm, Δr = 5 nm and (c) r_0 = 15 nm, Δr = 7.5 nm. Pore filling depresses etch rates at progressively lower porosities as the average pore radius increases.

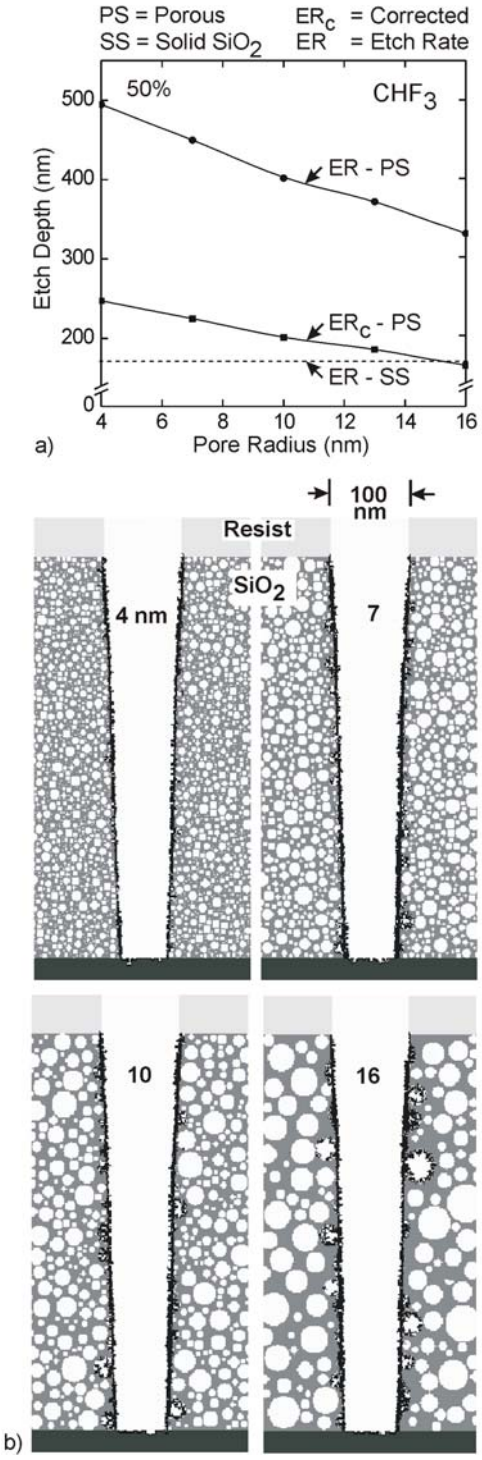

Fig. 4.13. Etch properties of 50 % porosity PS as a function of pore radius for etching of HAR features in CHF_3 plasma for base case conditions. (a) Etch rates. (b) Etch profiles. The etch rates and corrected etch rates decrease linearly with increasing pore radius. Profiles indicate little dependence of taper with pore radius.

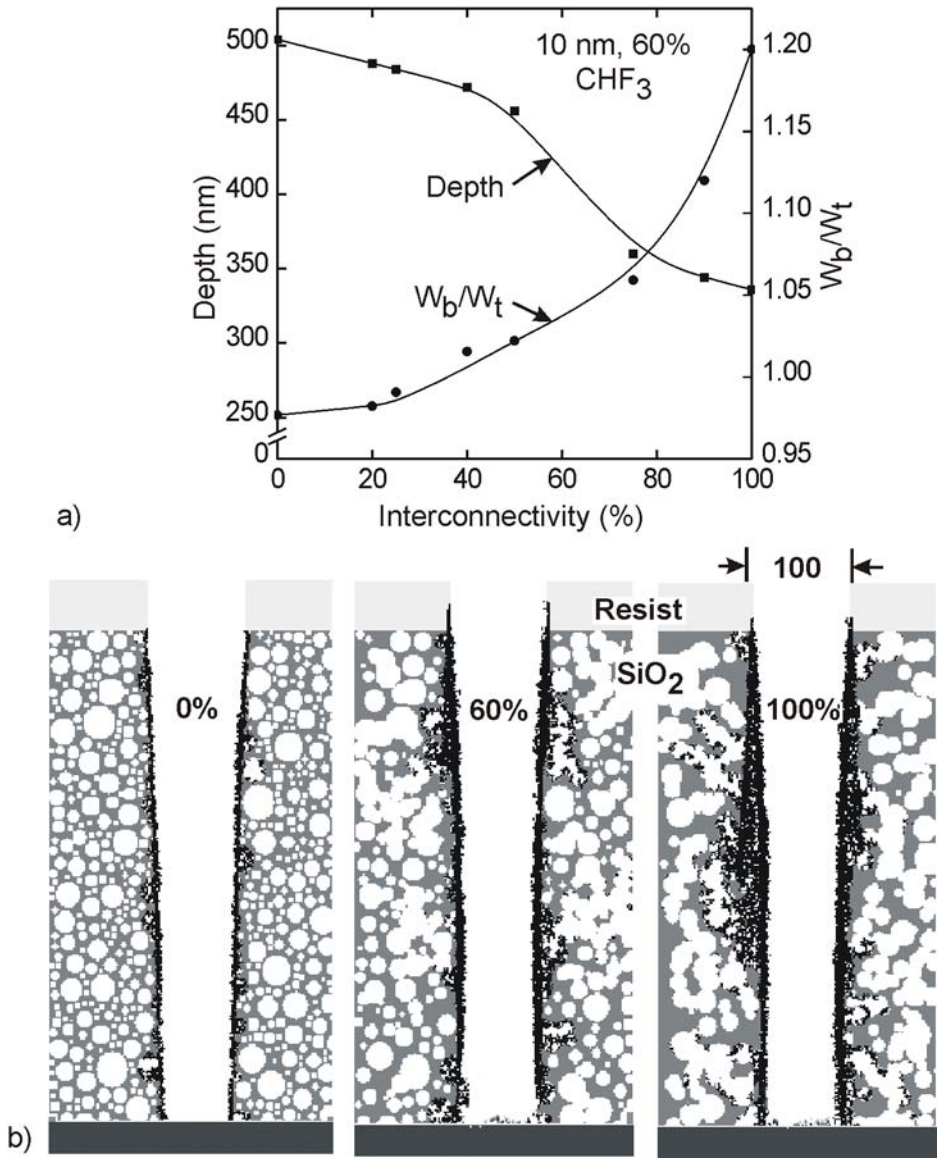

Fig. 4.14. Effect of interconnectivity on etch properties for etching of PS features with r_0 = 10 nm, 60% porosity in CHF_3 plasma for base case. (a) Etch rate and taper. (b) Etch profiles. Increasing interconnectivity decreases etch rates due to pore filling. Larger interconnectivities produce bowed profiles.

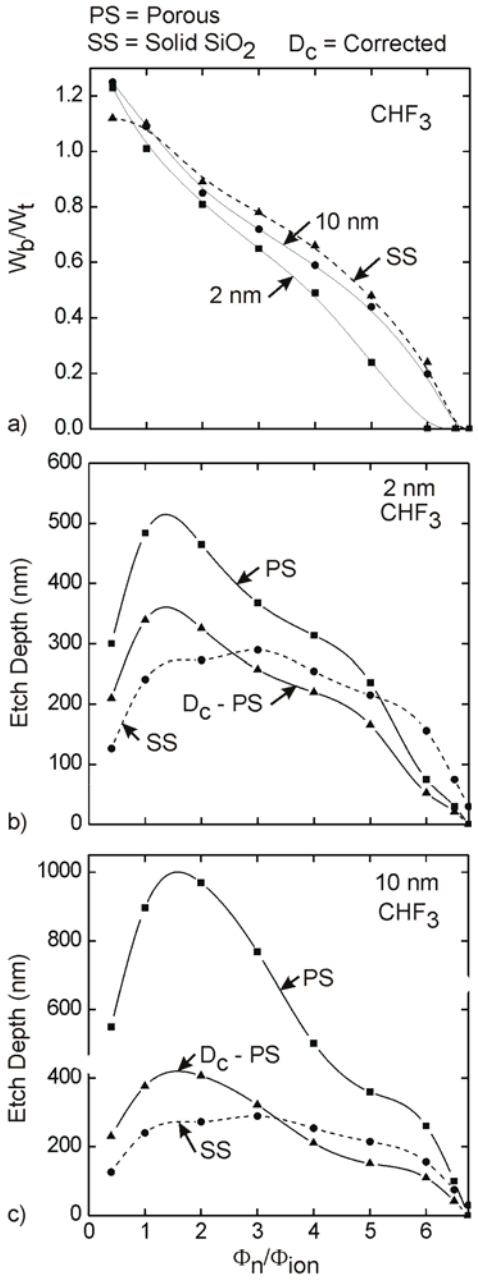

Fig. 4.15. Influence of passivating neutral to ion flux ratio Φ_n/Φ_{ion} on PS features etched in CHF_3 plasma for base case and self bias of -110 V. (a) Taper of the profiles for PS with r_0 = 2 nm, 30 % porosity and r_0 = 10 nm, 58% porosity. (b) ERs for PS with r_0 = 2 nm, 30 % porosity. (c) ERs for PS with r_0 = 10 nm, 58% porosity. Pore filling increases disproportionately with increasing Φ_n/Φ_{ion}, which slides the gross etch rate of PS below that of solid SiO_2.

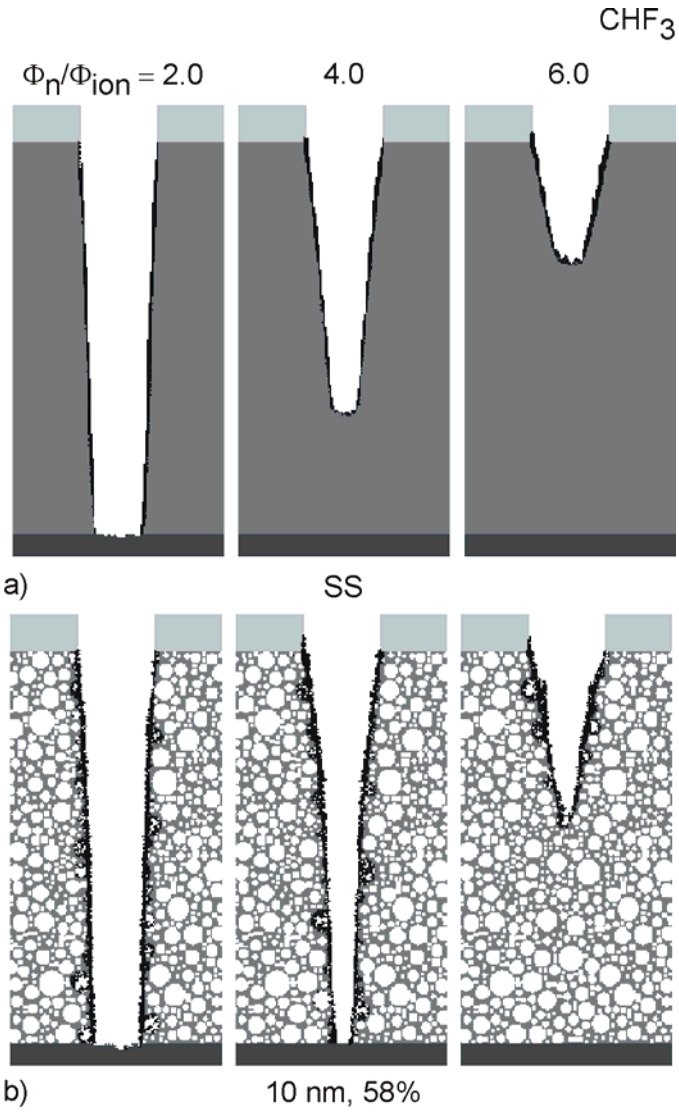

Fig. 4.16. Profiles of HAR trenches of SS and PS (r_0 = 10 nm, 60% porosity) etched in CHF_3 plasma for base case and self bias of -110 V as a function of Φ_n/Φ_{ion}. As Φ_n/Φ_{ion} increases, etch stop occurs at lower depths and taper increases for both SS and PS.

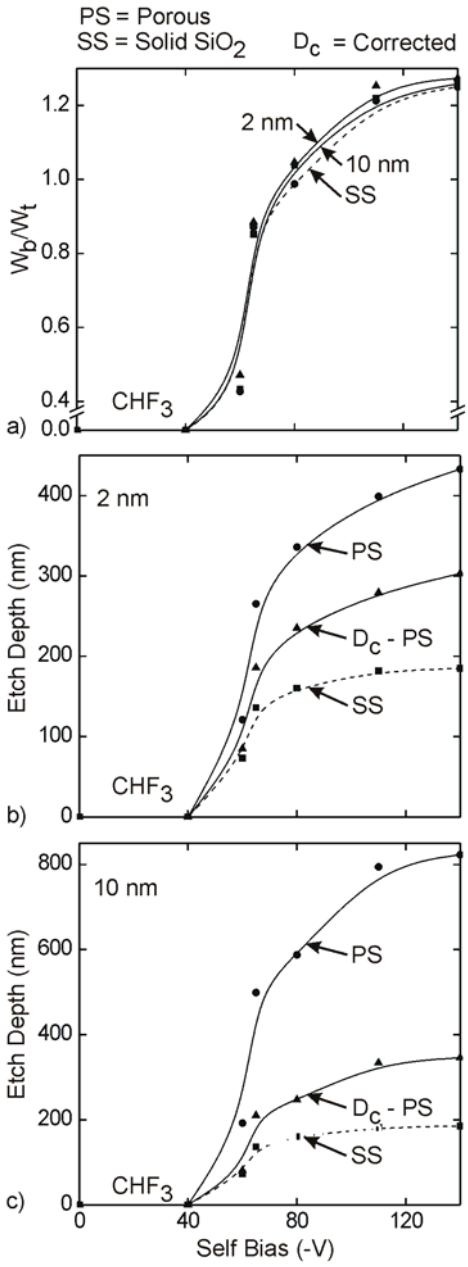

Fig. 4.17. Etch rates and taper of PS features etched in CHF_3 plasma as a function of self-bias for (a) taper of the profiles for PS with 2 nm pore radius, 30 % porosity and 10 nm pore radius, 58% porosity. (b) PS with 2 nm pore radius, 30% porosity. (c) 10 nm pore radius, 58% porosity for base case conditions. Increasing self-bias reduces pore filling by increased ion activation, thus enhancing etch rates.

4.8 References

[1] M. Schaepkens, T. E. F. M. Standaert, N. R. Rueger, P. G. M. Sebel, G. S. Oeherlein, and J. M. Cook, J. Vac. Sci. Technol. A **17,** 26 (1999).

[2] T. E. F. M. Standaert, E. A. Joseph, G. S. Oehrlein, A. Jain, W. N. Gill, P. C. J. Wayner, and J. L. Plawsky, J. Vac. Sci. Technol. A **18,** 2742 (2000).

[3] T. E. F. M. Standaert, P. J. Matsuo, S. D. Allen, G. S. Oehrlein, and T. J. Dalton, J. Vac. Sci. Technol. A **17,** 741 (1999).

5. RESIDUAL FLUOROCARBON STRIPPING AND Cu IMPVD ONTO POROUS AND NONPOROUS SiO_2

5.1 Introduction

The adoption of low dielectric constant (low-k) materials such as porous silica (PS) as interlayer dielectrics (ILD) in microelectronics fabrication depends on its process compatibility. Cleaning of residual polymer from trenches following etching and the deposition of a continuous barrier layer are critical processes for integration PS as ILDs. To investigate these issues, the surface reaction mechanism for etching of fluorocarbon polymer in O_2 plasmas, which was described in Section 3.3.2 has been incorporated into the two-phase MCFPM (described in Chapter. 3) and the results from this investigation is presented in this chapter. Validation of the surface reaction mechanism for etching of PTFE in Ar/O_2 chemistries by comparison to experiments is shown in Section 5.2.[1] Stripping of residual fluorocarbon from etched high aspect ratio (HAR) trenches of PS and SS using O_2 plasmas is discussed in Section 5.3. Copper IMPVD, developed earlier for studying trench filling in nonporous films, was then investigated for deposition on cleaned PS trenches as a surrogate to deposition of barrier coating or seed layer and is presented in Section 5.4.[2]

5.2 Validation of the Reaction Mechanism

The surface reaction mechanism for Ar/O_2 plasma etching of organic polymer described in Section 3.3.2 was validated by comparison to experiments done by Standaert *et al* for etching of PTFE.[1] The ICP reactor used for this study, shown in Fig. 5.1, is patterned after that used by Standaert *et al*.[3] ICP power is supplied through a 3-turn coil sitting on a 1.9 cm thick, 23 cm diameter quartz window at the top of the reactor. The quartz window is 19-mm-thick with a

diameter of 23 cm and the plasma is generated below this window. The process gases are injected into the reactor by a nozzle under the quartz window. The gas flow rate (40 sccm), pressure (4 mTorr) and ICP power (600 W at 13.56 MHz) were held constant. The 125 mm wafer is on a substrate 7 cm below the quartz window and is maintained at 10° C for all simulations. The substrate is independently biased at 3.4 MHz to produce directional ions to the wafer.

Spatial densities of Ar^+ and O radicals are shown in Fig. 5.1. The feed gas is Ar/O_2 = 94/6 and the rf bias is 40 V at 3.4 MHz. The power deposition and dominant ionization is confined to 2–3 cm below the coils and the transport of electrons and ions are primarily governed by ambipolar diffusion. Hence the Ar^+ density peaks at the center of the reactor. The O radical density, is also high near the nozzle as O radicals are the product of electron impact dissociation of the O_2 feed gas.

Fluxes of Ar^+, O_2^+, O^+ and O to the wafer as a function of radius for the same process conditions are shown in Fig. 5.2(a). The dominant ion for these process conditions is Ar^+. Fluxes of Ar^+ and O atoms, which are the key precursors in the etch kinetics, decrease moderately with radius resulting in less activation and lower sputtering at the edge of the wafer. For these conditions etch rates for blanket etching of PTFE at the edge of the wafer were ≈20% lower than at the center. The energy and angular dependence of the Ar^+ flux, shown in Fig. 5.2(b) has an average energy of ≈75 eV and angular spread of 10°.

Total ion and O fluxes to the center of the wafer for different Ar/O_2 ratios as a function of the applied rf bias are shown in Fig. 5.3. Increasing the O_2 mole fraction results in a corresponding increase in the flux of O and decrease in the ion fluxes. O radical fluxes are not sensitive to changes in the applied rf bias. However, ion fluxes increase ≈10% when rf bias is

increased to 80 V. Bias power as a function of applied rf bias voltage and gas mixture is shown in Fig. 5.3(c). With increasing Ar fraction, there is an increase in the total ion flux to the wafer, which increases current and power deposition for a given rf bias.

Etch rates as a function of bias power for blanket etching of PTFE in Ar/O_2 mixtures are shown and compared to experiments in Fig. 5.4.[1] For a given gas mixture, the O atom flux is nearly independent of bias power, and so the rate of formation of P* is constant. The increase in etch rates with increasing bias power is attributed to an increase in the sputtering of P* which releases volatile etch products such as CO_x, COF_x and F_2. At zero bias, increases in the etch rate with increasing O_2 is only nominal which indicates that the sputtering of P* is the rate-limiting step at low biases. In contrast, at 100 W bias power, increasing the O_2 content from 6% to 25% increases the etch rates from 3500 nm/min to 4500 nm/min. At these bias powers oxidation of the polymer surface to form P* becomes the rate-limiting step. These results are also consistent with earlier observations that oxygen plasma etching of organic polymer has distinct oxygen-neutral limited regime and ion-limited regime.[4]

The sensitivity of polymer etch rates on coefficients describing formation (Eq. 3.13) and sputtering of P* (Eq. 3.14) was investigated. For example, etch rates as a function of O atom sticking probability to form P* for the base case conditions and $Ar/O_2 = 94/6$ are shown in Fig. 5.5. Without a bias, etching is limited by the sputtering rates. As a result increasing p_0 has little effect on etching. As the substrate bias increases, ion energies increase sufficiently to sputter P* and facilitate product formation and thereby exposing more polymer surface to further oxidation. As a result, etch rates increase with p_0 at intermediate biases. However further increasing the bias increases the rate of direct sputtering by ions, which then becomes the dominant polymer removal process. Hence the variation of etch rate as a function of p_0 is minimal at large biases.

Based on these observations, and similar parameterizations for other gas mixtures and comparisons to experiments, we chose $p_0 = 0.50$.

The sensitivity of sputtering of P* was also investigated for the same process conditions. The resulting etch rates are also shown in Fig. 5.5. Since at low rf bias, ion sputtering is rate limiting, decreasing E_{th} significantly increases the fraction of ions that are able to sputter P*. At zero substrate bias etch rates increase from ≈400 to 2000 nm/min when E_{th} is decreased from 45 to 15 eV. Etch stop occurs for $E_{th} \geq 45$ eV. High biases are in the neutral-limited regime and as a result changes in E_{th} has little effect on the etch rates. Increasing p_0 increases etch rates for all substrate biases. Based on these parameterizations and comparison to experiments we chose E_{th} = 45 eV and $p_0 = 0.03$.

5.3 Stripping of Residual Fluorocarbon Polymer

Stripping of residual polymer from vias and trenches of SiO_2 etched in fluorocarbon plasmas has become increasingly challenging with the reduction in feature sizes and increase in the aspect ratio of the features. Use of O_2 plasmas for this purpose; although common practice for SS films, has yet to be optimized for PS films due to their complex pore morphologies and their more complex interactions with the plasma species.

The ICP reactor that was used for the etching of the SS and PS trenches is the same as that used for the stripping applications. Profiles of HAR SS trenches before and after stripping are shown in Fig. 5.6. The etching process conditions are 1400 W ICP power at 13.56 MHz, 6 mTorr pressure, 40 sccm CHF_3 flow rate and substrate bias of -65 V. These process conditions were optimized to obtain a profile with nearly vertical sidewalls. The aspect ratio of the profile is 5 with a top opening of 100 nm. The taper of the profile calculated as the ratio of the width of

the trench at 400 nms from the bottom to the width at the top of the trench is 0.98. The stripping process conditions are the base case with Ar/O_2 = 99/1 and bias = 20V. The post etch residual polymer thickness on the sidewalls for this case is ≈5 nm and on the bottom of the trench is a few monolayers. This difference is a result of there being less ion sputtering of the passivation layer on the sidewalls of the profiles during etching due to the high degree of anisotropy of ions. In contrast the directional ions are more efficient in delivering activation energy to the bottom of the trench and hence reduce the thickness on the bottom of the trench. The stripping process is optimal for SS trenches, where complete stripping is achieved. For the time scales required to achieve complete cleaning of the residual fluorocarbon polymer, there is little resist erosion as the resist thickness are comparatively larger and the threshold energies for ion assisted processes for resist etching are larger than that for fluorocarbon polymer etching. Therefore, we have not discussed resist erosion in this chapter. Resist erosion is discussed in Chapter 7.

Stripping efficiency (the fraction of polymer remaining) for the same conditions using Ar/O_2 = 99/1 while varying substrate biases is shown in Fig. 5.6(b) as a function of time. As in blanket etching, at low biases there are low rates of sputtering of P*. The removal of polymer sites to produce volatile etch products is the rate limiting step. As the bias increases there is increased production of etch products due to both chemically enhanced and direct sputtering. Note that the cleaning times are short as only 5-10 nm of material need to be removed from the sidewalls. The time is short compared to that required to remove the much thicker photoresist.

The stripping of residual fluorocarbon from PS having closed pores and 50% porosity and different average pore radii is shown in Fig. 5.7. The process conditions are the base case, Ar/O_2 = 99/1 and an rf bias of 20 V at 3.4 MHz. Results are shown for a time corresponding to removing 99% of the polymer for the 4 nm pore case. Stripping efficiencies generally decrease

with increasing average pore radius. The non-monotonic change in efficiency (at a given time) between, for example, 10 and 13 nm pore cases results from the stochastic nature of the pore morphology and view angles to the plasma. When PS with 4 nm pores are completely cleaned of polymer nearly 24% of the residual polymer remains for the 16 nm case. The cleaning is more effective at the top of the trench than the bottom of the trench due to the lack of view angles for the incident ions. This is particularly so for the inner surfaces of pores. There is significant polymer left on the inner surfaces of the pore. These locations at best receive hot neutrals from ion reflection which have lower energies. This results in poor ion sputtering and removal of the polymer. On the other hand, the formation of polymer at these sites during fluorocarbon etching results from low ion energy activation and is more dependent on the neutral fluxes. The neutral flux being more isotropic in nature is less sensitive to the pore morphology.

The inefficiencies in stripping due to the complex pore morphology which occur in a closed pore network are magnified by interconnected networks. For example, profiles of HAR trenches in interconnected PS films after cleaning using an Ar/O_2 = 75/25 plasma for the base case conditions and rf bias of 20 V are shown in Fig. 5.8. The cleaning time is 10 s (same scale as for Fig. 5.7) which removes 99% of the polymer from a 4 nm closed pore network in an Ar/O_2 = 99/1 plasma. View angles for ions inside the interconnected chains become even more unfavorable and so the activated polymer surface sites in the interconnected chains are less likely to receive particle fluxes with sufficient energies to remove material. The end result is that residual polymer remains deep within the interconnected pores. With interconnected structures there is also the likelihood for O radicals to penetrate into the porous network, which could change the dielectric properties of the film by reacting with organic groups.

The stripping efficiency of residual fluorocarbon from PS with pore size of 16 nm and 50% porosity as a function of time for different interconnectivities are shown in Fig. 5.9 for Ar/O_2 = 75/25 and substrate rf biases of 20 and 80 V. With a closed pore network, increasing the substrate bias compensates for unfavorable view angles and achieves virtually complete polymer removal by increasing the energy of reflected neutrals into open pores. In contrast a 20 V bias is only able to remove 65% and 27% of the polymer from the 60% and 100% interconnected samples. For a 100% interconnected structure increasing the bias to 80 V reduces the asymptotic residual polymer fraction to 0.2. Even higher substrate biases would be required to deliver the required energy inside the pore chains for complete cleaning of the residues. The downside to this would be sputtering damage to the PS film.

Stripping was investigated for SS and PS trenches having different aspect ratios (AR). These stripping efficiencies are shown in Fig. 5.10 for an Ar/O_2 = 99/1 and rf bias = 20 V. Profiles for the 16 nm case, for ARs of 1, 3 and 5 are shown in Fig. 5.11. The time for cleaning was chosen such that 99% of the polymer was removed for SS trenches with AR = 4. The general trend is more rapid polymer removal for lower AR features. For a given AR, cleaning is less rapid as pore sizes increases. The scaling with AR is in part due to being in a reactant limited regime. The magnitude of the reactant current is determined by the width of the trench. As the AR increases a larger surface area is cleaned by a constant current of reactants and so on this basis alone the cleaning time should increase in proportion to the fractional increase in surface area. Additional increases in cleaning time are due to nonlinear processes.

For low AR trenches the pore morphology has little effect on the cleaning times. The views angle to the plasma from all surfaces is sufficiently large, or the shadowing sufficiently small, that energetic particles (direct or reflected) can reach into pores to sputter polymer.

Having said that, polymer stripping also depends on the location in the trench. For example, for AR = 3, pores near the top of the trench have large view angles to ions and so are left with residual fluorocarbon. Pores at the bottom of the trench also have little residual fluorocarbon as they receive energetic particles resulting from ions reflecting from the bottom of the trench. Pores located in the middle of the trench see fewer ions impacting directly or following reflection and so considerable residual polymer is left. The overall cleaning efficiency for the AR = 3 feature is ≈10% and which is mostly attributable to this middle region. For AR = 5, the cleaning efficiencies for the top 100 nm, middle 300 nm and the bottom 100 nm of the trench are 3%, 30% and 40% respectively. The overall cleaning efficiency in this case is 33%. As the aspect ratio increases, the view angles at the bottom of the trench decrease and the ions reflected from the bottom of the trench contribute less towards the stripping process.

5.4 Trench Filling by Cu IMPVD

Barrier coatings and seed layers of metals are typically deposited by PVD or IMPVD. Although Cu is not used for barrier coatings, we are using Cu IMPVD as a surrogate for these studies as the knowledge base for that system is well established. The reactor used for this study has been extensively discussed earlier and is briefly explained here.[5] A schematic of the reactor is shown in Fig. 5.12. The diameters of the target and the induction coils are both 20 cm. The diameter of the substrate is 21 cm. The distance between the target and the substrate is 13 cm. The process conditions are 1000 W ICP power, 300 W magnetron power, 40 mTorr Ar gas buffer and 150 sccm gas flow rate. The magnetic field is 250 G. The rf voltage on the inductive coil is 100 V and the self generated dc bias is -90 V. The rf and dc bias combination results in about 20 V of rf oscillation in the plasma potential. Fluxes of selected radicals and neutrals

incident on the wafer are shown in Fig. 5.12(b). Due to a high pressure of 40 mTorr the majority of the incident flux is Cu^+. The majority of the neutral Cu flux to the wafer consists of Cu* (metastable). Cu^+ has an ion energy distribution between 40 to 80 eV, which is primarily due to the oscillation in the plasma potential. Cu^+ flux is dominantly anisotropic and has an angular spread of -15° to 15° from the normal. In contrast the Cu* has energies between 0.1 to 0.7 eV and an isotropic angular distribution varying between 0° and 90°.

Barrier layers for atomically smooth ideal SS via and etched SS via are shown in Fig. 5.12. When the SS surface is atomically smooth, the resulting film is conformal with similar sidewall and bottom coverage as shown in Fig. 5.12 as well. When the SS surface is initially atomically smooth, the resulting film is conformal with similar sidewall and bottom coverage as shown in Fig. 5.12(c). Even in this case there is some small amount of roughness in the final Cu barrier layer due to sputtering of the SiO_2 sidewalls and Si bottom layer during the IMPVD process. This surface roughness is then magnified during the deposition process which has a directional component. When the initial surface has roughness, as in Fig. 5.12(d), the resulting film has significant thickness variation. The roughness here results from sputtering during the etch and cleaning processes and is magnified by the finite size of our numerical mesh. Nevertheless it is illustrative of the consequences of sidewall roughness, which by micro shadowing produces unevenness in the film. The direct result is that thicker films are required to insure that no pinholes or critically thin regions occur.

This need for thicker average films to mask roughness extends to PS. Barrier layers for SS and closed PS (4, 10 and 16 nm at 50% porosity) are shown in Fig. 5.13. The process conditions were optimized to achieve conformal coating for the SS film. The coating times are different for the different materials to achieve similar thickness. The film thickness on the

sidewalls for the different substrates is typically ≈3-5 nm. For 4 nm PS, the ratio of the film thickness on the top surface to the sidewalls (R) required for achieving conformal coverage is ≈3, which is larger than that required for SS, ≈2. This ratio increases to ≈6 for 10 nm PS. For 16 nm PS conformal coverage could not be achieved even when at ratios >6. In this case the pores are sufficiently large that species fluxes are inefficient in tracing the complex morphology of the pore and producing conformal coverage. The alternative would be to bridge the gap at the pore openings, which would require barrier coating thickness of at least the pore diameter.

Similar challenges are faced with interconnected porous networks, where the goal is to seal the opening to the interconnect chains by the diffusion barrier. Conformal coating into pores is sufficient for a good diffusion barrier for closed pores. However for interconnected pores it is not possible for the species flux to map onto the contours of the interconnect chains to achieve conformal coating and instead sealing or bridging is required. To characterize the efficiency of the barrier coating onto interconnected pores, deposition onto vias of 12 nm, 50% and 4 nm, 40% PS films for different interconnectivities were investigated and the results are shown in Fig. 5.14 and 5.15. The thickness of the coating on the sidewalls is ≈5-8 nm for all films. To bridge pores, coating thickness of at least the average pore diameter is required on the sidewalls. This is not feasible with the 12 nm PS, where there is narrowing of the trench opening for increased coating times. This reduces the view angles of the species fluxes and further decreases the efficiency of deposition inside the trench. Eventually this could lead to pinch-off. Due to the smaller pore diameter, 4nm PS film is more effectively sealed than 12 nm PS. R ≈5-6 is sufficient to effectively seal the interconnective paths. Unabridged pores in the case of the 60% and 100% interconnected 4 nm PS trenches are an artifact of the pore size distribution, which leads to larger gaps than the average pore diameter.

5.5 Concluding Remarks

Stripping of residual fluorocarbon from etched vias of PS and SS have been investigated using a surface reaction mechanism for etching of organic polymer in Ar/O_2 chemistries, which has been incorporated into a feature scale model coupled to a reactor scale model. Etching of organic polymer was ion-assisted with low etch rates in pure oxygen chemistries. Stripping efficiencies were higher in SS than PS and decreased with increasing aspect ratios of the feature. Stripping was less efficient in PS with larger average pore radius due to unfavorable view angles for the incident ion fluxes because of the complex pore morphology. For interconnected PS and larger pores, even when the cleaning process was extended to asymptotic limits, the stripping was incomplete. Complex pore morphologies are easily filled with polymer but the cleaning of PS using traditional dry etching techniques is less efficient. Trench filling by Cu IMPVD was investigated as a surrogate to barrier coating and seed layer deposition. Deposition was less conformal in PS with closed pores. With interconnected PS network, thicker films were required to avoid formation of pin holes. Thicker films also lead to pinch-off during the deposition process.

5.6 Figures

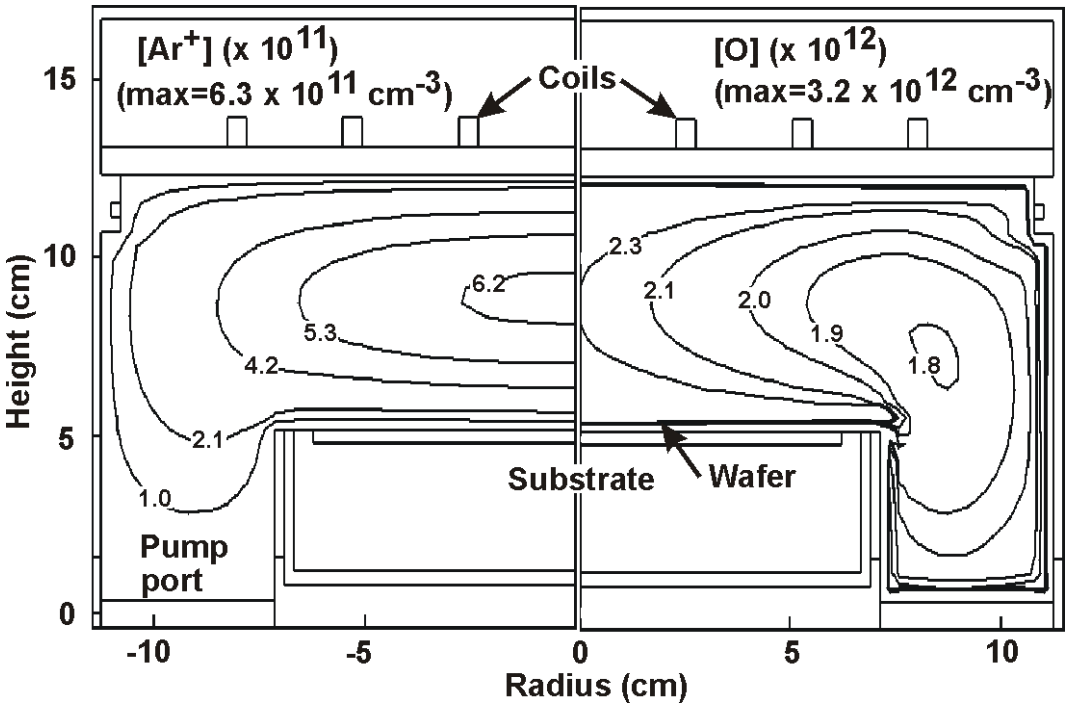

Fig. 5.1. Plasma properties of an Ar/O_2 = 94/6 plasma for the base case (600 W ICP power, 4 mTorr, 40 sccm) and 40 V rf bias at 3.4 MHz). (a) Ar^+ and (b) CF_2 density. As diffusive transport dominates at low pressures, the densities peak near the center

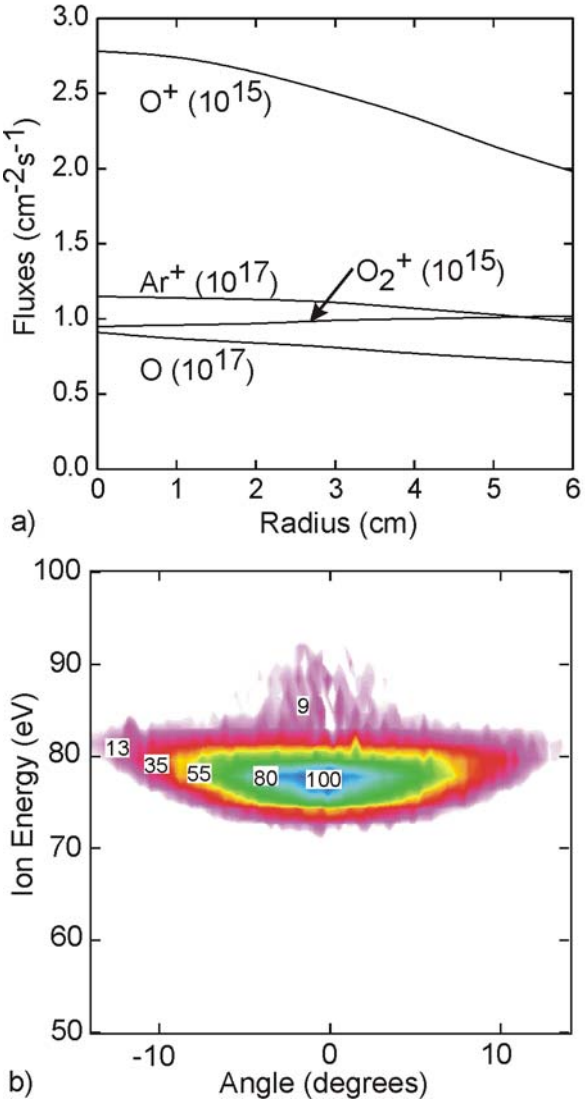

Fig. 5.2. Properties of the fluxes to the surface for the base case conditions for Ar/O_2 = 94/6 and 40 V bias (a) Ar^+, O_2^+, O^+ and O radical flux as a function of radius. (b) Ar^+ angular and energy distributions incident on and averaged over the wafer. Ion angular distributions indicate anisotropic fluxes to the wafer.

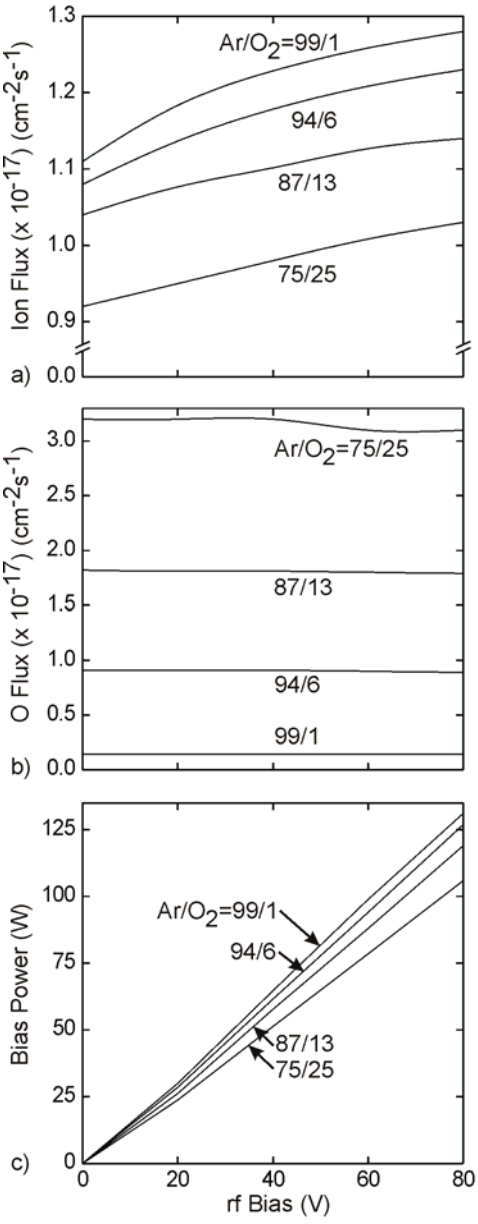

Fig. 5.3. Plasma properties as a function of gas composition and bias on the substrate for the base case conditions. (a) O flux to the center of the wafer (b) Ar^+ flux and (c) Bias power. Increased Ar^+ flux at higher Ar content in the gas mixture leads to larger substrate powers.

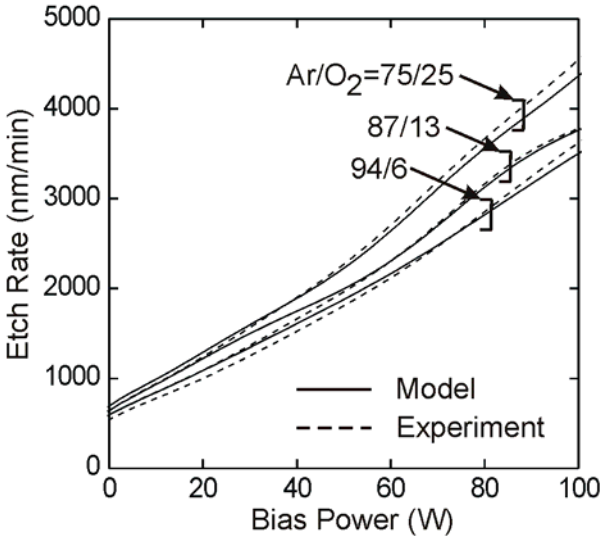

Fig. 5.4. A comparison of simulated and experimental results of PTFE etch rates as a function of bias power for Ar/O_2 chemistries. Etch rates are directly proportional to the bias power. Experimental results are from Ref. 1.

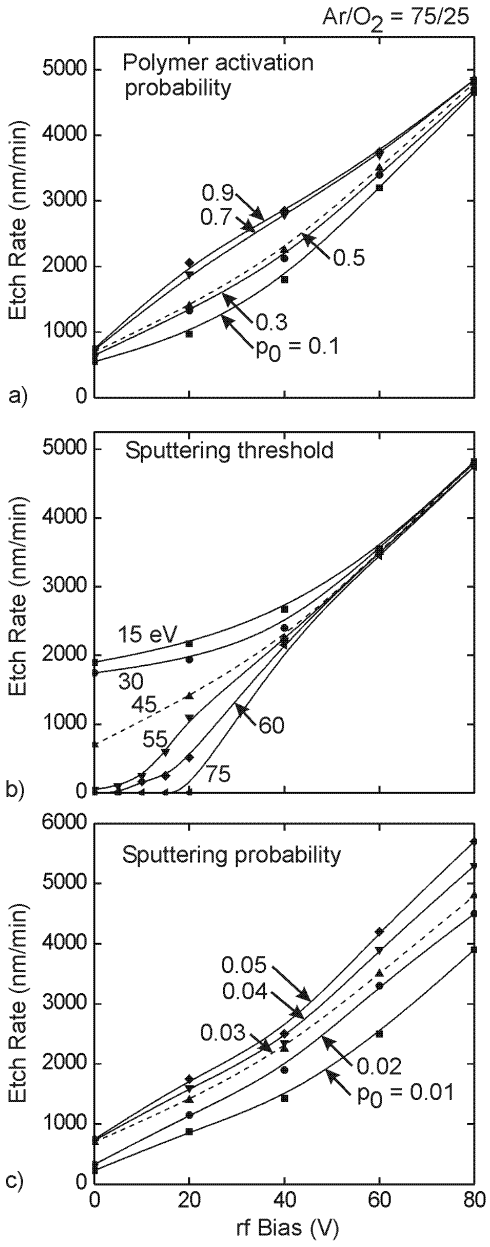

Fig. 5.5. Calibration of the parameters in the reaction mechanism for the base case conditions. (a) Probability of formation of activated polymer site. (b) Threshold energy of the sputtering of activated polymer site and (c) Sputtering probability of the activated polymer site. The polymer etching process shows an oxygen limited regime and a ion-energy limited regime.

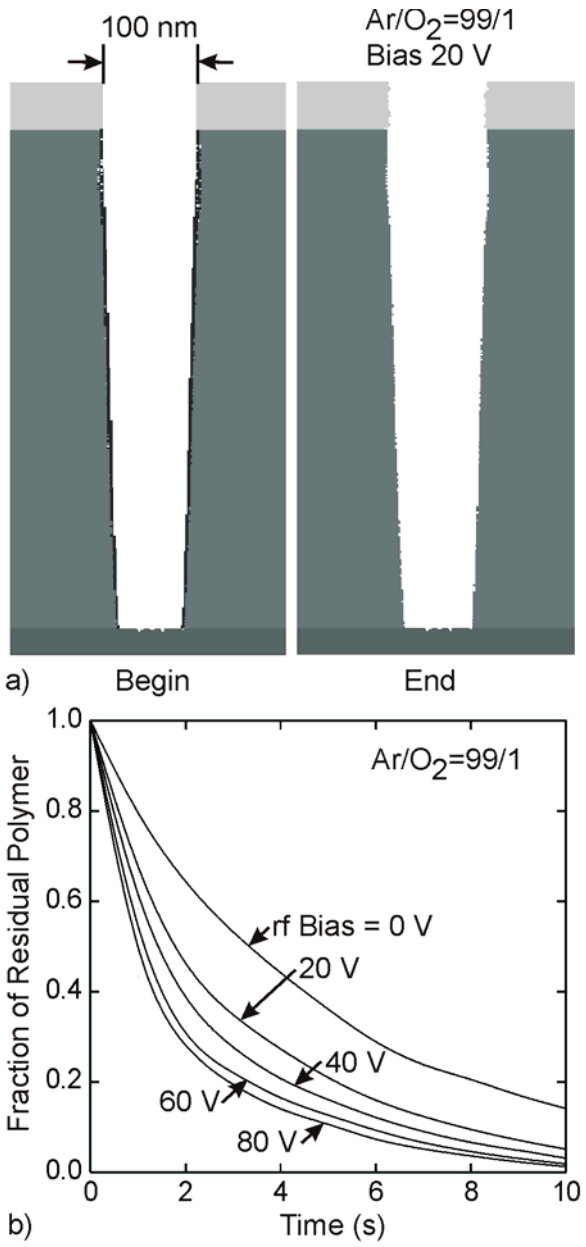

Fig. 5.6. (a) Profiles of SS via before and after the cleaning process using Ar/O_2 = 99/1, 20 V bias and base case conditions. The aspect ratio is 5 and the trench opening is 100 nm. (b) Stripping efficiency as a function of bias for a SS via cleaned using the same process conditions. As in blanket etching of PTFE, stripping is more efficient at higher biases due to larger effective sputtering of P*.

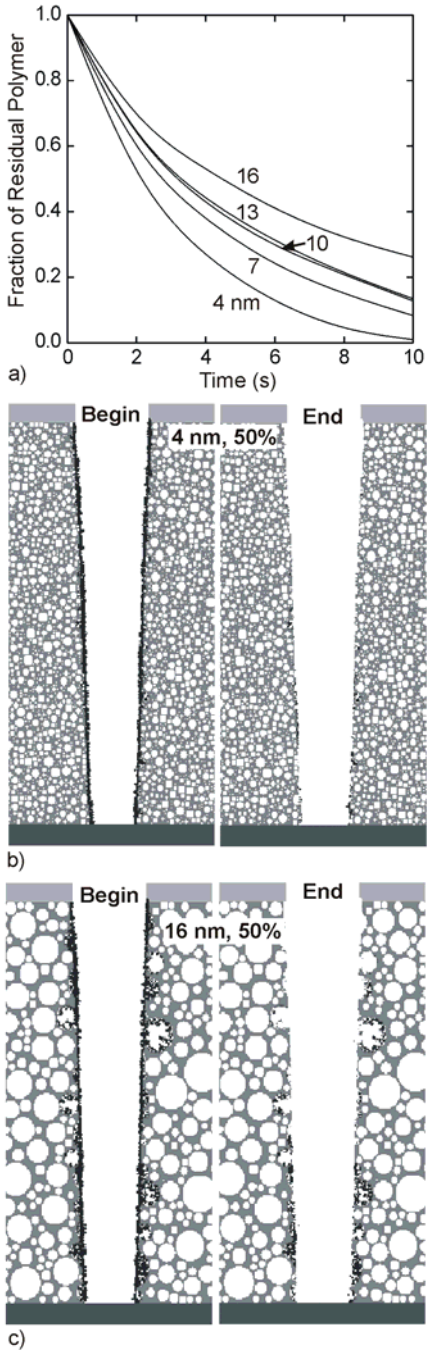

Fig. 5.7. (a) Stripping efficiency as a function of r_0 of PS thin films with closed pores and 50% porosity using Ar/O_2 = 99/1 for the base case conditions and 20 V bias. Profiles of the vias before and after the stripping process for the same process conditions for PS with (b) r_0 = 4 nm and (c) r_0 = 16 nm. Unfavorable view angles due to complex pore morphologies in case of PS with larger pores leads to inefficient stripping.

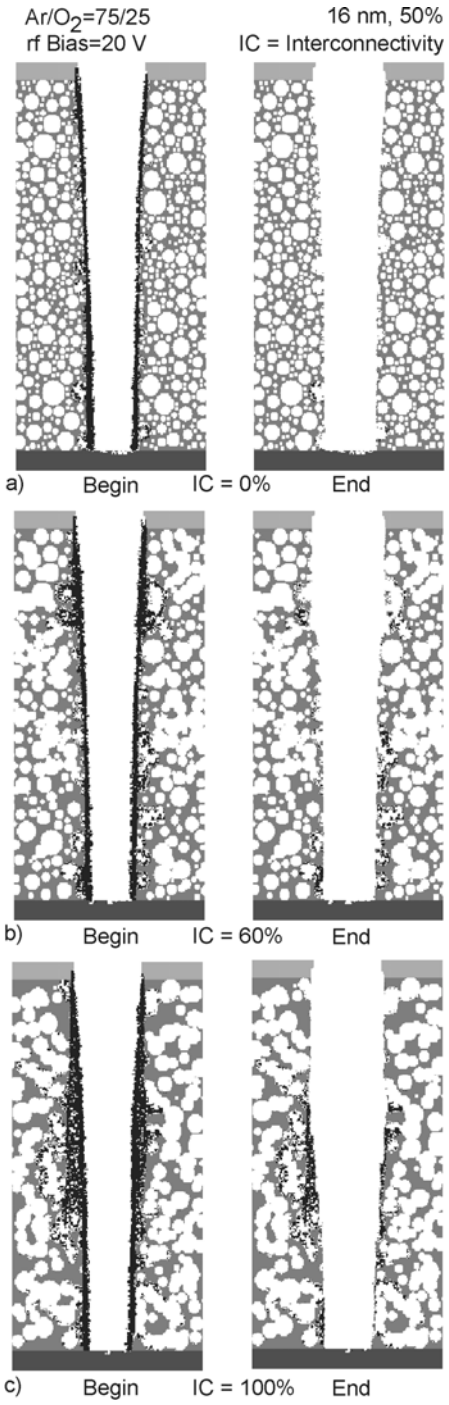

Fig. 5.8. Profiles of the vias before and after the stripping process for the base case conditions and 20 V bias using Ar/O_2 = 75/25 for PS with r_0 = 16 nm, porosity = 50%, (a) IC = 0%, (b) 60% and (c) 100%.

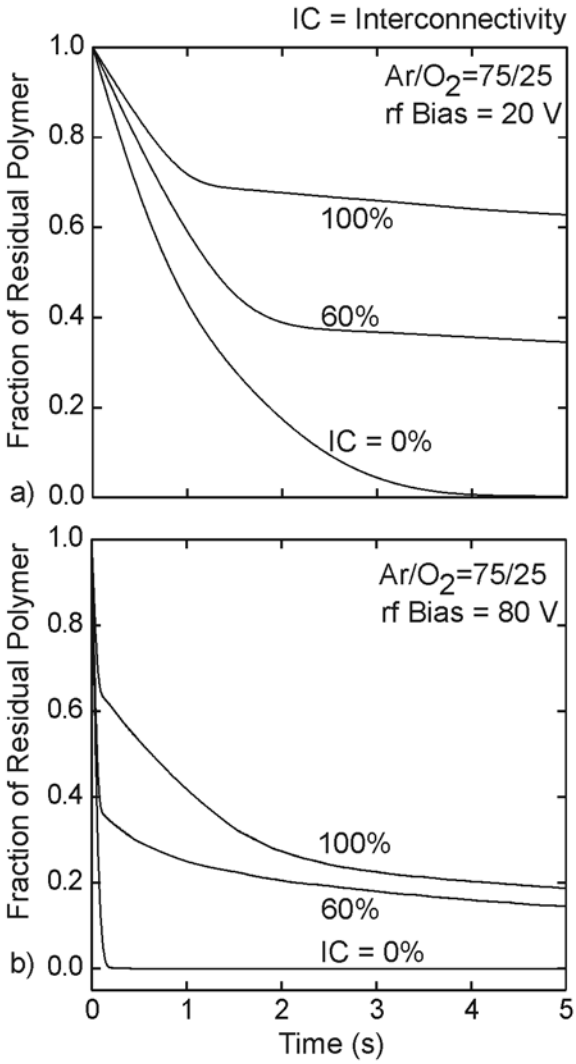

Fig. 5.9. Effect of interconnectivity and bias on the asymptotic limits of the residual polymer fraction cleaned using Ar/O_2 = 75/25 for base case conditions and (a) 20 V bias and (b) 80 V bias. Asymptotic limits decrease with increasing bias and decreasing interconnectivities.

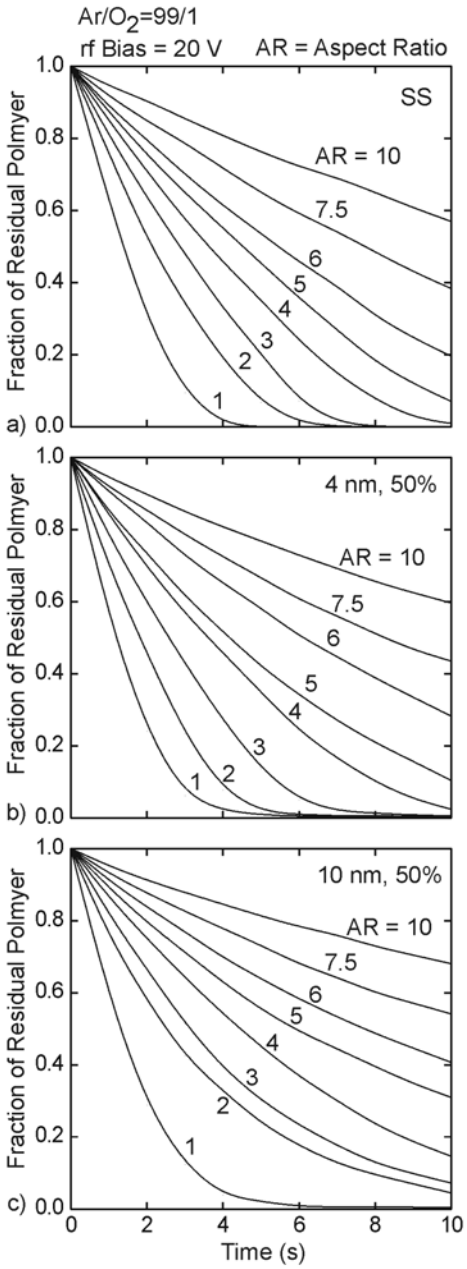

Fig. 5.10. Effect of aspect ratio on stripping efficiency for vias cleaned using Ar/O_2 = 99/1, base case conditions and 20 V bias for (a) SS, (b) PS with r_0 = 4 nm and porosity = 50% and (c) PS with r_0 = 10 nm and porosity = 50%. Cleaning efficiencies decrease with increasing aspect ratios due to lack of view angles for the ion fluxes at high aspect ratios.

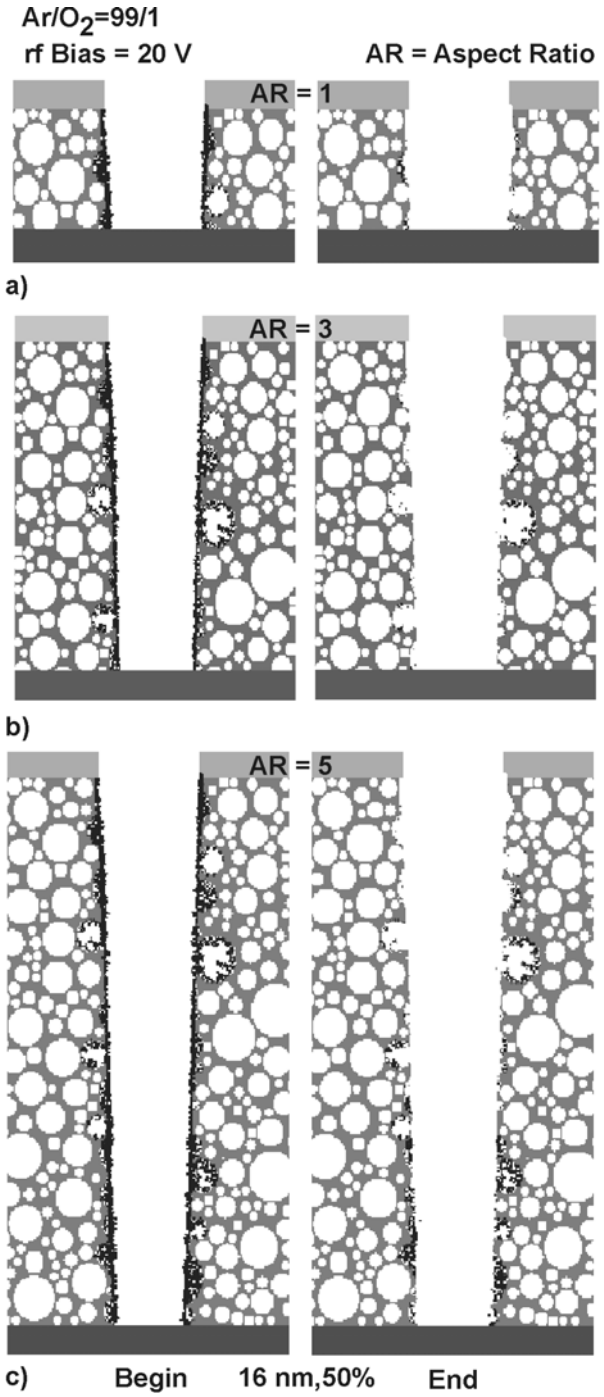

Fig. 5.11. Profiles of PS with r_0 = 16 nm and 50% porosity, stripped using Ar/O_2 = 99/1, 20 V bias and base case conditions for (a) AR = 1, (b) AR = 3 and (c) AR = 5. Top and the bottom of the trench have better ion view angles due to direct impact and reflection from the bottom of the trench respectively, which improves stripping for low and intermediate aspect ratios.

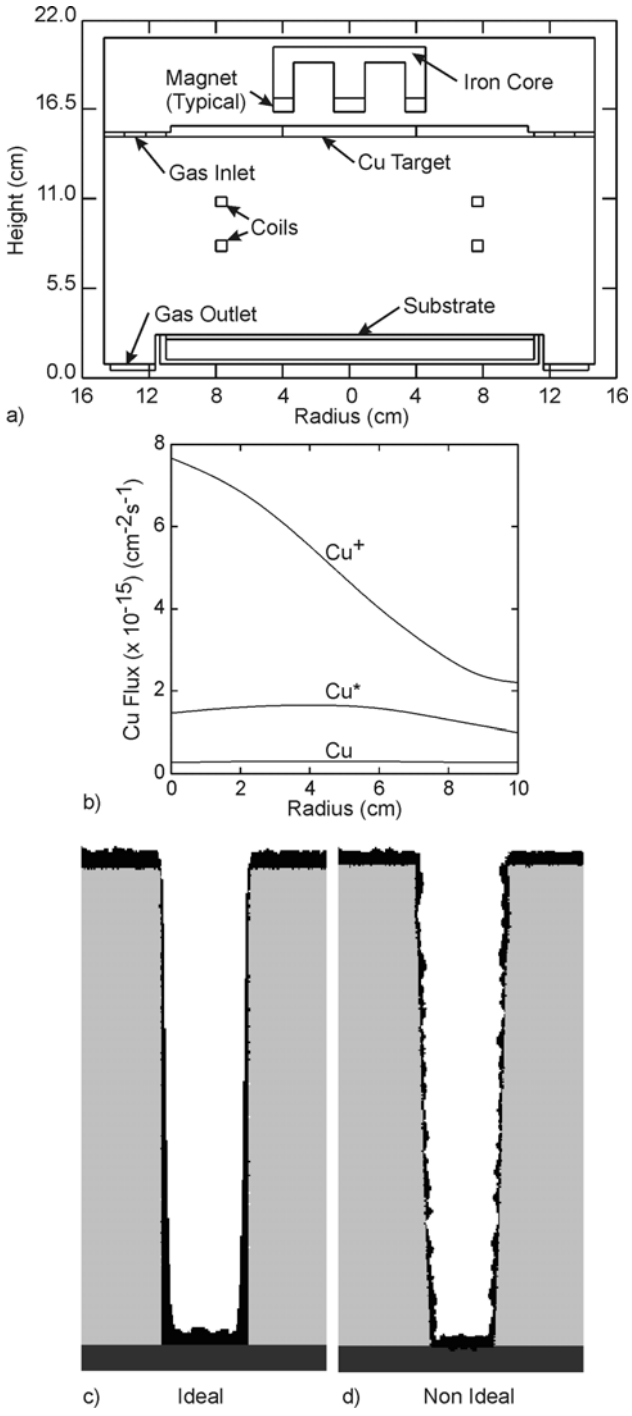

Fig. 5.12. (a) Schematic of the ICP reactor used for Cu IMPVD process. b) Fluxes of Cu^{+}, Cu* and Cu^{0} to the wafer for the base case. Profiles of SS trenches coated using Cu IMPVD for the base case for c) atomically smooth ideal trench and d) trench obtained after etching and stripping. Sputtering during the different processing steps results in sidewall roughness, which by micro shadowing produces unevenness in the deposited film.

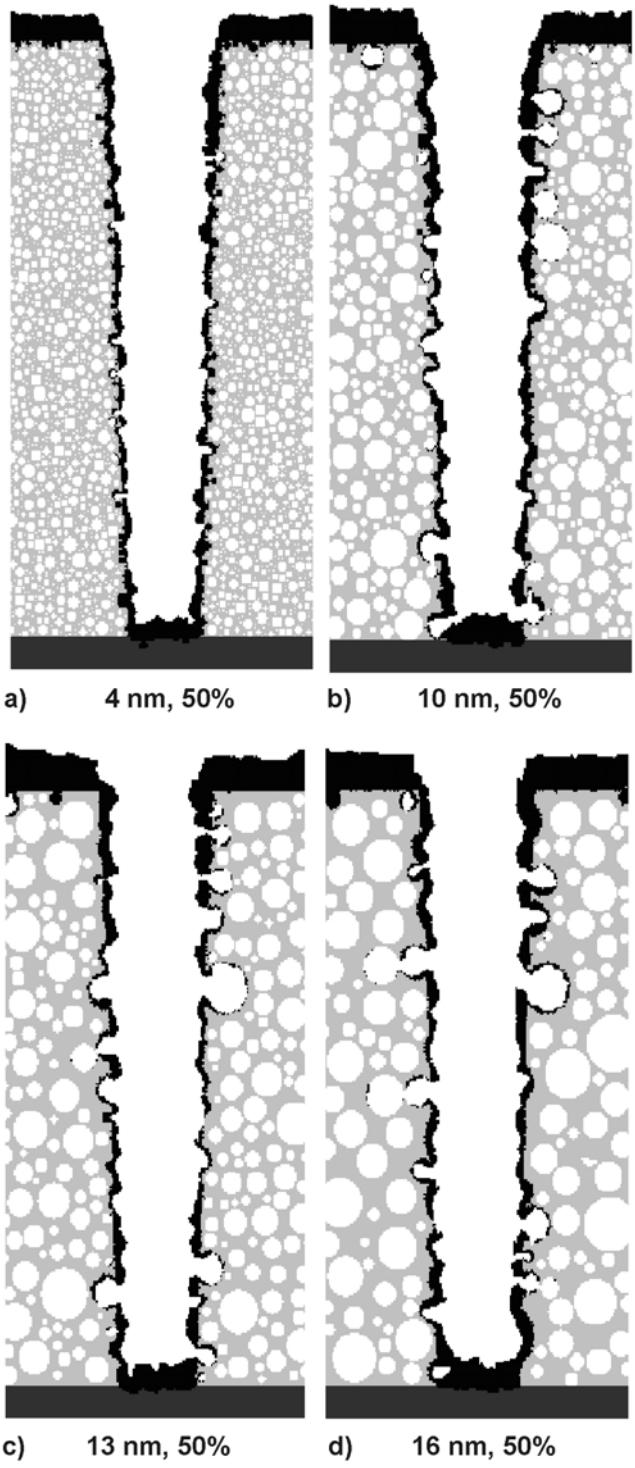

Fig. 5.13. Cu IMPVD onto 50% porosity PS trenches for different average pore radii. (a) 4 nm, (b) 10 nm, (c) 13 nm and (d) 16 nm. Coating is less conformal for larger pores and voids are created or initiated due to the presence of pores.

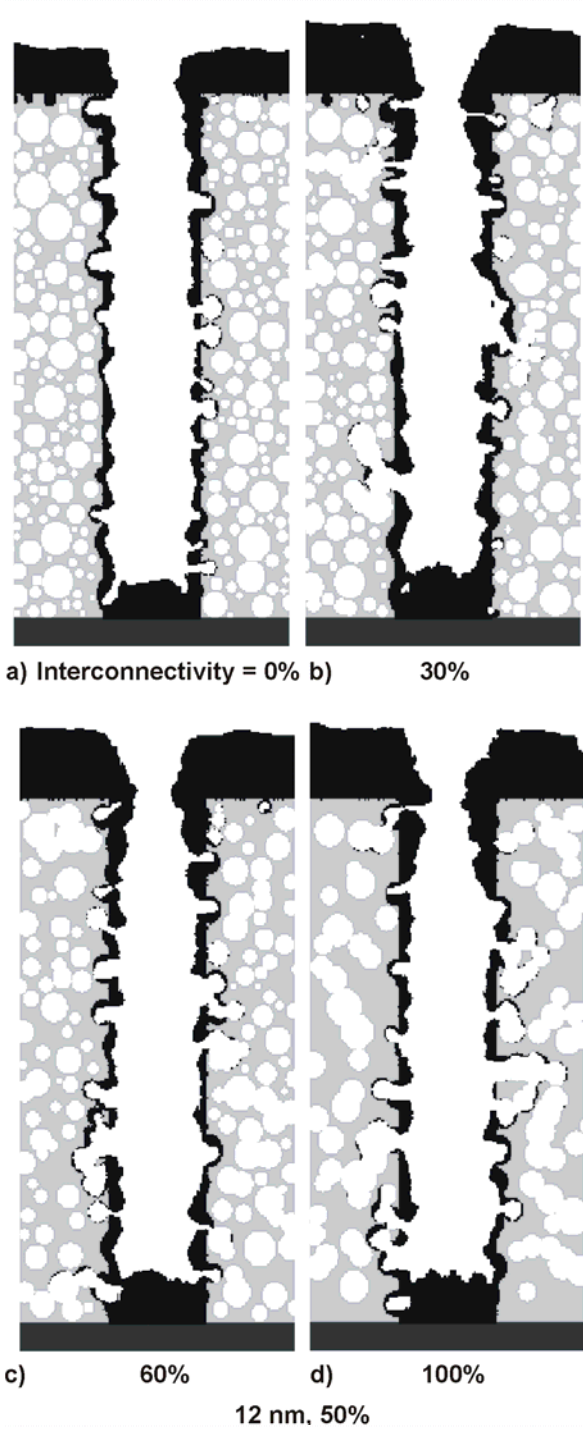

Fig. 5.14. Effect of interconnectivity on the Cu IMPVD process for cleaned vias of PS with r_0 = 12 nm and 50% porosity. (a) IC = 0%, (b) 30%, (c) 60% and (d) 100%. Thicker coatings are required for effective pore sealing and to avoid pin-hole formation. Thicker coating also leads to narrowing of the trench opening and pinch-off.

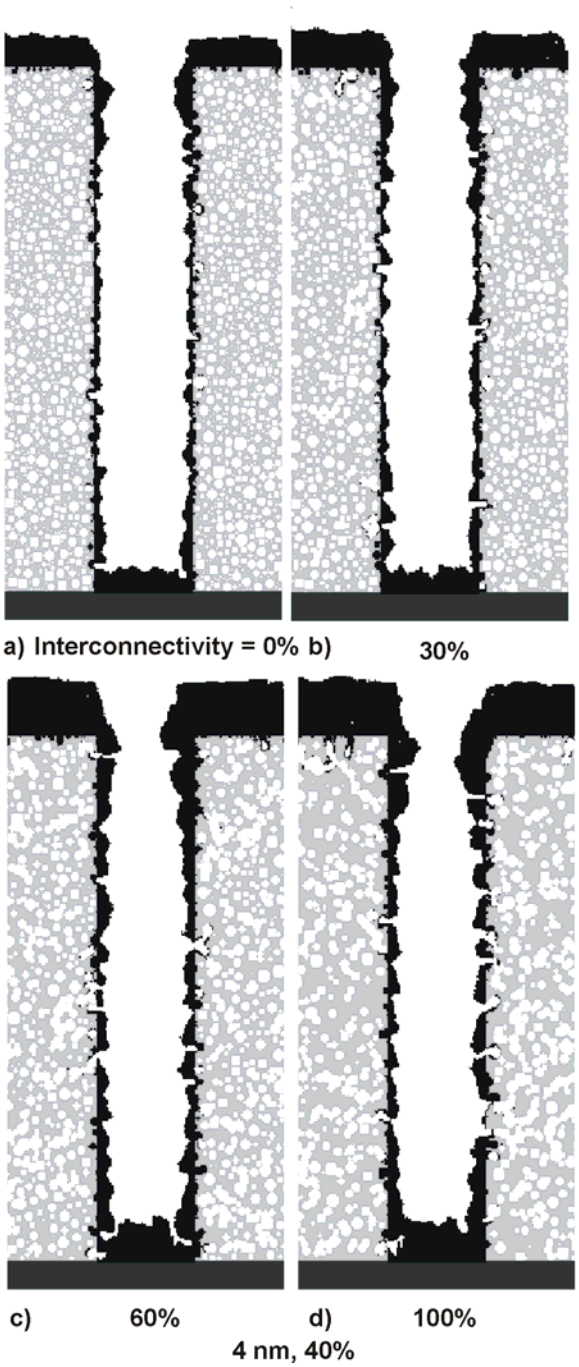

Fig. 5.15. Effect of interconnectivity on the Cu IMPVD process for cleaned vias of PS with r_0 = 4 nm and 40% porosity. (a) IC = 0%, (b) 30%, (c) 60% and (d) 100%. Deposition is more efficient for small pores, despite the problems posed by interconnected network and pore sealing is achieved.

5.7 References

[1] T. E. F. M. Standaert, P. J. Matsuo, X. Li, G. S. Oehrlein, T. M. Lu, R. Gutmann, C. T. Rosenmayer, J. W. Bartz, J. G. Langan, and W. R. Entley, J. Vac. Sci. Technol. A **19,** 435 (2001).

[2] J. Lu and M. J. Kushner, J. Vac. Sci. Technol. A **19,** 2652 (2001).

[3] M. Schaepkens, T. E. F. M. Standaert, N. R. Rueger, P. G. M. Sebel, G. S. Oeherlein, and J. M. Cook, J. Vac. Sci. Technol. A **17,** 26 (1999).

[4] F. Greer, L. Van, D. Fraser, J. W. Coburn, and D. B. Graves, J. Vac. Sci. Technol. B **20,** 1901 (2002).

[5] P. F. Cheng, S. M. Rossnagel, and D. N. Ruzic, J. Vac. Sci. Technol. B **13,** 203 (1995).

6. ETCHING OF POROUS AND NONPOROUS SiO_2 IN COMPLEX GAS MIXTURES

6.1 Introduction

Low pressure fluorocarbon plasmas are widely used in microelectronics fabrication for a variety of surface modification purposes, especially for etching of SiO_2 based dielectrics.[1-4] The choice of fluorocarbon plasmas typically used depends on the application and is based on optimizing the fluxes of neutrals and energetic ions. These parameters also determine the selectivity of etching one material compared to another. Subtle variations of these processes for different materials (etching of SiO_2 versus Si_3N_4) have resulted in the use of a wide variety of fluorocarbon gases (e.g., CHF_3, C_2F_6, and c-C_4F_8) and numerous additives (e.g., O_2, N_2, CO, and Ar) to optimize the reactant fluxes and delivery of activation energy.[4-6] c-C_4F_8 is commonly used for plasma etching of dielectrics such as Si, SiO_2 and Si_3N_4 among others and is often used in mixtures with Ar, CO, N_2, and O_2.[4,7]

To investigate issues regarding etching of SS and PS in such complex gas mixtures, the surface reaction mechanism developed for etching of organic polymers in O_2 plasmas has been modified to address etching of SS and PS in C_4F_8 chemistries with O_2 additives. For these investigations, the fluorocarbon etching mechanism discussed in Chapter 3 is essentially maintained the same. The fluorocarbon polymer formed during etching is treated as organic polymer and is etched by O_2 additives. Validation for etching of SS and PS is done by comparisons to experiments in ICPs for C_4F_8, C_4F_8/Ar and C_4F_8/O_2 chemistries and is presented in Section 6.2.[4] Profile simulations and validation for etching of SS and resist erosion obtained by comparisons to profiles from experiments in a magnetically enhanced reactive ion etching (MERIE) reactor for $C_4F_8/Ar/O_2$ chemistries are presented in Section 6.3. Profile simulations of

SS in $C_4F_8/Ar/O_2$ chemistries in an ICP reactor for varying pressures are presented in Section 6.4.

6.2 Blanket Etching of SS and PS in an ICP Reactor

The ICP reactor used for this study is similar to that which was used for etching of SS and PS in CHF_3 plasma presented in Chapter 4 and therefore is not described here. The base case process conditions are 20 mTorr pressure, 40 sccm flow of C_4F_8, 600 W ICP power at 13.56 MHz. The substrate was separately biased at 3.7 MHz to vary the self generated dc bias required for validation. The base case plasma properties are presented for a dc bias of –125 V. The gas phase chemistry for this work was developed by Vasenkov *et al*. on the same modeling platform (HPEM) as used earlier.[8] The gas phase plasma properties for these process conditions and their sensitivity to the parameters of the reaction mechanism have been explained in detail by Vasenkov *et al*.[8] The intent of this work is to use those results to study the surface processes and predict feature evolution. Hence, only relevant plasma properties have been discussed here.

Selective ion and neutral fluxes to the center of the wafer as a function of the radius for the base case are shown in Fig. 6.1. The prominent ions are CF_2^+, CF^+, CF_3^+ and $C_2F_4^+$. The prominent neutrals are C_2F_3, C_2F_4, CF_2, CF and F. Due to the low pressures and fairly large power depositions in these systems, there is a high degree of dissociation of the plasma, leading to smaller molecules being populated. The primary electron impact dissociation reaction of C_4F_8 yields C_2F_4. Dissociation of C_4F_8 and ionization of C_2F_4 are two important sources for the formation of $C_2F_4^+$. As a result, there is a large flux of both C_2F_4 and $C_2F_4^+$ in these systems. EADs of CF^+, CF_3^+ and $C_2F_4^+$ for the base case are shown in Fig. 6.2. The average energy for all the ions is ≈180 eV. The profiles indicate an anisotropic distribution for the ions. Heavier ions

have narrow EADs in energy, a consequence of their longer crossing time across the sheath and being less affected by collisions.

A comparison of computed results to experiments for blanket etching of SS as a function of the self-generated dc bias for the base case in c-C_4F_8 plasma is shown in Fig. 6.3. In accordance with earlier results presented in Chapter 4, there is a threshold bias for etching, which in this case is ≈40 eV. Polymer deposition dominates until the threshold bias. Increasing the bias further increases ion energies and reduces the passivation layer thickness, thus facilitating etching. At high biases, there is saturation in the etch rates due to the reduction of the polymer layers to submonolayer thickness. This is consistent with earlier observations.

Etch rates as a function of Ar and O_2 addition to c-C_4F_8 for blanket etching of SS for base case conditions and a dc bias of -100 V are shown in Fig. 6.4. Increasing the Ar in the gas mixture decreases the fluorocarbon mole fraction in the gas mixtures, thereby reducing the polymerizing fluxes to the wafer. Also larger ionization rates of Ar lead to larger ion fluxes at larger mole fractions of Ar. The cumulative effect is that the steady state polymer layer thickness decreases as the Ar fraction is increased. This has a positive effect initially, as it produces optimal polymer layer thickness on the SiO_2 substrate. The etch rate has a maximum for Ar mole fraction ≈0.6. At higher Ar fractions the steady state polymer thins down to submonolayers and there is an insufficient flux of etchants to the wafer, decreasing the etch rate.

A similar maximum in etch rate is observed with O_2 addition. The maximum in etch rate in this case is ≈0.4 mole fraction of O_2 and is consistent with experimental observations. O radicals etch away the organic polymer and thus reduce the polymer thickness, resulting in optimal polymer thickness for nominal O_2 additions. Increasing O_2 mole fraction reduces polymer thickness to submonolayers. Etch stop is observed for O_2 mole fractions of ≈ 0.9.

Etch rates of two PS films (4 nm and 30%; and 10 nm and 50%) as functions of Ar and O_2 additives for the base case conditions are shown in Figs. 6.5 and 6.6. For pure C_4F_8, etch stops for both the PS films unlike the SS film, which will etch. As observed in Chapter 4, the steady state polymer thickness on top of the SiO_2 substrate in C_4F_8 is ≈3-5 nm. Since the plasma is highly polymerizing, pore filling is dominant, thereby increasing the polymer thickness and producing an etch stop. A large Ar addition is required to increase ion activated processes to reduce the effect of pore filling. At Ar fractions ≈0.7, the etching of the 4 nm PS has a maximum rate. Increasing the Ar fractions to higher values decreases the polymer thickness to sub-optimal values despite the pore filling effect. For 10 nm PS, pore filling is more sever and so increasing Ar to 90%, monotonically increases etch rates. As a result, in this case there is no maximum. For both PS films, the corrected etch rate (ER_c) is less than the ER of SS, except at high Ar fractions when the polymer thickness on the SS film is submonolayer.

In contrast to Ar addition, less O_2 is required to counter the pore filling effect and the ERs of the PS films increase significantly with O_2 addition. Etching of the activated polymer sites formed by O radicals requires lower ion energies, so removal of polymer in O_2 plasmas is faster. Also, etching of polymer in O_2 chemistries is also neutral dependent to some degree and is less sensitive to polymer layer thickness. This results in larger etch rates and corrected etch rates in both PS films for less than 15% O_2 addition. The maximum in ER for 10 nm PS film is with ≈80% O_2 addition, which is larger than that for 4 nm PS film, (≈40%). This is a result of increased pore filling and thicker polymers with larger pores.

6.3 Profile Comparisons for Etching of SS and Resist Erosion in MERIE Reactor

The model reactor used in this study, shown schematically in Fig. 6.7, is patterned after

plasma sources that are commercially available. The metal substrate is powered at 10 MHz through a blocking capacitor. A conductive Si wafer (σ = 0.01/Ω-cm), 20 cm in diameter, sits in electrical contact with the powered substrate, which is surrounded by a Si ring (focus ring 1, $\varepsilon/\varepsilon_0$ = 12.5, $\sigma = 10^{-6}$/Ω-cm) and dielectric focus ring (focus ring 2, $\varepsilon/\varepsilon_0$ = 8.0, $\sigma = 10^{-6}$/Ω-cm). All other surfaces in the reactor are grounded metal, including the annular pump port and the showerhead, which extends to a radius of 10 cm. As an approximation to the magnetic fields, we specified that the magnetic field be purely radial and parallel to the electrodes. Although this magnetic field is unphysical at r=0, it is the configuration which best captures, within available computing resources, the behavior produced by asymmetric cross wafer magnetic fields. The base case operating conditions are 40 mTorr with a flow rate of $Ar/C_4F_8/O_2$ = 200/10/5 sccm, chosen as being similar to industrial processes, and 1500 W total power deposition. The rf bias amplitude is 512 V and the dc bias is –115 V. In this and other cases the rf amplitude was varied to obtain the desired power.

Fluxes of selected prominent ions and neutrals to the wafer as a function of the radius are presented in Fig. 6.8. Ar^+ is the most prominent ion, primarily because of its high mole fraction and because of the large ionization rates of Ar. In the case of fluorocarbon ions the heavier molecules have higher fluxes than the smaller ones, while the prominent neutrals have a fairly uniform flux distribution along the radius, except for CF_2, which decrease at the edge. Ion fluxes tend to increase at the edge of the wafer. We predict a moderate increase in the etch rate of both SS and resist at the edges based on higher ion activation; however, we have not quantified this effect in this work.

The EADs of the total ion flux and CF_2 radical flux (representative of the neutrals) for the base case are shown in Fig. 6.9. The neutrals have lower average energies and broader angular

distributions. The ions have a two peak energy distribution, which is typically found in rf biased systems.[9,10] The ions have an anisotropic distribution. The decrease in electron mobility due to the transverse magnetic field in this reactor results in a more resistive bulk plasma and a thickening of the sheath. This results in a lower collection of electron currents in the sheath during the period of the rf cycle when the potential of the sheath near the wafer is minimum. The smaller electric fields in the sheath as a result of the low electron currents lead to lower energy ions striking the wafer. This explains the broad energy distribution of the ions striking the wafer.

Profile comparisons to experiments performed at SEMATECH for the base case with $Ar/C_4F_8/O_2$ =200/10/5, 1500 W; $Ar/C_4F_8/O_2$ =300/10/5, 1500 W; and $Ar/C_4F_8/O_2$ =300/10/5, 2000 W are shown in Fig. 6.10.[11] The initial photoresist thickness is 450 nm and the initial trench width is 180 nm. The reaction mechanism for resist depletion by O_2 has been discussed in Chapter 3. For all the etch recipes, good agreement in terms of dielectric etching, resist erosion and feature width is obtained. As the Ar flow rate is increased, there is an increase in the total Ar^+ flux (total ion flux), which results in an increased resist etch. As resist trimming is more dependent on ion sputtering, it is more sensitive to increase in ion fluxes than dielectric etch. A similar result is obtained at higher power deposition of 2000 W. Based on these resist erosion comparisons, the resist etching mechanism was validated and the reaction parameters were determined (Table 3.2).

6.4 Profile Simulations of SS Trenches for Varying Pressures in ICPs

Profiles of SS trenches for Ar and O_2 addition for the base case in an ICP plasma are shown in Fig. 6.11. For polymerizing environments such as this, there is a thick passivation

layer on the sidewalls of the trenches. Since the ion EADs are anisotropic in nature, they deliver more activation energy onto the bottom of the trench than onto the sidewalls. This leads to a polymer build-up. Where one observes etch proceeding on blanket wafers for the same conditions, the sidewall polymer leads to an etch stop in the features. Ion sputtering of the sidewall passivation layer increases as a function of Ar additive and etching proceeds deeper before etch stop. At lower depths the ion view angles are smaller, leading to an eventual polymer build-up and cessation of etching. Even for > 80% Ar addition, etch stop occurs. Since etching of the passivation by O_2 requires less activation and is predominantly neutral dependent and since the neutral EADs are isotropic in nature, addition of O_2 is very efficient in reducing the sidewall passivation layers. For a nominal 15% O_2 additive, sidewall polymer thickness is sufficiently reduced to facilitate etching. Due to predominant neutral based etching, bowing is observed.

Profiles of SS trenches in Ar and O_2 addition for the base case obtained using the ICP reactor at a pressure of 10 mTorr are shown in Fig. 6.12. The sheaths are less collisional at lower pressures resulting in larger mean free paths for the ions in the sheaths and therefore higher ion energies in the sheaths. The fluxes of the predominant neutrals and ions are shown in Table 6.1. Due to lower pressures, densities of neutrals and ions are less in the bulk plasma. At such low pressures, diffusive transport dominates for the ions, resulting in a larger flux of ions reaching the wafer at the lower pressure of 10 mTorr and therefore in higher ion activation at lower pressures. While etch stop is observed in a pure c-C_4F_8 plasma at 20 mTorr, increased ion activation facilitates etching at 10 mTorr. The increased ion activation, however, with Ar addition leads to some undercutting in the feature. With O_2 addition, however, the etching process is predominantly governed by neutral etching and therefore increased ion activation as a

result of lower pressures has a relatively moderate effect on the etch rates and feature dimensions.

6.5 Concluding Remarks

Etching of PS and SS films in complex gas mixtures ($C_4F_8/Ar/O_2$) was studied by coupling reaction mechanisms developed for fluorocarbon etching of SiO_2 based dielectrics and oxygen etching of organic polymer. The coupled reaction mechanism was validated by comparisons to experiments for both blanket and profile etching in ICP and MERIE reactors. For both Ar and O_2 addition, blanket etching of SS and PS films showed maxima in etch rates, which corresponded to an optimal polymer layer thickness. In the case of PS films with larger pores, increased Ar and O_2 additives were required for optimal etch rates. Profile simulations in the MERIE reactor showed higher resist etching for larger Ar mole fractions and larger power deposition, which was a result of increased sputtering of the resists. Etch stop due to thick sidewall passivation was observed for etching of high aspect ratio features in ICPs. O_2 addition and lower pressures decreased the sidewall thickness and helped etching of such features.

6.6 Tables

Table 6.1: Fluxes of selected species to the center of the wafer for pressures of 10 and 20 mTorr. Process conditions: C_4F_8 plasma, 600 W ICP power, 40 sccm gas flow rate and –125 V self-bias.

	Flux ($cm^{-2}s^{-1}$)	
Species	10 mTorr	20 mTorr
CF_3^+	9.23×10^{14}	3.91×10^{14}
CF_2^+	4.41×10^{15}	1.35×10^{15}
CF^+	1.93×10^{15}	6.17×10^{14}
$C_2F_4^+$	7.35×10^{15}	3.75×10^{15}
CF_2	6.90×10^{17}	4.08×10^{17}
CF	5.93×10^{16}	5.59×10^{16}
F	1.32×10^{16}	6.73×10^{15}
C_2F_3	1.29×10^{16}	1.46×10^{16}
C_2F_4	5.17×10^{17}	3.55×10^{17}

6.7 Figures

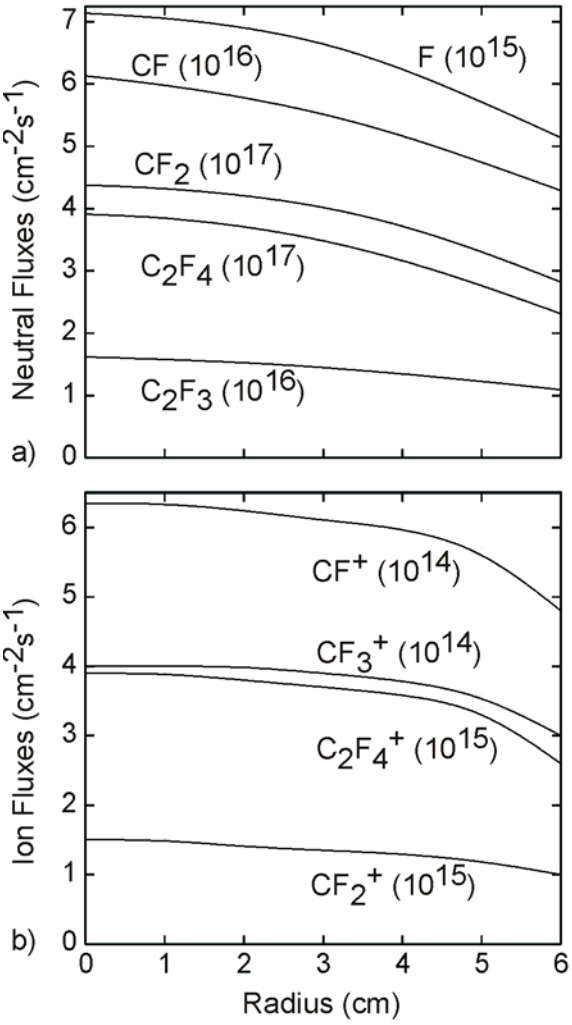

Fig. 6.1. Fluxes to the surface as a function of radius for C_4F_8 ICP plasma. (a) Fluxes of CF_2, CF, C_2F_3, C_2F_4 and F. (b) Fluxes of CF^+, CF_2^+, CF_3^+ and $C_2F_4^+$. The process conditions are 600 W ICP power at 13.56 MHz, 20 mTorr, 40 sccm and -125 V self-bias.

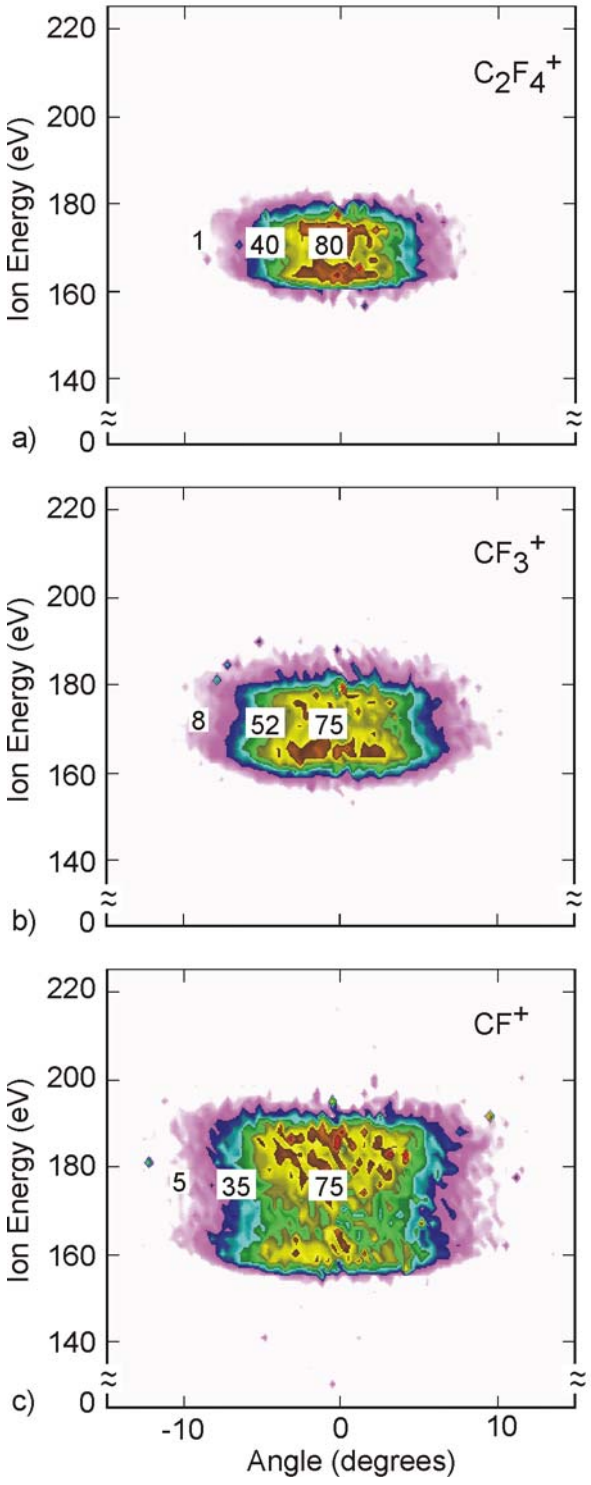

Fig. 6.2. Energy and angular distributions incident on and averaged over the wafer for the process conditions in Fig. 6.1 for (a) $C_2F_4^+$, (b) CF_3^+ and (c) CF^+.

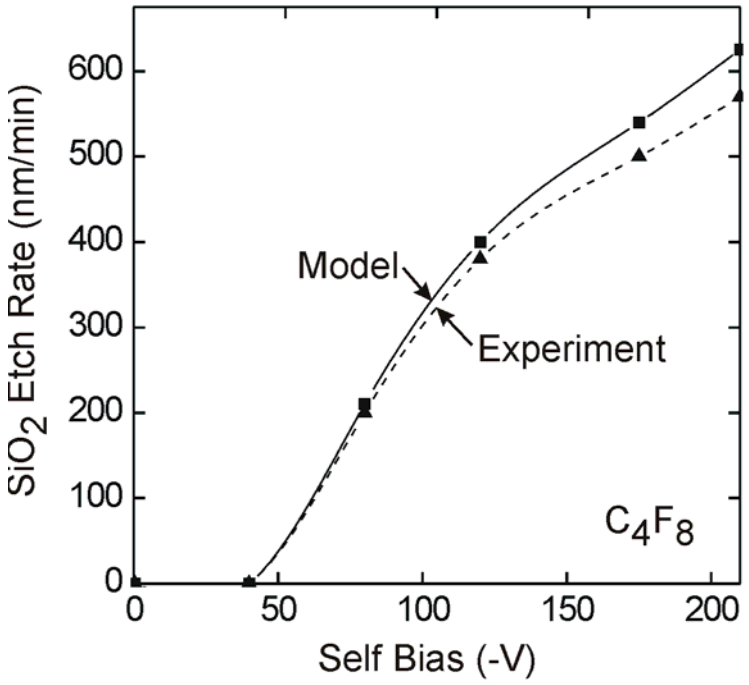

Fig. 6.3. A comparison of simulated and experimental results of SiO_2 etch rates as a function of self-bias voltage for a C_4F_8 plasma for process conditions in Fig. 6.1. Experimental results are from Ref. 4.

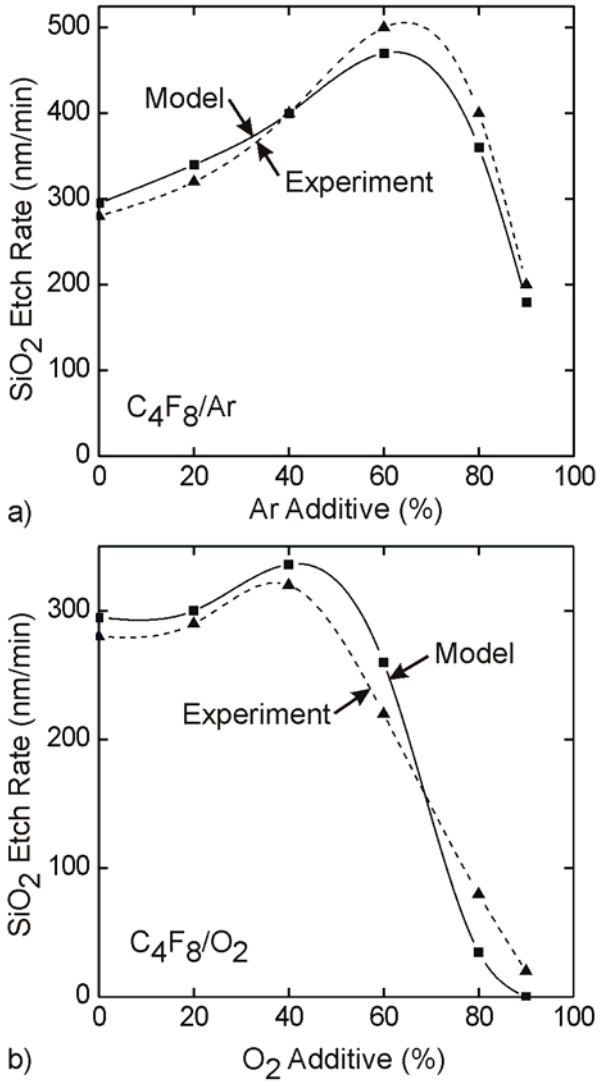

Fig. 6.4. A comparison of simulated and experimental results of SiO_2 etch rates as a function of (a) Ar and (b) O_2 mole percentages for process conditions in Fig. 6.1. Experimental results are from Ref. 4.

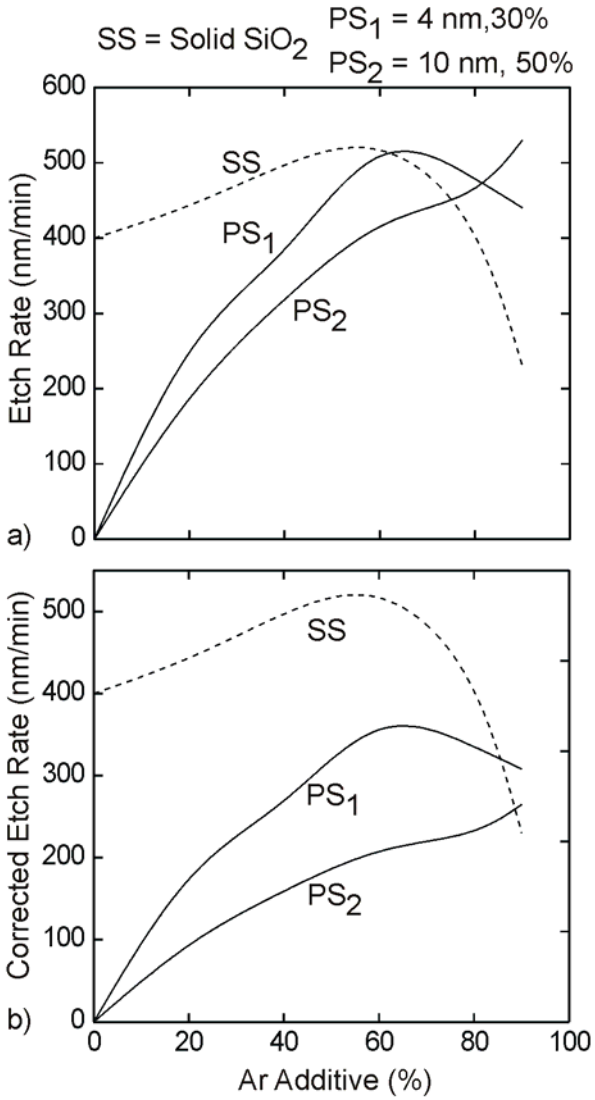

Fig. 6.5. Blanket etch rates of solid and porous SiO_2 as a function Ar mole percentages for process conditions in Fig. 6.1.

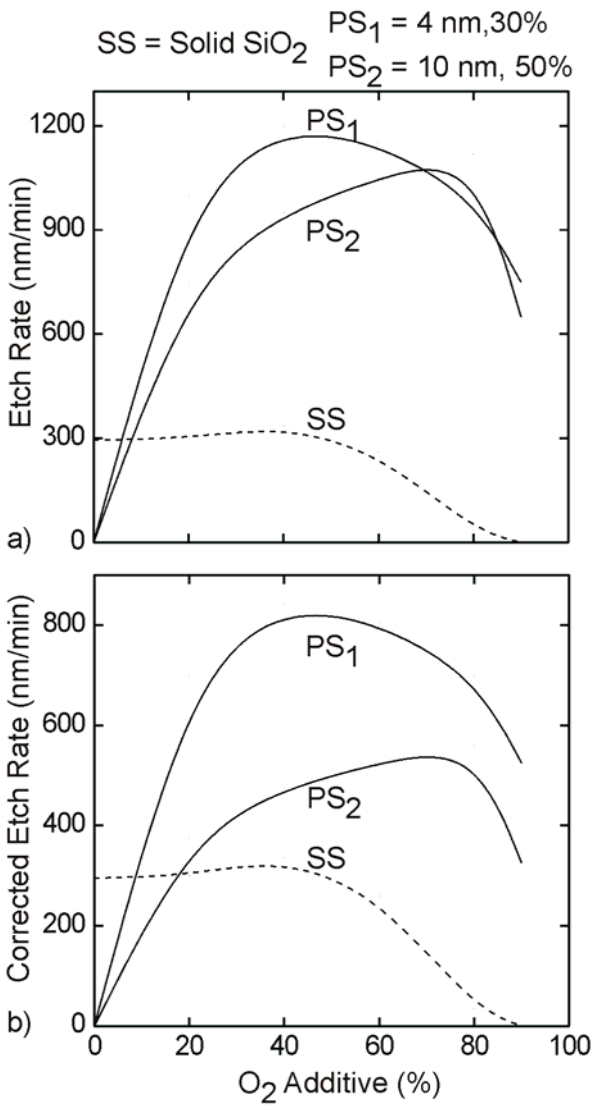

Fig. 6.6. Blanket etch rates of solid and porous SiO_2 as a function O_2 mole percentages for process conditions in Fig. 6.1.

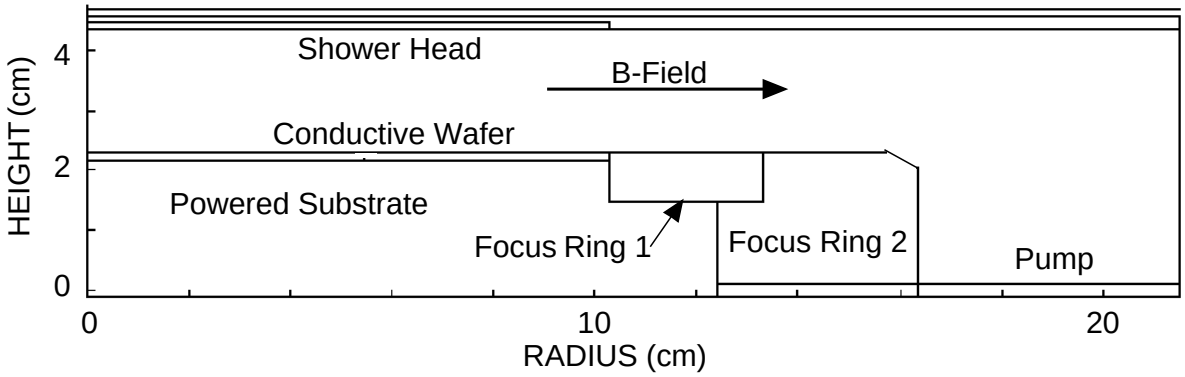

Fig. 6.7. A schematic of the MERIE reactor.

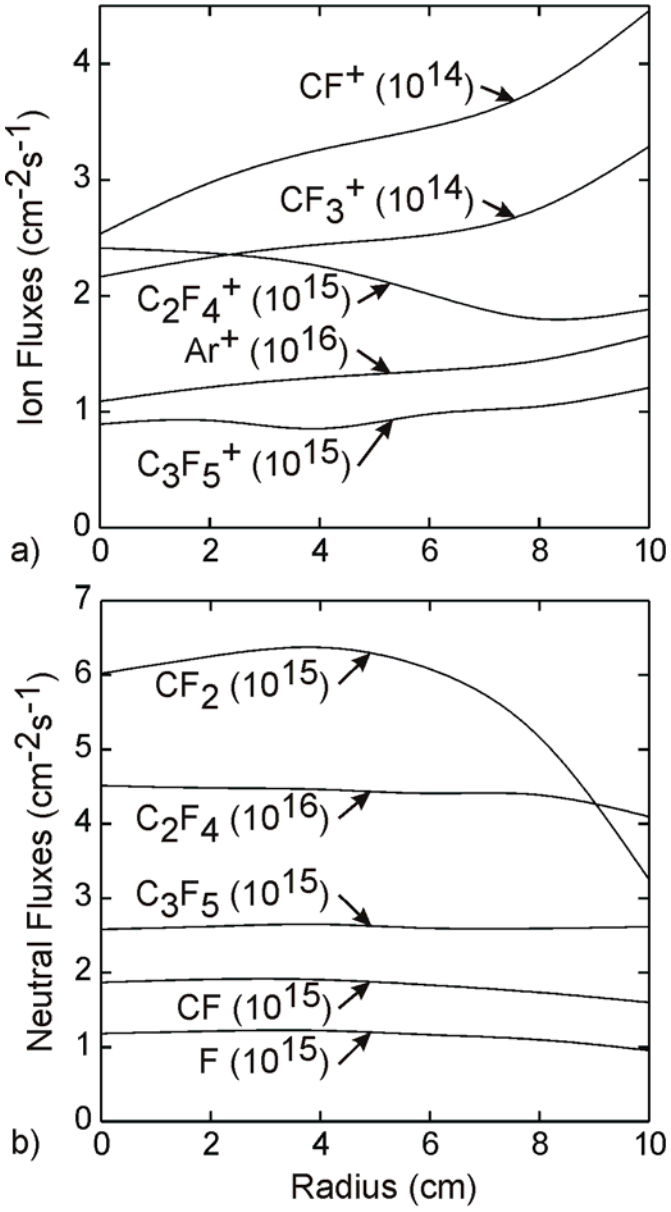

Fig. 6.8. Fluxes to the surface as a function of radius in a MERIE reactor. (a) Fluxes of CF_2, CF, C_3F_5, C_2F_4 and F. (b) Fluxes of CF^+, Ar^+, CF_3^+, $C_2F_4^+$and $C_3F_5^+$. The process conditions are 1500 W power, 40 mTorr, flow rate of $C_4F_8/Ar/O_2$ = 10/200/5 sccm and -115 V self-bias.

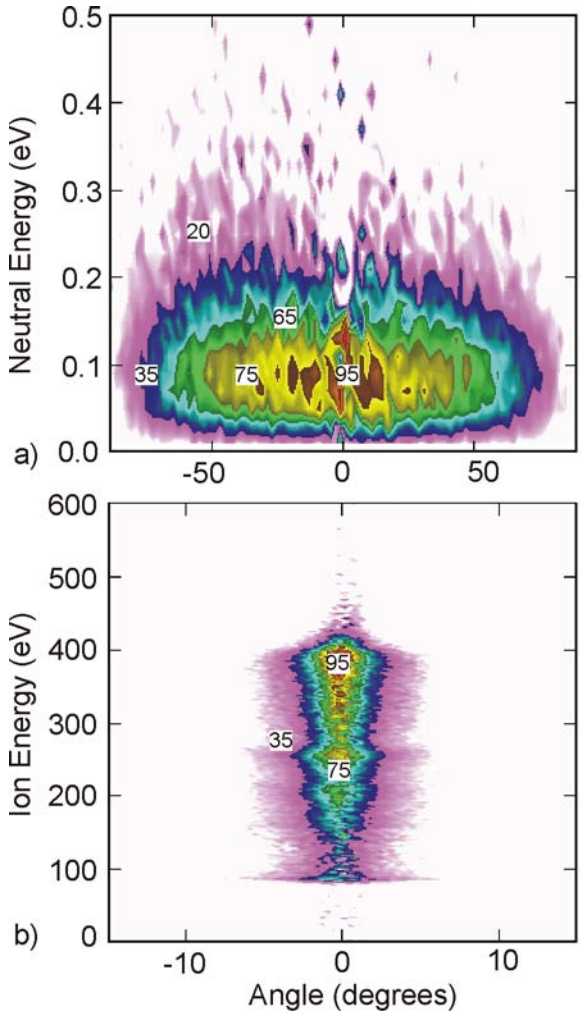

Fig. 6.9. Energy and angular distributions of ions and neutrals incident on and averaged over the wafer for the process conditions in Fig. 6.8.

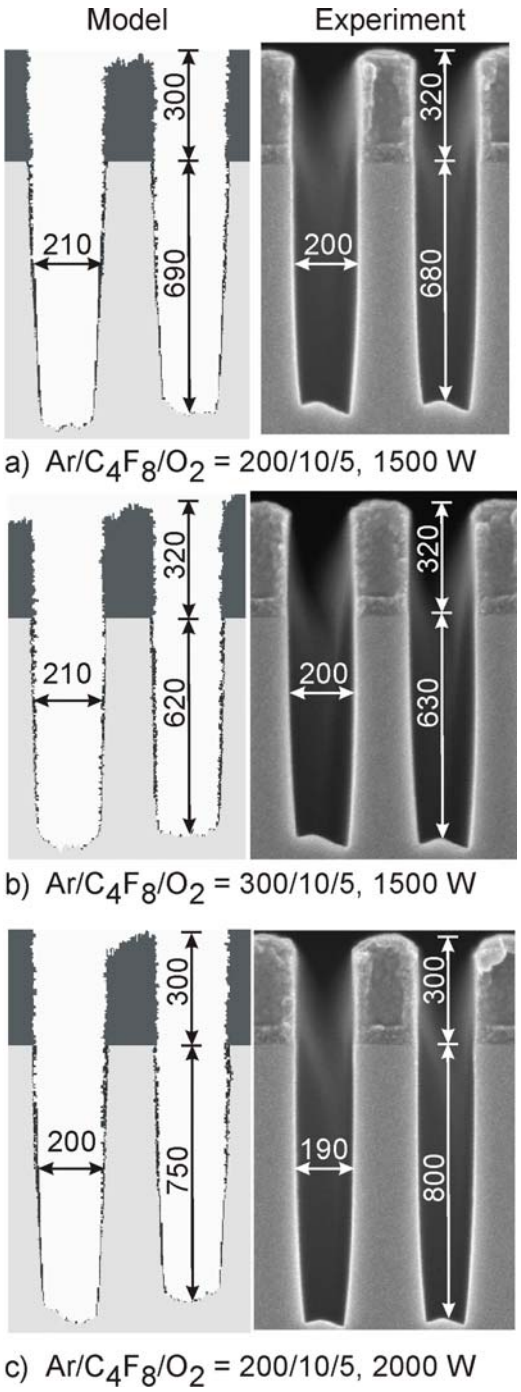

Fig. 6.10. A comparison of experimental and simulated results of SiO_2 profiles etched in a MERIE reactor for the process conditions in Fig. 6.8 for 9a) $Ar/C_4F_8/O_2$ = 200/10/5 sccm and (b) . $Ar/C_4F_8/O_2$ = 200/10/5 sccm. Experimental results are from Ref. 11.

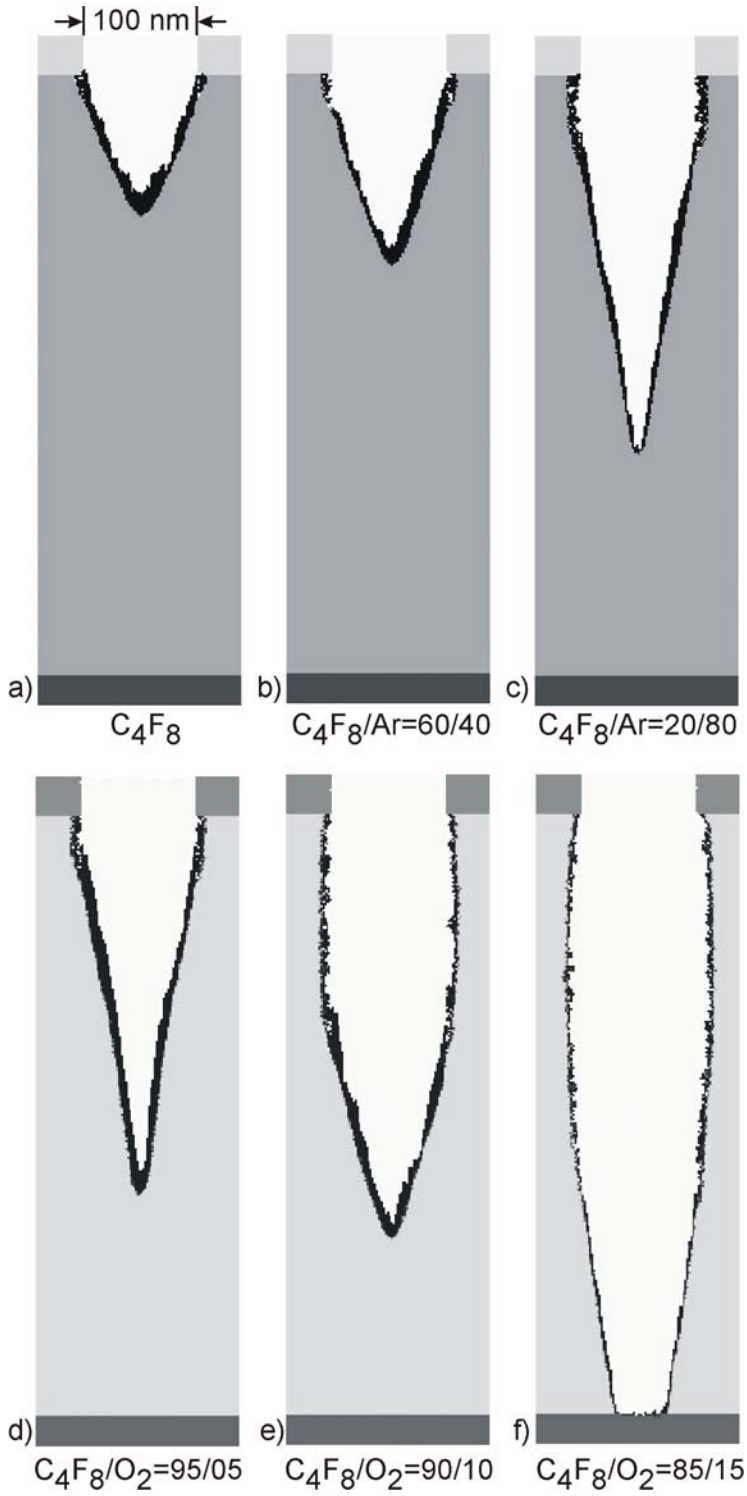

Fig. 6.11. Profiles of SiO_2 etched in a ICP plasma for process conditions in Fig. 6.1 for varying Ar and O_2 addition. (a) C_4F_8, (b) C_4F_8/Ar=60/40, (c) C_4F_8/Ar=20/80, (d) C_4F_8/O_2=95/05, e) C_4F_8/O_2=90/10 and f) C_4F_8/O_2=85/15.

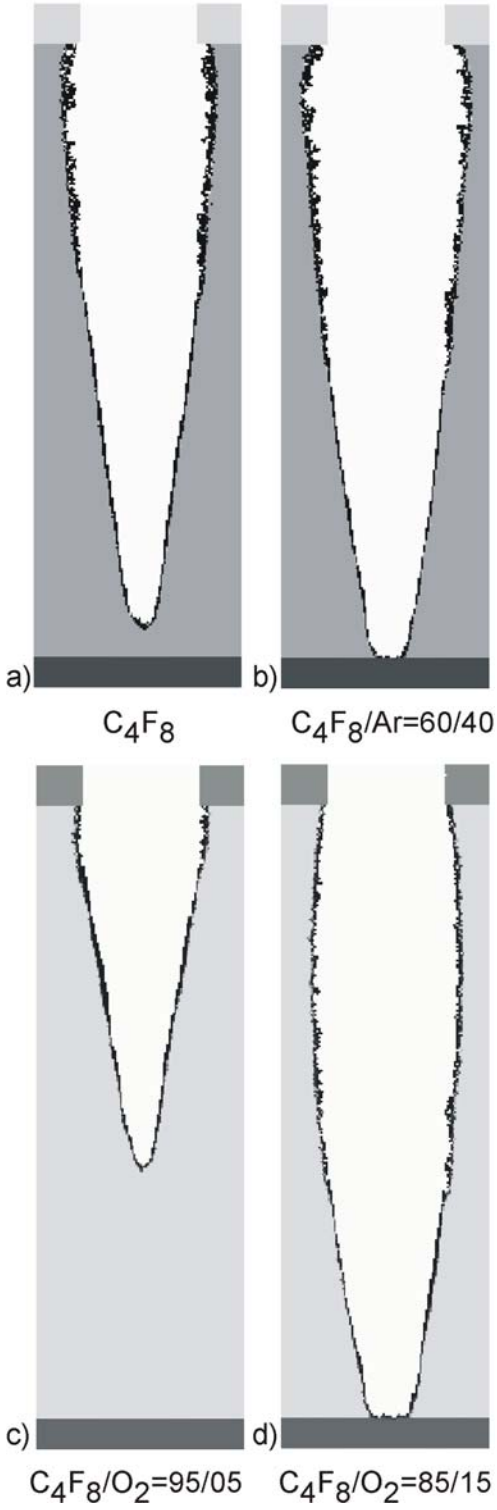

Fig. 6.12. Profiles of SiO_2 etched in a ICP plasma for process conditions in Fig. 6.1 and pressure of 10 mTorr for varying Ar and O_2 addition. (a) C_4F_8, (b) C_4F_8/Ar=60/40, (c) C_4F_8/O_2=95/05 and (d) C_4F_8/O_2=85/15.

6.8 References

[1] K. Miyata, M. Hori, and T. Goto, J. Vac. Sci. Technol. A **15,** 568 (1997).

[2] J.-P. Booth, Plas. Sources. Sci. Technol. **8,** 249 (1999).

[3] M. Sekine, Appl. Surf. Sci. **192,** 270 (2002).

[4] X. Li, L. Ling, X. Hua, M. Fukasawa, and G. S. Oehrlein, J. Vac. Sci. Technol. A **21,** 284 (2003).

[5] G. S. Oehrlein, M. F. Doemling, B. E. E. Kastenmeier, P. J. Matsuo, N. R. Rueger, M. Schaepkens, and T. E. F. M. Standaert, IBM J. Res. Develop. **43,** 181 (1999).

[6] M. Matsui, T. Tatsumi, and M. Sekine, J. Vac. Sci. Technol. A **19,** 1282 (2001).

[7] M. Matsui, T. Tatsumi, and M. Sekine, J. Vac. Sci. Technol. A **19,** 2089 (2001).

[8] A. Vasenkov and M. J. Kushner, submitted to J. Vac. Sci. Technol. A (2003).

[9] M. A. Sobolewski, Y. Wang, and A. N. Goyette, J. Appl. Phys. **91,** 6303 (2002).

[10] N. Mizutani and T. Hayashi, J. Vac. Sci. Technol. A **19,** 1298 (2001).

[11] V. Bakshi (private communications, 2003).

7. CONCLUSIONS AND FUTURE EXTENSIONS

7.1 Conclusions

Understanding plasma-wafer interactions is critical to microelectronics fabrication. Surface reaction mechanisms are among the least understood in plasma processing of semiconductors. As device sizes have decreased, increases in RC delay times in signal propagation have detrimentally impacted device performance. The adoption of low dielectric constant (low-k) materials as interlayer dielectrics (ILD) and copper as interconnect wires in microelectronics fabrication to alleviate this problem has brought forth newer complexities in the form of integration and process compatibility of the new materials. This has reemphasized the importance of understanding surface reaction mechanisms in plasma processing of semiconductors.

In this work the suitability of porous silica (PS) as an ILD was investigated. Compatibility of porous silica (PS) in plasma processing steps such as plasma etching, stripping of etch residues and plasma deposition of barrier coating onto the cleaned PS trenches have been analyzed. To investigate these issues, a surface reaction mechanism for fluorocarbon etching of SiO_2/Si was developed and validated among different fluorocarbon chemistries such as CHF_3, C_2F_6 and C_4F_8. The Monte Carlo Feature Profile Model (MCFPM) has been incorporated with the capability to address two-phase porous systems and has been used to simulated profile simulations. Profile simulations of PS films revealed that due to their complex morphologies, pore filling in PS films can affect etch rates. As such, etched trenches of PS have non-pristine surfaces, which can be problematic during subsequent post-etch processing. Interconnected pore networks and larger pores were found to be less suitable as they have a higher degree of pore

filling.

To investigate issues regarding post-etch process compatibility of PS films, a surface reaction mechanism for etching fluorocarbon polymer in O_2 plasmas was developed and extended to studying stripping of residual fluorocarbon from etched vias. The surface reaction mechanism was validated against blanket etching of polytetrafluoroethylene (PTFE). Stripping efficiencies indicated that closed PS films with smaller pores are a better choice for ILD applications. Cu IMPVD onto the cleaned trenches, investigated as a surrogate for deposition of barrier coating, indicated that the presence of pores was a source of non-conformality in the deposition process and lead to the creations of void in the barrier coating. Interconnected porous networks lead to formation of pin holes and narrowing of the trench opening. Both of these above issues are detrimental to the device performance.

7.2 Future Extensions

From a modeling stand point, improvements can be made to the surface reaction mechanisms. In the case of etching of polymers in both fluorocarbon and oxygen gas chemistries, the surface mesh cells could be represented by the different functional groups, depending on the polymer structure, instead of being represented by a single generic polymer species. This would render more flexibility and accuracy over a wider range of gas chemistries and would also pave the way for studying complex polymers with multiple functional groups, which could be useful in modeling many organic low-k dielectrics as an alternative to PS. As an extension, other silica based porous low-k materials could be investigated with slight modifications to the current surface reaction mechanism. Currently many of the silica based porous low-k materials investigated for ILDs have impurities such as methyl groups on the

surface of the pore. The two-phase model has the capability to incorporate non-vacuum pores into the mesh and can be utilized in analyzing such materials. 3-D modeling of PS films would better capture the physics in the spherical pores, which could be modeled using the 3-D MCFPM as opposed to depicting the pores as cylindrical.

Oxygen plasma based cleaning of PS films is known to have a detrimental effect on the dielectric properties of PS. As an alternative, stripping of residual polymer can be studied in H_2 plasmas. Such stripping would, however, entail process compatibility issues similar to those of stripping in O_2 plasmas. There is ongoing research on the effect of N_2 additives to O_2 plasmas for stripping. N_2 would have the positive effect of sealing the pore openings and preventing diffusion of O_2 into the interconnect structure thus maintaining the dielectric properties of the PS film. Surface reaction mechanisms for deposition of a TaN barrier coating could be modeled instead of using Cu IMPVD as a surrogate. Currently, processes to cross-link the carbon based functional groups in PS using novel gas chemistries are being investigated to effect sealing of the pores during deposition of a barrier coating. Depicting surface mesh cells as functional groups instead of molecular species would allow modeling such processes.

VITA

Arvind Sankaran was born in Chennai, India. He received his B. Tech. degree in Chemical Engineering in 1999 from the Indian Institute of Technology, Madras, India, and his M.S. in Chemical Engineering in 2001 from the University of Illinois at Urbana-Champaign. Under the direction of Professor Mark J. Kushner, he has studied surface reaction mechanisms in low temperature plasmas for semiconductor applications since December 1999. His work has resulted in two refereed journal publications and seven conference presentations. He has also worked as a teaching assistant and tutor for several engineering courses. He received the "SCS Excellence in Teaching Award" from the School of Chemical Sciences, University of Illinois for the year 2001-02. He will begin work in the spring of 2004 at Novellus Systems, Inc., in Portland, Oregon.